Electron spin resonance studies of impurity ions in rutile

S. W. Hodgskiss

ELECTRON SPIN RESONANCE STUDIES

of

IMPURITY IONS IN RUTILE

by

S. W. HODGSKISS, B.Sc.
(Hatfield)

A Thesis submitted to the University
of Durham in Candidature for
the degree of Doctor of Philosophy

August 1981

ABSTRACT

Electron spin resonance techniques were used to study the photo-electronic behaviour of defect centres in rutile, using both single crystal and powdered samples.

Single crystals of rutile were grown by a plasma torch method. Analysis of the boules by several techniques established that they contained, in general, fewer impurities than crystals grown by the conventional Verneuil method. Some boules were deliberately doped during growth with specific impurities. Control of the oxygen content of the plasma enabled the growth of some boules in a completely stoichiometric state, requiring no subsequent oxidation. Some crystals were doped after growth with various transition metal ions, using either evaporation and diffusion or vacuum capsule diffusion techniques.

E.S.R. analysis indicated the presence of several impurity ions, notably iron and nickel, in most samples. Low temperature ultra-violet irradiation caused significant changes to the intensities of most spectra, together with the appearance of several new spectra. Isochronal annealing then revealed the temperatures at which thermally stimulated charge transfers occurred, as reflected in changes to e.s.r. spectra. At least twelve different trapping centres were detected, with thermal ionization temperatures between 30 and 400K. Where possible, the ionization energies were determined by measuring variations in the rate of charge transfer with temperature and many of the values were in good agreement with those reported using other techniques. In most cases it was also possible to determine the polarity of the traps, by studying their interaction with other centres.

It is thought that many of the shallow electron traps consist of complexes of intrinsic defects, such as interstitial ions or vacancies,

with nearby Aluminium ions. Iron and chromium appear to form hole trapping centres with energy levels near the valence band. Nickel, Manganese and Copper are recombination centres with levels near the centre of the band gap.

The same e.s.r. methods were applied to samples of rutile pigments and a computer simulation technique was used to aid analysis and interpretation of powder spectra. All the pigment samples exhibited the same u.v.-activated e.s.r. spectrum. Isochronal annealing suggested that it represented a trapped hole and also inferred the existence of several shallow electron traps.

ACKNOWLEDGEMENTS

I would like to express my gratitude to the following for the valuable parts played by them in contributing to the work reported in this thesis:-

The Science Research Council, for the funding of the research project.

My supervisor, Dr. J. S. Thorp, for his guidance and support.

Professor G. G. Roberts, for the use of the facilities of the Applied Physics and Electronics Department.

Mr. F. Spence and his team of technicians, in particular Mr. R. Waite,for their assistance in building equipment and preparing samples.

Dr. W. Hutton, for many stimulating discussions and the use of his powder pattern simulation programme.

Dr. M. Hird of Tioxide International Ltd. for the use of crystal growth and mass spectrometer facilities.

Mr. E. Johnston, for tracing many of the diagrams.

Mr. S. Mellanby, for typing the thesis.

CONTENTS

Pages

Pages

CHAPTER 1

INTRODUCTION

The rutile form of titanium dioxide has sometimes been referred to as 'the ideal pigment', since when interspersed with a suitable organic binding medium it produces coating layers with maximum light scattering but minimal light absorption. The exceptional light scattering ability is due to the high refractive index of rutile, and has resulted in the growth, in the last 30 years, of a large industry concerned with the production of high grade titanium dioxide pigments (both rutile and anatase) for supply to paint and protective coating industries. In all applications where the brightness and opacity (or hiding power) are the chief requirements of the protective coating, rutile pigments have repeatedly given superior results to those of their rivals (Clark, 1975 , Cremer, 1977).

The main factor which determines the useful life of an exterior paint is the rate at which it degrades when exposed to sunlight, a process known as chalking in which the organic binder is gradually oxidized and decomposed, leaving unprotected pigment particles at the surface to give a chalk-like appearance. These pigment particles are then eroded to expose lower levels of the paint. There are two main mechanisms which cause the chalking process. The first involves the direct absorption of sunlight by the organic binder. In the second mechanism the pigment particles act as a catalyst to the organic degradation. The rutile particles absorb the ultra violet component of sunlight, which has sufficient energy to excite electrons transitions across the forbidden energy gap, causing an increase in the population of conduction electrons. The electrons at the surface of the pigment particles are then able to attack and degrade the surrounding organic binder, probably by the creation of highly reactive intermediate oxidant species, (**Pappas 1974**).

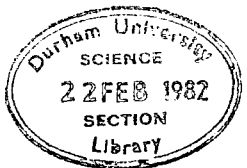

The addition of certain impurities, notably Aluminium and several transition metals, to rutile during pigment manufacture has been shown to slow down the chalking process and hence give a definite improvement in paint durability performance. Little is known of the actual mechanism by which doping of the pigment inhibits chalking, but it is assumed to be related to a decrease in the number of conduction electrons available at the pigment surface, possibly by the creation of electron traps and recombination centres in the rutile lattice. There is, therefore, considerable interest in characterizing the various defect centres introduced by different dopants in rutile and in studying their effects on photoelectronic properties, such as trap densities, recombination rates, etc.

A previous research project in this Department, conducted in association with rutile pigment manufacturers Tioxide International Ltd. of Stockton, involved the use of thermally stimulated conductivity (T.S.C.) and thermoluminescence (T.L.) techniques to investigate the photoelectronic properties of defects in rutile, using both single crystal and pigment samples. Such techniques can lead to the evaluation of charge trapping parameters such as trap density, capture cross-section and ionization energy, but are usually unable to provide any information with regard to the origin or identity of each trapping centre. Other research workers in this Department have used electron spin resonance (E.S.R.) spectroscopy to study dopant ions in single crystals (e.g. Gd in $CaWO_4$, Cr in MgO) and glass ceramics. E.S.R. can reveal both the identity of a paramagnetic defect and its site in a diamagnetic host lattice. It was the realisation that T.S.C. and E.S.R. could provide different but complementary information about the same centres which lead to the proposal for the research project which is reported in this thesis.

The basic aim of this work has been to combine aspects of both techniques and thereby develop a method of studying the photoelectronic behaviour of impurity centres in rutile more directly, by measuring the effect of optical irradiation and temperature variation on their e.s.r. spectra. More specific objects were to detect thermally and optically stimulated changes in e.s.r. spectral intensities to compare with existing T.S.C. and T.L. data, to identify known trapping centres and to investigate the possibility of determining trapping parameters from e.s.r. measurements.

The majority of the work was carried out using single crystals of rutile, which usually yield much more useful analytical information than powdered samples. Several of the single crystal samples were taken from commercially supplied boules, which had been grown by the conventional Verneuil method. Other samples, however, were 'home-grown', and a considerable amount of time was spent developing a method of growing rutile crystals of controlled stoichiometry by an O_2-Ar plasma torch technique, using equipment at Tioxide International. A description of the apparatus and growth procedure and a summary of the crystals produced are reported in Chapter 2.

Chapter 3 consists of an introduction to the basic concepts of e.s.r. spectroscopy, with a discussion of applications and interpretations of results.

Chapter 4 presents a review of rutile properties, with emphasis on the structure, e.s.r. and optical data, and the effects of impurities.

Chapter 5 discussed experimental details, including a brief explanation of the operation of the e.s.r. spectrometer, an account of the methods used to dope and prepare samples, and a description of the measurement techniques. Single crystal results are presented in Chapter 6.

In addition to the single crystal studies, some time was devoted to a preliminary investigation of rutile pigment samples supplied by Tioxide International. The results from these samples and the analysis of e.s.r. powder spectra by computer simulation are summarised in Chapter 7.

Finally, Chapter 8 discusses the results and presents conclusions from the project, together with suggestions for further work.

CHAPTER 2

CRYSTAL GROWTH

2.1 INTRODUCTION

Single crystals of synthetic rutile were first grown by the National Lead Company in 1947 (Moore, 1947), using the well-established Verneuil technique (Verneuil, 1902), and this still remains the most commonly used method for growing boules commercially. Basically, the method consists of feeding a powdered charge material into an oxygen-hydrogen flame, which melts the powder. This then falls into a molten interface on a seed crystal which is lowered into an afterheater as it grows. In general the Verneuil method does not produce crystals of as high quality as other methods of growth from the melt, such as zone melting or Czochralski crystal pulling. Its main disadvantages are the difficulty of controlling growth parameters, limited choice of gas ambient, high thermal gradients and the relatively small liquid volume, which can lead to strains and inhomogeneities in the crystal. The technique, however, does have an important advantage in that it requires no crucible and hence can still be used for the growth of high melting-point crystals, for which no suitable crucible material can be found. The melting point of rutile is 1870^{o}C (Brauer, 1960), and although single crystals of rutile have successfully been grown by the Czochralski method (Nassau, 1962), analysis showed them to be significantly doped with iridium, the crucible material. Several other techniques have been applied to the growth of rutile single crystals, including zone refining by r.f. induction heating (Holt, 1965), growth from a $Na_2O.3B_2O_3$ flux (Berks, 1965) and chemical vapour deposition using titanium tetrachloride and oxygen (Farrell, 1975).

One of the main problems in using the Verneuil method to grow rutile is that the hydrogen content of the flame chemically reduces the crystals so that, in order to approach full stoichiometry, a subsequent oxidising heat

treatment is needed. Another consequence is that large amounts of interstitial hydrogen are incorporated into the crystal lattices. These problems can be overcome by replacing the oxygen-hydrogen flame with a r.f.induction plasma torch (Reed, 1961) which allows the use of oxidising or inert gas ambients and the attainment of higher temperatures. In their simplest form induction plasma torches consist of concentric quartz tubes, open at one end and with gas injected at the other, surrounded by a r.f. coil. The feed material is dropped through the plasma, melted and collected on the growing crystal as in the conventional Verneuil technique. This approach was first used to grow rutile crystals by Chase and van Ruyven (Chase, 1969), who used a 5% O_2-95% Ar plasma. Their boules were non-stoichiometric, probably due to insufficient oxygen content of the plasma, but significantly the subsequently re-oxidized crystals did not exhibit the time-dependent conductivity found in Verneuil-grown crystals (van Raulte, 1965). Chase and van Ruyven ascribed this difference to the absence of interstitial hydrogen in their crystals, though their interpretation was disputed by Johnson (1968), who suggested that the time-independent conductivity of the plasma-grown crystals was due to there being a relatively low concentration of interstitial titanium ions, following heavy re-oxidation at 1300^{o}C.

The technique which was adopted to grow rutile single crystals is a refinement of the induction plasma torch method used by Chase and van Ruyven. The aim was to grow crystals of high quality, in terms of both intrinsic and extrinsic defects, and to investigate the possibility of growing stoichiometric rutile. It was also our intention to grow some boules deliberately doped with trivalent aluminium or pentavalent niobium. The work described in this chapter was performed in conjunction with Mr.R.Hillhouse, a fellow research student of the Department of Applied Physics and Electronics, and was carried out at the Central Laboratories of Tioxide International Ltd., Stockton on Tees.

2.2 EXPERIMENTAL

2.2.1 Apparatus

A diagram of the crystal growth apparatus is shown in Fig. 2.1. The plasma gun consists of two concentric quartz tubes, open at one end and mounted at the other end into a brass holder with channels drilled into it, through which the gases are injected to give a laminar flow down the tubes. The plasma gas mixture of oxygen and argon flows down the inner quartz tube, of 31 mm bore and 15 cm length. Energy is supplied to the plasma gases via a 5-turn, water-cooled copper induction coil, powered by a Lepel r.f. generator operating at 2.6 MHz and 9 kW. The coil surrounds the outer quartz tube and is situated about 3 cm below the end of the inner tube. In addition, a flow of argon is injected between the two quartz tubes and has the dual purpose of centring the plasma and cooling the outer tube. Jets of compressed air also help to cool both the outer tube and the induction coil. Fig.2.2 is a photograph of the plasma gun assembly during crystal growth.

The feed material, prepared from triply-distilled titanium tetrachloride and provided by Central Laboratories, Tioxide International, is sandy rutile, and is so called because of its very uniform particle size of 40 $\pm$ 2 μm and its consequent tendency to flow like sand. The feed is stored above the plasma in a cylindrical perspex hopper, the bottom face of which consists of a 75 μm steel gauze. To produce a constant flow of feed powder from the hopper a vertical 100 Hz sinusoidal vibration is applied to the gauze via a steel rod passing along the axis of the hopper, attached at one end to the gauze and at the other to a vibrator. Control of the feed rate is achieved by varying the amplitude of the sinusoidal displacement. The feed is carried towards the plasma region in a small flow of oxygen and is directed, via a quartz funnel, to a brass probe, with a tip consisting of a double-walled, water-cooled copper tube. Because the plasma has a hollow core, the probe can be raised and lowered through the centre of the plasma gun,

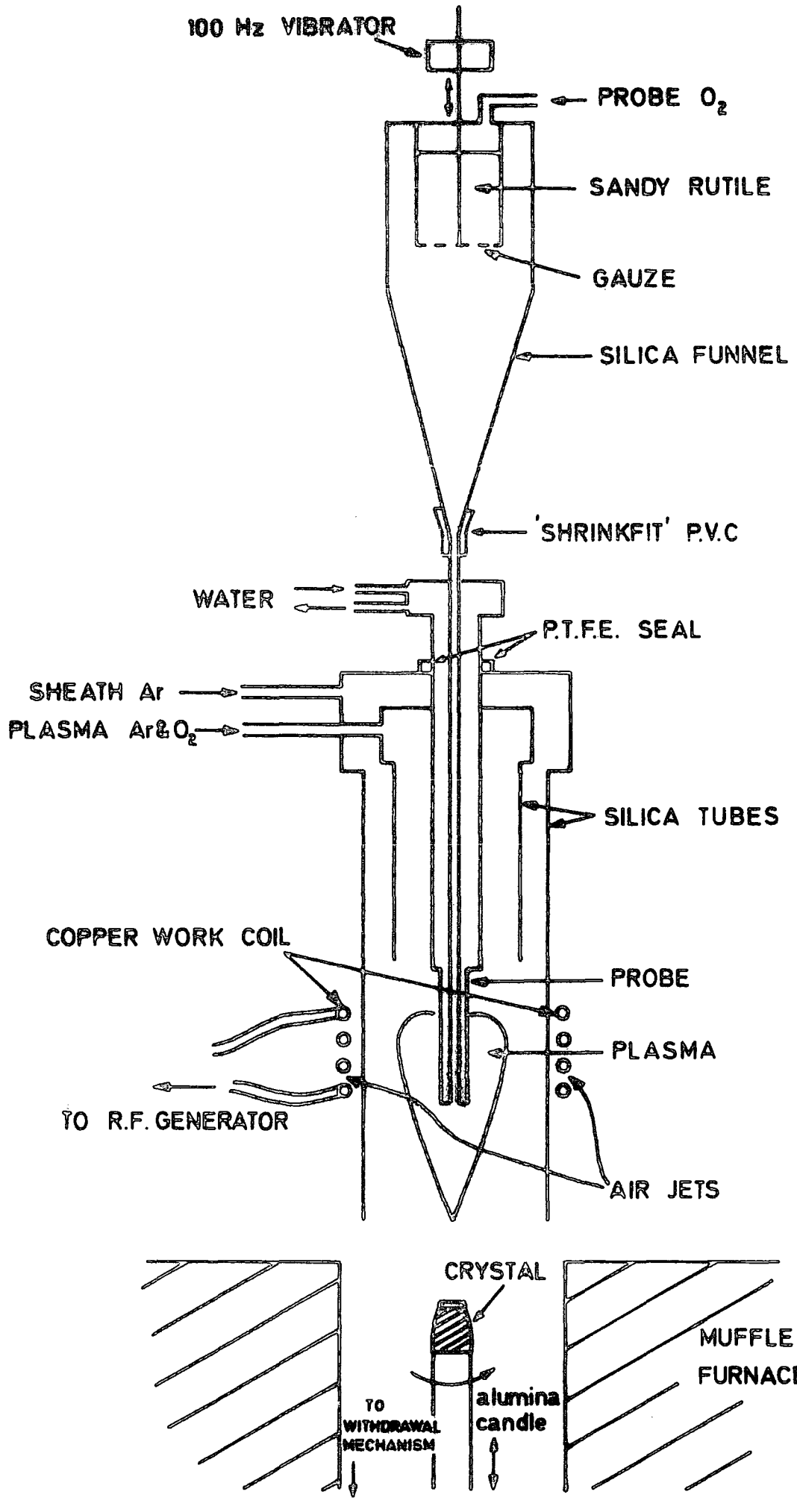

FIG. 2·1 PLASMA TORCH CRYSTAL GROWTH APPARATUS

Figure 2.2 : Plasma gun assembly during crystal growth.

giving control over the point at which the feed is released into the plasma.

The molten rutile is collected and crystallized on an alumina candle, of 1 metre length and 1 cm diameter, which revolves at 6 r.p.m. about an axis colinear with both the plasma and the feed probe. Under stable growth conditions, the candle is automatically withdrawn, at a rate of 3 cm per hour, into a muffle furnace which is coated with alumina cement to keep the vertical temperature gradient as low as possible. There is also a faster manual control of the candle height to facilitate the location of the optimum growth position.

2.2.2 Growth Procedure

Prior to initiating the plasma, the feed probe was raised and the alumina candle lowered away from the plasma region. The plasma was 'ignited' with a tesla coil using only Argon, at a flow rate of 21 l. per min, with a sheath Argon flow rate of 27 litres per min. Following ignition the r.f. power was raised and the plasma Argon flow rate was simultaneously increased to 37 l. per min. Safety covers containing u.v.-absorbing windows were then erected around the plasma. It was found that, unless the quartz tubes were concentric, the plasma would become unstable and susceptible to quenching. When a stable plasma had been realised the feed probe was lowered so that its tip was positioned about 2 cm. below the induction coil. The relative displacement of the feed probe and the plasma proved to have a critical effect on the growth conditions. At this stage, the oxygen content of the plasma was gradually increased to 5 l. per min.with a consequent increase in the plasma temperature and a flow of 1 l. per min. of oxygen was supplied to the feed probe.

A 100 Hz vibration was applied to the gauze at the base of the feed hopper, producing a steady flow of sandy rutile into the plasma, where it was melted. The alumina candle was raised until its tip was approximately level with the top of the muffle furnace, at which point the feed rate was increased to produce a rapid sintered growth on the candle. The feed rate was returned to its initial level and the candle height manually adjusted to remelt the top

of the polycrystalline deposit and hence locate the growth zone. Growth of a single crystal then proceeded by withdrawing the candle in order to maintain a molten cap on the boule at a constant height with respect to the plasma. It was found that several parameters critically affected both the optimum location of the molten cap and the growth rate, necessitating frequent use of the manual control for minor adjustments of the candle height. It was essential to maintain constant gas flow rates, since small changes in them had a marked effect on the temperature and shape of the plasma torch. Similarly, the flow rates of the feed powder varied between different batches of sandy rutile, and also the feed rate changed as the hopper emptied, requiring corrections in the candle height to relocate the growth zone. If the feed rate was too high, some of the powder would remain unmelted by the plasma and a polycrystalline crust would form on the crystal surface. If, however, the feed rate dropped, a heat sink was removed from the plasma and the crystal would be remelted. Furthermore, the position of the feed probe tip relative to the plasma affected both the percentage of feed falling on the boule and the oxygen content of the gases incident on the boule. When the feed was released near the centre of the plasma, i.e. with the probe tip just below the induction coil, the probe oxygen flow had little effect on the overall gas composition and the feed tended to diverge away from the central axis, forming a polycrystalline coating on the outer quartz tube. But if the probe was lowered further into the tail of the plasma, the flow of feed was much more directional, so that most of it fell on the boule, and the oxygen flow which accompanied it considerably increased the oxygen content in that region of the plasma. Using the latter configuration some rutile crystals were grown in a stoichiometric state and did not require subsequent oxidation of the 'as-grown' boules.

On the completion of a growth run, which would typically last about two hours, the chief consideration was to cool the boule as slowly as possible, to avoid introducing excessive strain in the crystal. This was done by gradually reducing the oxygen content of the plasma while withdrawing the

boule into the centre of the muffle furnace, over a period of about ten minutes, but keeping the feed on and hence building a polycrystalline crust on the boule. Then the feed and probe oxygen supplies were turned off and a further five minutes allowed before the r.f. power and the remaining argon gas flows were switched off simultaneously, to avoid blowing cold gas on the boule. The furnace was left to cool overnight before removing the boule from the candle.

Some boules were deliberately doped with impurities by mixing appropriate amounts of either the dopant metal powder, as with Aluminium, or the oxide, as in the case of Niobium, with the feed material and trundling them together for 24 hours to produce a homogeneous mixture. This treatment appeared to have a slight adverse effect on the free-flowing properties of the feed, presumably due to a partial breakdown of particle size uniformity, though it was still possible to achieve stable feed rates and hence to grow single crystals. An alternative doping method, in which the sandy rutile particles were coated with a precipitate of Manganese Chloride, following evaporation of the aqueous salt solution, was unsuccessful, probably due to uneven doping of the feed material.

2.3 RESULTS

In practice the growth rates varied considerably from boule to boule, ranging between 1 and 6 cm. per hour, but most good boules had growth rates approaching the automatic withdrawal rate of 3 cm. per hour. By weighing the final boules and noting the drop in the hopper feed level it was found that typically about 70% of the feed was falling on the candle and contributing to crystal growth. Altogether about thirty growth runs were performed, of which nineteen (B.S. 1-19) were catalogued as being likely to produce single crystals. The final outcome was the production of three good pure boules (B.S.3, B.S. 8 and B.S. 10), two Aluminium-doped boules of nominal concentration 1000 p.p.m. (B.S. 16) and 8000 p.p.m. (B.S. 18), and two Niobium-doped boules of nominal concentration 500 p.p.m. (B.S. 12) and 200 p.p.m. (B.S. 19). All of these

boules contained regions of single crystal which were approximately 1 cm. in diameter and from 1 to 3 cm. in length. Figure 2.3 shows photographs of B.S. 12, during and after growth.

Examination of single crystals by X-ray back-reflection photography showed that the growth axis was always within 10° of < 001 > , the c axis. Also, the absence of mosaic structure and the coincidence of reflection patterns following 180° rotations of the samples showed the crystals to be relatively strain-free.

Samples of some boules were cut, washed in hydrofluoric acid and sent, together with samples of sandy rutile, for mass spectrographic (M.S. 7) analysis by Tioxide International. The results are presented in Table 2.1. Most impurities in the crystals appear to have been present in the feed material in comparable amounts. The sulphur and silicon contents of the crystals, however, are significantly higher than in the feed and it is probable that these impurities were introduced elsewhere. The silicon impurity may be due to the use of quartz tubes and funnel. The origin of the sulphur is unclear, though it may be present in the form of sulphur dioxide in the atmosphere or as an impurity in the plasma gases. Table 2.1 also demonstrates the success of the doping experiments and shows that the doping level can be closely controlled simply by varying the percentage of dopant material mixed with the feed powder.

Table 2.2 compares the M.S.7 analysis of B.S. 16 with that of a boule provided by the National Lead Company, also nominally doped with 1000 p.p.m. of aluminium, but grown by the conventional Verneuil method. In general the impurity concentrations in the plasma-grown boules are significantly lower than in the Verneuil-grown sample. Further indications of crystal purity were provided by thermoluminescence and thermally stimulated current measurements (Hillhouse, 1978), which showed the concentration of trapping centres in the plasma-grown crystals to be considerably lower than in National Lead crystals.

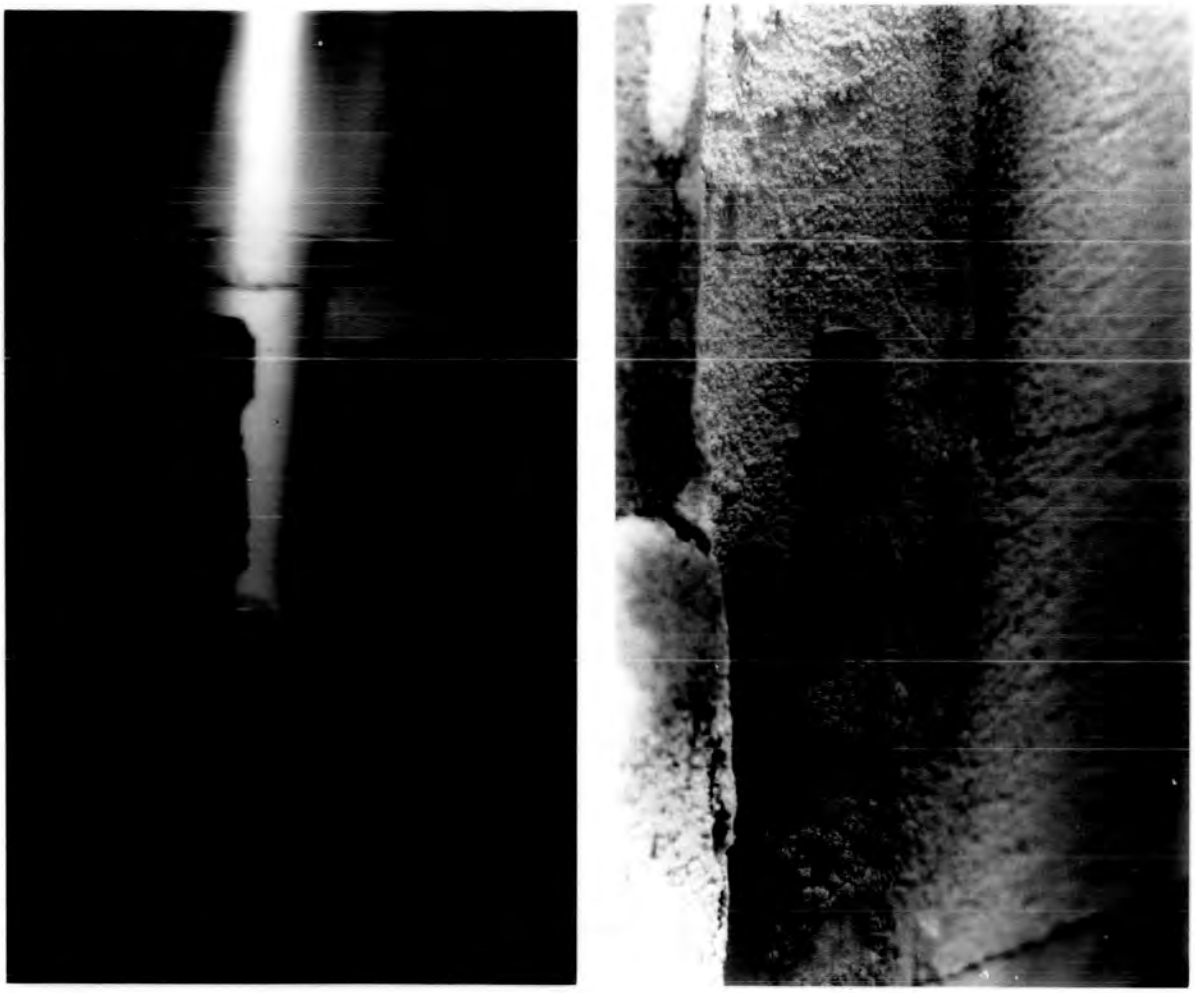

(a) (b)

Figure 2.3 : Photographs of boule B.S.12, (a) during and (b) after growth.

TABLE 2.1 : Mass spectrographic analysis (in p.p.m) of impurities in source material (DN4,5) and crystals (B.S.1-19) grown by the plasma torch technique

	CRYSTAL									POWDER	
Element	BS1	BS3	BS10	BS11	BS12	BS13	BS14	BS16	BS19	DN4	DN5
Mg	5	4	30	30	35	3	12	6	3	7	12
Al	11	15	5	50	10	4	15	1100	40	<1	1
Si	250	50	110	110	300	75	500	50	75	<50	<50
P	100	<2	<2	<2	<2	<2	2	2	90	13	13
S	150	300	700	400	1400	200	1400	700		<40	<40
K	4	4	3	7	7	3	7	7	3	14	13
Ca	30	7	7	30	10	7	10	6	4	6	6
V	0.3	0.3	0.6	0.6	≤1	0.1	0.3	0.5	0.6	0.5	0.5
Cr	≤1	0.4	0.3	0.7	≤3	0.4	0.6	0.2	<0.2	<1.5	<1.5
Mn	0.2	0.5	0.3	0.5	0.2	0.3	80	0.5	<0.1	0.2	0.4
Fe	18	27	4	25	12	5	15	3	14	2	3
Co	<2	<2	<2	<2	<2	<2	<2	2	<2	<2	<2
Cu	<1	<1	<1	<1	<1	<1	<1	≤1	<1	<1	<1
As	0.4	0.5	0.5	0.8	0.8	0.3	0.3	0.5	0.5	1.5	0.5
Sr	0.5	≤1.5				<4	0.1	≤0.6	≤0.4	<0.1	<0.1
Zr	<1	1.5	1	1.5	3	1	<1	3	1	<1	<1
Nb	4	10	5	<6	500	10	1.5	6	160	1	1
Mo	<2	3	6	10	6	2	<2	3	2	<2	<2
Sn		<1				<1	<1	<1	2	10	6
Sn		<1				<1	<1	<1	1	<1	<1
Ni		≤3				≤3	≤3	≤2	≤0.5		
Y		0.5		0.8	1.5						
Dopant				Al	Nb		Mn	Al	Nb		
Source	DN1	DN1	DN4	DN4	DN5	DN5	DN5	DN4 & 5	DN4 & 5		

TABLE 2.2 : A comparison of the impurity levels (in p.p.m) in a plasma-grown boule, B.S. 16, with a National Lead (N.L.) boule, grown by the Verneuil method. Both boules were nominally doped with 1000 p.p.m. Al.

Element	BS 16	N.L.
Mg	6	400
Al	1100	1100
Si	50	250
P	<2	130
S	700	400
K	7	8
Ca	6	14
V	0.5	1
Cr	0.2	1.5
Mn	0.5	0.3
Fe	3	20
Co	2	<6
Cu	<1	<4
As	0.5	20
Zr	3	3
Nb	6	3
Sn	<1	<2
Ni	≲2	≲5

E.S.R. measurements on these crystals will be discussed in Chapter 6.

The boules produced in runsB.S.1-15were all dark blue and this is taken as evidence of the chemical reduction undergone during growth. For all of these growth runs the tip of the feed probe was positioned about 0.5 cm. below the induction coil, but for the following run the probe was lowered approximately 1 cm. further and this had the previously mentioned effect of increasing the oxygen content in the tail of the plasma. The resulting boule, B.S. 16, was completely colourless, indicating that it was in a fully-oxidized, stoichiometric state. The following boule, B.S. 17, was grown using the same feed material as for B.S. 16, but with the probe returned to its original position and, although a good single crystal was not produced on this occasion, the final polycrystalline deposit was dark blue. Moreover, when B.S. 18 was being grown, the probe was raised from the lower position to the original position half-way through the process. This upset the delicate balance of growth conditions which had to be readjusted before crystal growth could proceed. Subsequent examination of the boule revealed two distinct regions of single crystal, separated by a grain boundary. The lower region, which was grown in the first half of the run, was colourless, but the upper region was dark blue. This suggests that the degree of reduction of the boules may be controlled by the position of the feed probe with respect to the plasma and that the main requirement in growing stoichiometric rutile crystals is a relatively large oxygen content in the gases incident on the growing crystal. The electrical resistivity of cut and polished samples were measured using a model 602 Keithley electrometer, with Ohmic contacts formed by evaporated Ag. The resistivity of stoichiometric samples were typically 10^{14} Ω cm, while the reduced samples had resistivities of 10^{-2} to 10 Ω cm. Oxidation of the non-stoichiometric crystals increased the resistivity to about 10^{12} Ω cm, suggesting that reduction during growth is only partially reversible and that full stoichiometry can only be achieved by growing the crystals in an oxidising environment.

CHAPTER 3

PRINCIPLES OF E.S.R

3.1 INTRODUCTION

All branches of spectroscopy involve the determination of energy level separations by exciting transitions between the levels with incident radiation of known wavelength and then detecting the resulting changes in the intensity of the output radiation. The particular case of electron spin resonance (e.s.r) spectroscopy concerns transitions between the energy splittings which are caused by an unpaired electron's interaction with an external magnetic field, with nuclear spins and with surrounding atoms. Since materials which contain these unpaired electrons are paramagnetic, e.s.r. is also referred to as paramagnetic resonance.

For the magnitude of homogeneous magnetic fields that may easily be obtained in the laboratory ($\sim$ 1 tesla) the induced energy level splittings are typically about 1 cm^{-1}, and hence the appropriate radiation which is required to promote transitions between the levels is in the microwave region of the electromagnetic spectrum. The basic aim of an e.s.r. measurement, therefore, is to detect the absorption of power from a microwave beam by a paramagnetic sample during resonance. Unlike most forms of spectroscopy, in which the energy of the radiation is varied to match the relevant energy level splittings, it is experimentally more convenient to keep the microwave frequency fixed and to vary the energy level separations by sweeping the external magnetic field through the resonance condition.

This chapter is intended to be an introduction to the fundamental principles of e.s.r. The detailed theory has been covered in several standard texts, e.g. Pake (1962), Assenheim (1966), Ayscough (1967).

3.2 PARAMAGNETISM

Electrons in all materials may be considered as possessing two types of motion, giving rise to (a) orbital angular momentum, due to motion around the nucleus of an atom and (b) an intrinsic spin angular momentum corresponding to the electron spinning about its own axis. Since electrons possess charge both types of motion produce magnetic moments and hence, in an external magnetic field, the electrons behave as magnetic dipoles with a tendency to align themselves to the direction of the field. In most materials the electrons are arranged in pairs of opposing spins so that there is no net magnetic moment and hence the materials are classified as diamagnetic. There are several classes of materials,however, in which unpaired electrons can exist, causing an overall magnetic moment which gives rise to paramagnetism. Such materials are :-

(a) transition metal and rare earth compounds, where incomplete d or f orbitals may leave one or more electrons unpaired

(b) free radicals, where a bonding electron is left associated with only one atom.

(c) F-centres, in which electrons or holes are trapped at point defects.

(d) atoms or molecules which possess an odd number of electrons.

(e) metals and semiconductors, in which the conduction electrons can cause paramagnetism.

3.3 ENERGY LEVELS IN A MAGNETIC FIELD

Quantum theory states that the angular momentum, and hence also the magnetic moment, of the electron may only hold certain discrete values. With the simplest case of a single free electron, with no orbital angular momentum, the spin-only angular momentum is given by :-

$$P_s = \frac{1}{2} \frac{h}{2\pi} \qquad (3.1)$$

and the magnetic moment is :-

$$\mu_s = \beta = \frac{eh}{4\pi mc} \qquad (3.2)$$

In the presence of an external magnetic field the electron experiences a torque which tries to align its magnetic moment vector with the direction of the field, but quantisation restricts the number of possible orientations, so that the magnetic moment can never be completely parallel to the field, but instead it precesses around the field direction at an angular frequency, ω_o, where :-

$$\omega_o = \gamma \, Ho \qquad (3.3)$$

Ho is the magnetic field value and γ is the magnetogyric ratio and is 17.6×10^6 sec^{-1} $Gauss^{-1}$ for a free electron. The energy of a magnetic dipole of moment μ in the presence of a magnetic field Ho is given by :-

$$E = \mu \, Ho \cos \theta \qquad (3.4)$$

where θ is the angle between the magnetic field and the axis of the dipole. In the case of a free electron there are only two allowed orientations of magnetic moment, corresponding to magnetic quantum numbers, Ms, of $\pm\frac{1}{2}$, and there are consequently only two permitted energy levels, E , described by :

$$E = 2 \beta M_s Ho \qquad (3.5)$$

Thus the application of a magnetic field splits the previously-degenerate electron energy level into two different levels, separated by energy 2β Ho.

In real systems, where the magnetically-induced energy splittings may be affected by additional interactions, the relation of energy to

magnetic field is given by :-

$$E = g \beta Ho \tag{3.6}$$

where g is a numerical factor which is determined experimentally. (Due to relativistic corrections, g = 2.0023 for a free electron).

3.4 INTERACTION WITH RADIATION

In order to detect these splittings in the electron energy levels it is necessary to excite a transition between two levels with e.m. radiation of frequency ν , such that :-

$$h \nu = g \beta H_o \tag{3.7}$$

The mechanism by which the radiation induces a transition is also of a magnetic nature and may be thought of as being due to the oscillating magnetic field component of the e.m. radiation exerting an additional torque on the electron's magnetic moment, causing it to change direction and hence its energy when the microwave frequency is equal to the magnetic moment's precession frequency. In practice, the excitation of transitions by the microwave beam will take place over a range of frequencies on either side of the resonant value or, in the normal experimental set-up with a fixed microwave frequency, interaction occurs over a range of magnetic field values, so that when the field is slowly swept through the resonance condition, while the amount of reflected power is measured, an absorption line of finite width is produced.

Since there is an equal probability of an interaction between the microwave beam and an electron causing either an absorption or emission of power, the ability to detect such transitions relies on there being an excess population of electrons in the lower energy state. The relative populations

of the energy levels is given by a Boltzman distribution :-

$$\frac{n_1}{n_2} = \exp\left(\frac{-g\ \beta\ H_o}{kT}\right) \tag{3.8}$$

where n_1 and n_2 are the populations of the upper and lower energy states respectively. The net power absorption, therefore, increases as the temperature is lowered, causing an increase in e.s.r. signal-to-noise ratio.

To a first approximation, the population difference, $\Delta n = n_2 - n_1$, between the two energy levels may be expressed as :-

$$\Delta n = \frac{Ng\ \beta\ H_o}{2kT} \tag{3.9}$$

where N is the total concentration of unpaired electrons. Integration of the detected absorption line gives a measure of the total net power absorbed, P, which is given by

$$P = \frac{2\ \pi^2\ \nu^2\ H_o^2\ S(S+1)\ Ng^2\ \beta}{3kT} \tag{3.10}$$

where S is the total spin angular momentum. Hence the total amount of power absorbed is proportional to the total number of unpaired electrons in the sample.

3.5 RELAXATION

The interaction of radiation with the energy level system would rapidly bring about an equalisation of the populations and hence an end to the net absorption of power, were it not for the existence of a mechanism by which the electrons in the higher energy state can lose their excess energy to the surrounding lattice to retain the equilibrium population distribution. This spin-lattice relaxation process is

characterised by a relaxation time, T_1, which is the time for a spin system to lose $\frac{1}{e}$ of its excess energy. When T_1 is relatively short, as for example,is often found with transition metal ions, the equilibrium state of the spin system is easily maintained during resonance, though transitions may take place over a wide energy range, producing relatively broad resonance lines which can be difficult to detect. Since T_1 is inversely proportional to temperature, the width of resonance lines decrease as the temperature is reduced and this provides another advantage in performing e.s.r. measurements at cryogenic temperatures. Materials which have relatively long spin-lattice relaxation times, such as free radicals, give rise to narrow e.s.r. lines, but may be more susceptible to the problem of saturation of the spin system if the incident power is of sufficient magnitude that the equilibrium population distribution can no longer be maintained. This leads to a decrease in the population difference and consequently to a fall in the e.s.r. signal intensity. Due to the temperature dependence of T_1, saturation effects become more prominent as the temperature is lowered.

An alternative relaxation mechanism is by a spin-spin interaction with other defect centres. Spin-spin relaxation times, T_2, are usually shorter than spin-lattice times, and are relatively independent of temperature. The lineshape of an absorption signal is governed by the relaxation mechanism. If spin-lattice relaxation dominates the lineshape is approximately Gaussian, but if spin-spin relaxation is the main mechanism the absorption line is more Lorentzian in shape, and is also more susceptible to power saturation effects.

3.6 THE SPIN HAMILTONIAN

The discussion so far has mainly referred to the simple case of a free electron and its interaction with a magnetic field, since this enables the basic principles of magnetic resonance to be more readily understood. In practice, when a paramagnetic ion exists in a real chemical environment, there are many other interactions which may govern the electron energy

levels. The combined effects of these interactions may be expressed as terms, of decreasing magnitude, in a general Hamiltonian.

$$\mathcal{H} = \mathcal{H}_{V} + \mathcal{H}_{LS} + \mathcal{H}_{SH} + \mathcal{H}_{SI} + \text{smaller terms} \quad (3.11)$$

$\mathcal{H}_{V}$ is the effect of the crystal field into which the ion is placed and may be described by :-

$$\mathcal{H}_{V} = \sum_{i} e_{i} \quad V(r_{i}) \quad (3.12)$$

where $V(r_i)$ is the electrostatic potential at each surrounding ion. $\mathcal{H}_{LS}$ is the spin-orbit coupling term and represents the interaction between the orbital (L) and spin (S) angular momenta.

$$\mathcal{H}_{LS} = \lambda \underline{L}. \ \underline{S} \quad (3.13)$$

where λ is the spin-orbit coupling parameter. $\mathcal{H}_{SH}$ is the interaction of the electrons with external magnetic field.

$$\mathcal{H}_{SH} = \beta(\underline{L} + 2\underline{S}) \quad H \quad (3.14)$$

$\mathcal{H}_{SI}$ is a magnetic interaction between the electrons and nuclear magnetic moments.

$$\mathcal{H}_{SI} = A.\underline{I}.\underline{S}. \quad (3.15)$$

where A is the hyperfine splitting constant.

Placing a free ion into a crystal lattice usually has the effect of causing a partial or complete lifting of the orbital state degeneracy, since the orbitals are distorted to different extents by the electric fields

of the neighbouring ions. In general, a single orbital level is left as the ground state, which is then degenerate only in spin, so that the orbital motion can have no direct interaction with the magnetic field. Spin-orbit interactions, however, allow some admixing of higher orbital states, which may lead to zero-magnetic-field splittings of the spin states and departures from free-electron g-values.

The effects of the various interactions on the lower spin energy levels can be represented by a Spin Hamiltonian, which is derived (see e.g. Carrington, 1960) using first order perturbation theory. The Spin Hamiltonian is a method of describing the behaviour of the spin system, as observed by e.s.r., in which the effect of the orbital angular momentum is replaced by an anisotropic coupling between the electron spin and the external magnetic field.

$$\mathcal{H} = \beta(g_z H_z S_z + g_x H_x S_x + g_y H_y S_y) \qquad (3.16)$$

Thus the angular variation of the resonant magnetic field is a reflection of the angular variation of the surrounding crystal field.

To apply the concept of the Spin Hamiltonian to systems with more than one unpaired electron, i.e. $S > \frac{1}{2}$, it is necessary to extend to second order perturbation in order to include terms in S^2 which are independent of the magnetic field. The resulting Spin Hamiltonian for the general case of orthorhomic symmetry, including nuclear hyperfine interactions, is :-

$$\mathcal{H} = \beta(g_z H_z S_z + g_x H_x S_x + g_y H_y S_y) + AS_z I_z + BS_x I_x + CSy\ Iy + D\left[S_z^2 - \frac{1}{3}S(S+1)\right] + E(Sx^2 - Sy^2) \qquad (3.17)$$

The Spin Hamiltonian parameters, g, A, B, C, D and E may be determined experimentally by measuring the angular variation of resonance magnetic fields. For axial symmetry $g_z = g_{//}$, $g_x - g_y = g_{\perp}$, C = B, E = O. For cubic symmetry $g_x = g_y = g_z = g$, A = B = C, D = E = O.

Kramers theorem states that for a system containing an odd number of unpaired electrons a purely electrostatic field cannot completely remove the degeneracy of any level, so that, in principle, e.s.r. can be observed in all such systems. When an ion has an even number of unpaired electrons, however, it is possible that the crystal field may completely lift the degeneracy of the ground state to produce large zero-magnetic field splittings of spin levels. If the energy splittings are of significantly greater magnitude than the available microwave energy, it is no longer possible to excite electron spin resonance transitions.

3.7 INTERPRETATION AND APPLICATIONS

Successful interpretation of e.s.r. spectra can lead to fairly detailed models for the relevant paramagnetic centres, by providing information on the charge state, the type of binding, the amount of interaction with surrounding nuclei and the symmetry of the environment.

The value of the g-parameter and the magnitude of its departure from the free electron value gives an indication of the strength of the crystal field and the degree of spin-orbit coupling. The anisotropy of the g-value reflects variations in crystal field and hence can be used to deduce information concerning the defect site and the crystal structure. The identification of a defect or its surrounding nuclei can be particularly precise if there are electron-nuclear interactions, giving hyperfine structure to the spectra. The magnitude of the hyperfine splitting is proportional to both the nuclear magnetic moment and the probability of finding the electron at the nucleus.

Since the area under an absorption line is proportional to the number of unpaired spins, e.s.r. can be used as a sensitive, non-destructive

method of determining defect concentrations, providing care is taken with calibration procedures and the signal is not saturated by excessive power.

E.s.r. is one of the most powerful tools available for the study of defects in insulators, because it can only detect the presence of paramagnetic centres and therefore obtains results independently of surrounding diamagnetic material, which would swamp signals from low concentration centres in less selective techniques. E.s.r. has been used to study defects which are introduced into a crystal lattice by irradiation or dislocation. The charge state of trapping centres can often be deduced from the sign of Δg, the difference from the free electron g-value, which is negative for an electron trap but positive for a hole trap. The technique has been widely applied to the characterisation of impurity centres, such as those deliberately doped into single crystals to produce maser materials. Apart from the initial analysis of an e.s.r. spectrum to establish the identity of a defect, measurements of the variation of spectral intensity with time can be used to study reaction rates, e.g. the rates at which defects recombine after irradiation (Bartram,, 1976).

CHAPTER 4

PROPERTIES OF RUTILE : A REVIEW

4.1 GENERAL PROPERTIES AND STRUCTURE

Titanium dioxide can exist in three polymorphic forms, namely Anatase, Brookite and Rutile, though the first two forms are metastable and can be irreversibly transformed to rutile by heating to 1000° C and 850° C respectively (Shannon, 1965). Fully stoichiometric rutile is an insulator with a band gap of 3.0 eV and is transparent to radiation of wavelength greater than about 4100 Å which gives it a colourless appearance. The major application of rutile as a pigment in the manufacture of white paint is due to its high refractive index (De Vore, 1951) and excellent light scattering properties, which have also led to the production of gemstones, from single crystals of rutile, with fire and brilliance superior to those of diamonds, (Moore, 1948). Many of the general properties of rutile have been summarized in reviews by Cronemeyer (1952), Grant (1959) and Frederickse (1961).

The rutile structure consists of a body-centred tetragonal sublattice of Ti^{4+} ions, with each cation surrounded by a slightly distorted octahedron of O^{2-} anions (Fig.4.1). Each O^{2-} ion is associated with three co-planar Ti^{4+} ions. The lattice parameters of the tetragonal unit cell are a = b = 4.594 Å and c = 2.959 Å (Baur, 1956). The two Ti^{4+} ions in each unit cell are situated at (0,0,0) and $(\frac{1}{2},\frac{1}{2},\frac{1}{2})$ and the four oxygen ions are at (x,x,0), (-x,-x,0), $(\frac{1}{2}+x, \frac{1}{2}-x, \frac{1}{2})$ and $(\frac{1}{2}-x, \frac{1}{2}+x, \frac{1}{2})$, where x = 0.306.

The structure may also be visualised as an ABABA layer structure along the c axis, with each A layer composed of parallel -O-O-Ti-O-O-Ti-chains along the <110> axis and each B layer consisting of similar chains along

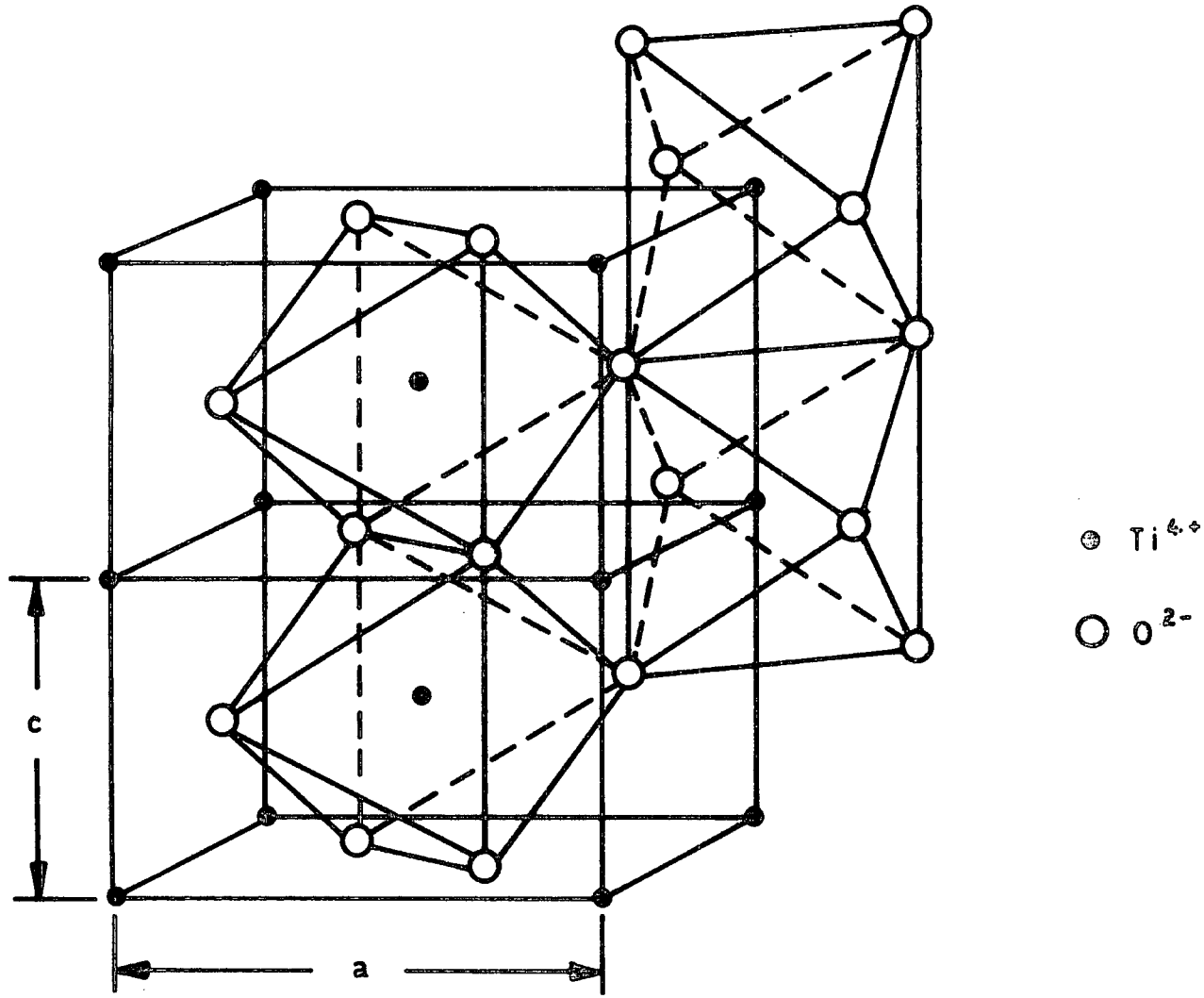

FIG.4·1 Crystal structure of rutile, TiO_2, (after R.G. Breckenridge)

the <1$\bar{1}$0 > axis. The repeat distance along the chains is $\sqrt{2}$ a. The separation between adjacent chains in the same layer is $\frac{a}{\sqrt{2}}$ and the repeat distance normal to the layer is c. Thus the octahedron of O^{2-} ions that surrounds each Ti^{4+} ion, e.g. at ($\frac{1}{2}$,$\frac{1}{2}$,$\frac{1}{2}$), is composed of the two neighbouring anions in the same <1$\bar{1}$0> chain at ($\frac{1}{2}$ + x,$\frac{1}{2}$ - x, $\frac{1}{2}$) and ($\frac{1}{2}$ -x,$\frac{1}{2}$ + x,$\frac{1}{2}$), together with two ions from each of the <110> chains in adjacent layers, i.e. (x,x,0), (1-x,1-x,0), (x,x,1) and (1-x,1-x,1). The oxygen ion octahedron is slightly distorted in two ways. First there is a slight stretch along the direction of the chain containing the centre Ti^{4+} ion, so that the lengths of the two Ti-O bonds along that axis are greater than the other four bondlengths. In addition there is a compression of the square formed by these latter four ions which results in the O-Ti-O angle which is bisected by the c-axis being smaller than its supplement (see Fig.4.2). Because of these distortions, the titanium ion site retains only orthorhombic (D2h) symmetry, with 2-fold rotational axes along the <110> , <1$\bar{1}$0> and <001> axes. The environments of the two titanium sites in each unit cell, however, are equivalent except for a rotation of 90^{o} about the c-axis (the ion chains through Ti^{4+} ions at (0,0,0) and ($\frac{1}{2}$,$\frac{1}{2}$,$\frac{1}{2}$) being along the <110> and < 1$\bar{1}$0> axes respectively) so that overall the structure has 4-fold symmetry about the <001> axis, but only 2-fold symmetry about <110> and <100> type axes.

4.2 IMPURITIES IN RUTILE

There are two main types of site in the rutile lattice which may be occupied by impurity ions. The first is a substitutional site in which the impurity ion replaces a Ti^{4+} ion and there are therefore two such sites per unit cell (see Fig.4.3). It has been found that the majority of impurity ions which have been doped into rutile crystals have favoured the substitutional site, e.g. Fe, Cr, Mn, Co, Nb. The alternative is an interstitial site, of which there are four per unit cell (see Fig.4.4), at (0,$\frac{1}{2}$,0), ($\frac{1}{2}$,0,0),(0,$\frac{1}{2}$,$\frac{1}{2}$) and ($\frac{1}{2}$,0,$\frac{1}{2}$). These interstitial sites are also surrounded by a distorted octahedron of O^{2-} ions, though in this case their relative orientations are such that the four sites differ by rotations of $\pm\ \alpha$ and $90^{o} \pm \alpha$ about the c axis,

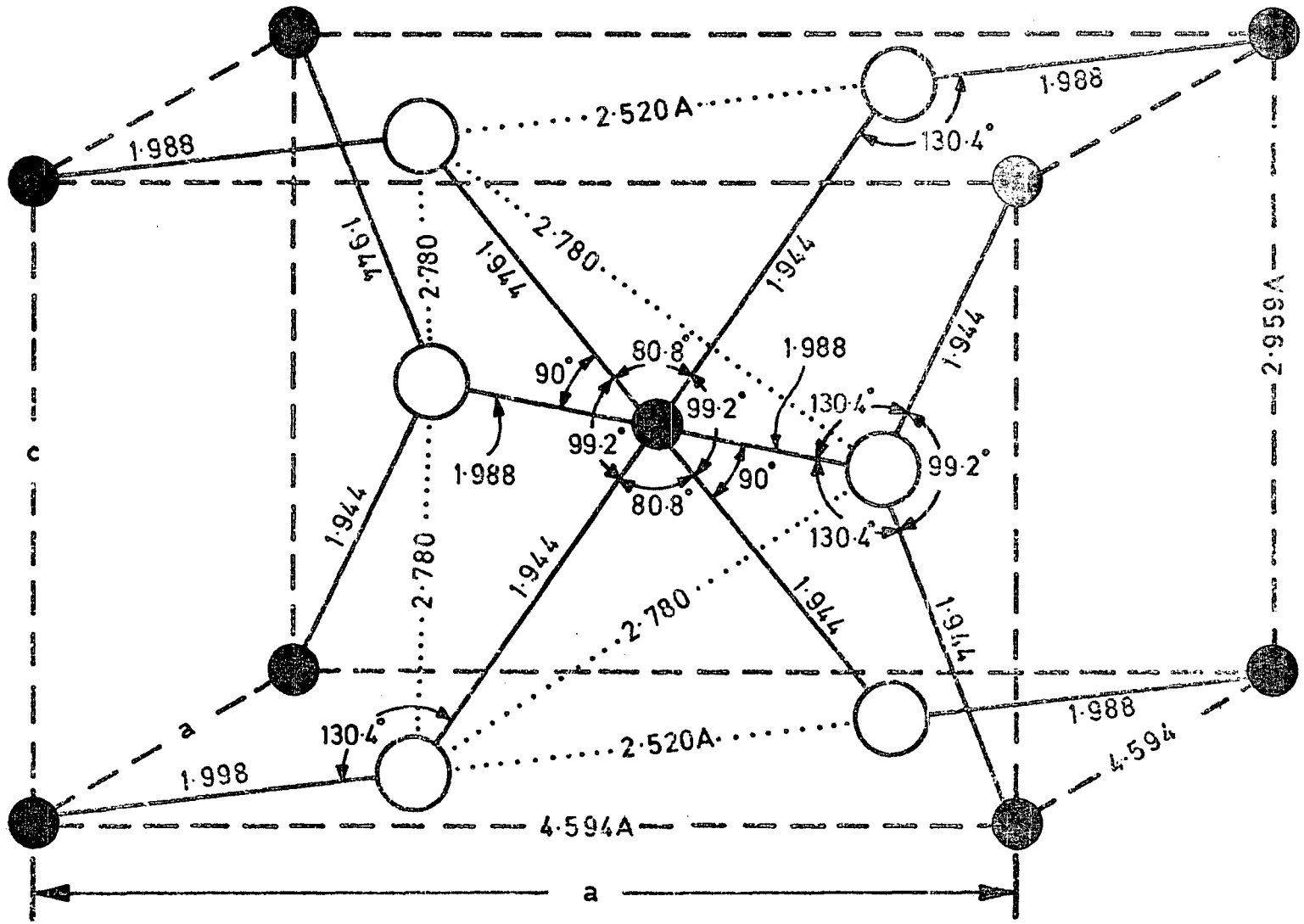

FIG.4·2 UNIT CELL OF RUTILE,
(AFTER VON HIPPEL)

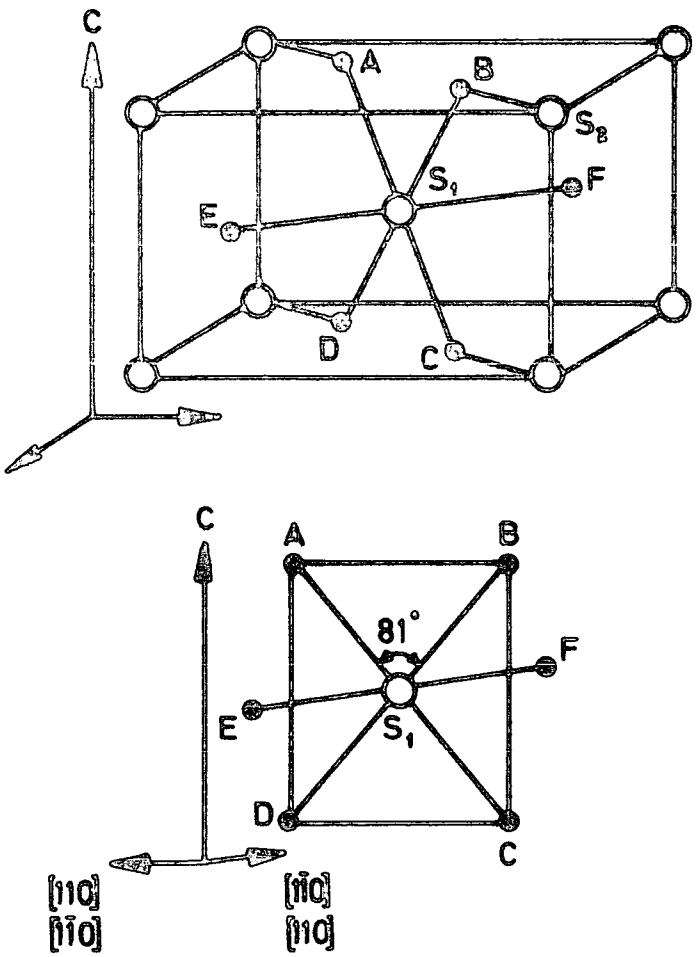

SA = SB = SC = SD = 1·94A

SE = SF = 1·99A

○ = Ti^{4+}

● = O^{2-}

FIG 4·3 PART OF RUTILE LATTICE SHOWING THE TWO SUBSTITUTIONAL POSITIONS.

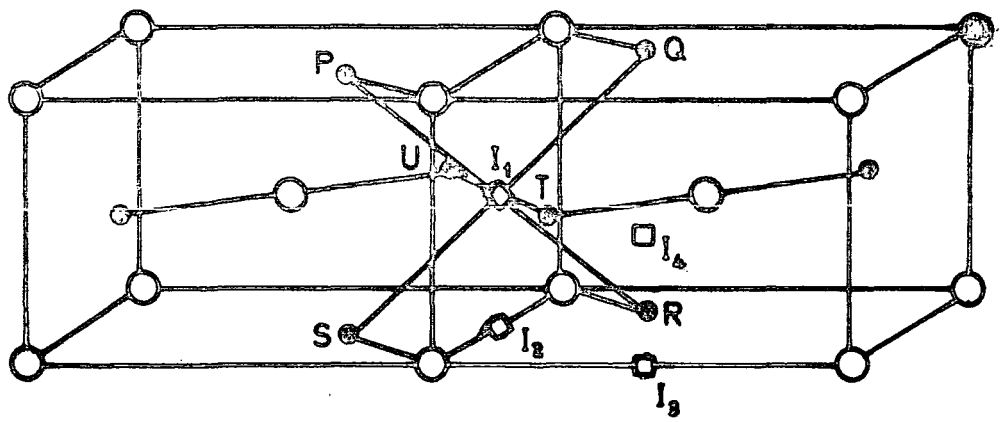

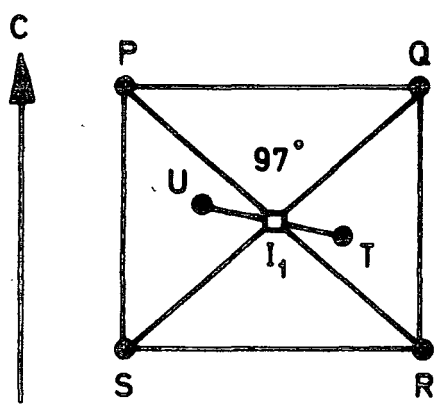

IP = IQ = IR = IS = 2·23A

IU = IT = 1·67A

□ = INTERSTITIAL SITE

FIG.4·4 PART OF RUTILE LATTICE SHOWING THE FOUR INTERSTITIAL POSITIONS

where $\alpha \sim 12.5^{\circ}$. The interstitial site has a slightly larger volume than the substitutional site and purely geometrical considerations suggest that the former is more likely to be occupied by ions of radius greater than 0.73 Å. Nickel and copper have been shown to favour the interstitial site.

The spatial arrangement of the octahedral interstitial sites in stacks along the c axis, e.g. $(0,\frac{1}{2},0)$, $(0,\frac{1}{2},\frac{1}{2})$, $(0,\frac{1}{2},1)$ etc. gives rise to the existence of relatively open channels parallel to the c axis (Huntington,1965), which allow a very rapid but highly anisotropic diffusion, at temperatures greater than $\sim 800^{\circ}$ C, of species with ionic radii less than ~ 0.75 Å. This property of the rutile structure has been exploited (Wittke, 1966) to give a useful alternative method of doping rutile crystals, other than growing boules from impurity-mixed starting material.

Huntington (1965) also proposed the existence of 4 tetrahedral interstitial sites per unit cell, at $(\frac{1}{2},0,\frac{1}{4})$, $(\frac{1}{2},0,\frac{3}{4})$, $(0,\frac{1}{2},\frac{1}{4})$ and $(0,\frac{1}{2},\frac{3}{4})$, though to date there have been no reports of this site being occupied by any impurity ions.

4.3 ESR STUDIES OF IMPURITIES IN RUTILE

Pure rutile is diamagnetic and its relatively anisotropic structure makes it a suitable host lattice for the incorporation of dopant paramagnetic ions to form masers. Much of the early work on doping impurities into rutile and the subsequent characterisation by e.s.r. methods was carried out as part of a comprehensive search for new maser materials (Gerritsen, 1960), (Schollmeier, 1967), and has been summarized in a review by Low and Offenbacher (1965).

In addition to information about such parameters as the charge state and nuclear hyperfine interactions that can usually be gathered from e.s.r. measurements, the anisotropic nature of the rutile structure means that it has often been possible to determine the lattice site of paramagnetic centres and sometimes also the relative location of other neighbouring point defects by studying isofrequency diagrams of e.s.r. spectra and relating their

angular variation to the symmetry properties of the crystalline structure.

Since there are two Ti^{4+} substitutional sites per unit cell which differ only by translation and rotation about the c axis, for an arbitrary orientation of an external magnetic field the two sites will experience different crystal fields along that magnetic field direction and hence paramagnetic centres at these sites will undergo different magnetically-induced splittings of their energy levels. This results in magnetic resonance occurring at two different field values to produce two e.s.r. absorption lines. The separation of the lines reaches a maximum when the magnetic field is directed along a <110> type axis, when it is then parallel to different principal magnetic axes at each of the two types of substitutional site. As the field direction varies, the absorption lines converge until, at all axes in the (100) and (010) planes (i.e. including the < 100 > , < 010 > and < 001> directions), the two sites are magnetically equivalent, the energy level splittings become identical and the resonance lines coincide.

The e.s.r. spectra of a defect on an oxygen substitutional site, e.g. an F-centre, will have the same symmetry properties as one from a titanium site, since although there are four O^{2-} sites per unit cell, it is only possible to distinguish two different sites with e.s.r. measurements, as pairs of sites, e.g. (x,x,0) and (-x,-x,0) have identical principal magnetic axes, along the <110 > , $< 1\bar{1}0 >$ and < 001 > crystalline directions, which differ from those of the other two sites, at ($\frac{1}{2}$ + x, $\frac{1}{2}$-x, $\frac{1}{2}$) and ($\frac{1}{2}$ - x, $\frac{1}{2}$ + x, $\frac{1}{2}$) only by a 90° rotation about the < 001 > axis. All paramagnetic defects on substitutional sites, therefore, give rise to e.s. r. spectra which display a 90° periodicity about the < 001 > axis.

A defect which occupies the octahedral interstitial site will generally exhibit four e.s.r. absorption lines for an arbitrary orientation

of the crystal with respect to the magnetic field. The field separation of the lines is a maximum when the field direction is $\sim 12.5^{o}$ from <110> type axes, in the (001) plane, though this angle may vary for different defects, since they will distort the surrounding lattice to differing extents. When the field is parallel to < 110 > and < 100> type axes, different pairs of sites become magnetically equivalent, resulting in two absorption lines, and when the magnetic field coincides with the <001> axis all four sites become magnetically indistinguishable, to give only one resonance line.

E.s.r. spectra of greater multiplicity may be encountered when the local crystal field at one of the above mentioned sites is perturbed by the presence of a neighbouring point defect. A maximum of eight different magnetic complexes may be distinguished in one unit cell, to give eight absorption lines for an arbitrary field orientation, two lines when parallel with < 110 > , < $1\bar{1}0$> , < 100 > and < 010 > axes, and again only one line when parallel to the < 001 > axis. The magnetic axes of the main defect, which may be deduced from the angular variation of the e.s.r. spectrum, may also suggest the relative location of the perturbing defect.

The e.s.r. line multiplicity that may be expected from different sites at specific magnetic field orientations are given in Table 4.1. The following section summarizes the e.s.r. data relating to impurities in rutile, together with other relevant results. The spin Hamiltonian parameters for the various spectra are presented in Table 4.2.

4.3.1 Chromium

Chromium-doped rutile was first studied by Gerritsen (1959), who deduced that Cr^{3+} substitutes for Ti^{4+}. Cr^{3+} is a $3d^{3}$ ion in which the singlet orbital ground state energy level is split by the crystal field into two Kramers doublets, separated by 1.43 cm^{-1} in zero magnetic field. Application of a magnetic field then splits the doublets by differing

TABLE 4.1

Multiplicity of e.s.r. lines exhibited by a $S = \frac{1}{2}$, $I = 0$ centre for different site symmetries at various orientations of crystal axes with respect to the external magnetic field.

Site \ Axis	<001>	<100>	<010>	<110>	<1$\bar{1}$0>	Arbitrary
Ti or O substitutional	1	1	1	2	2	2
Octahedral interstitial	1	2	2	2	2	4
Lower symmetry	1	2	2	2	2	8

TABLE V.3 E.S.R. Parameters of Impurity Ions in Rutile

Ion	g_{110}	$g_{1\bar{1}0}$	g_{001}	D	E	Other Data Remarks	Site	Reference
Cr^{3+}	1.97	1.97	1.97	0.55 cm^{-1}	0.27 cm^{-1}	A= 1.5×10^{-4} cm^{-1}	Subst.	Gerritsen(1959)
Cr^{5+}	1.928	2.105	1.976				Subst.	Sochava(1972)
Fe^{3+}	2.000	2.000	2.000	20.38 GHz	2.06 GHz	a=0.84 GHz, F = 0.68 GHz	Subst.	Lichtenburger (1969)
Ni^{2+}	g_x=2.10	g_z=2.20	2.10	-25 GHz	4.125 GHz	x,z are $\sim 5^{\circ}$ from<110>in the (001) plane.	Inter-stitial	Gerritsen(1962)
Ni^{3+}	g_x=2.085	g_z=2.254	2.085			x,z are $\sim 9^{\circ}$ from<110>in the (001) plane.	Inter-stitial	" "
Ni^{3+}	2.050	2.272	2.237				Subst.	" "
Mn^{4+}	1.99	1.99	1.99	12.1 GHz	3.88 GHz	A = 215 MHz	Subst.	Andresen(1961)
Mn^{3+}	2.00	2.00	1.99	-3.4 cm^{-1}	0.116cm^{-1}	A_{110} = 84.5 x 10^{-4} cm^{-1} $A_{1\bar{1}0}$ = 52.8 x 10^{-4} cm^{-1} A_{001} = 80.6 x 10^{-4} cm^{-1}	Subst.	Gerritsen(1963)
Co^{2+}	2.19	5.88	3.75				Subst.	Yamaka(1962)
V^{4+}	g_x=1.986	g_y=1.993	g_z=1.941			A_x = 45.4 x 10^{-4} cm^{-1} A_y = 60.5 x 10^{-4} cm^{-1} A_z = 111.4 x 10^{-4} cm^{-1}	Inter-stitial	Kubec (1972)
V^{4+}	1.915	1.956	1.913			A_x = 31 x 10^{-4} cm^{-1} A_y = 43 x 10^{-4} cm^{-1} A_z = 142 x 10^{-4} cm^{-1}	Subst.	Gerritsen(1960)

Ion	g_{110}	$g_{1\bar{1}0}$	g_{001}	D	E	Remarks	Site	Reference
Cu^{2+}	2.109	2.346	2.094			$A_{x_1}=19\times10^{-4}cm^{-1}$ $A_{x_2}=19\times10^{-4}cm^{-1}$ $A_{y_1}=27\times10^{-4}cm^{-1}$ $A_{y_2}=29\times10^{-4}cm^{-1}$ $A_{z_1}=-87\times10^{-4}cm^{-1}$ $A_{z_2}=-94\times10^{-4}cm^{-1}$	Subst.	Ensign(1969)
Nb^{4+}	1.981	1.973	1.448			$A_x = 1.66 \times 10^{-4} cm^{-1}$ $A_y = 7.93 \times 10^{-4} cm^{-1}$ $A_z = 2.32 \times 10^{-4} cm^{-1}$	Subst.	Zimmerman (1973)
Mo^{3+}	1.95	1.97	1.94	5.58 cm^{-1}	0.99 cm^{-1}		Subst.	Ohlsen(1973)
Mo^{5+}	1.8155	1.9167	1.7923				Subst.	Chang (1964)
W^{5+}	1.4725	1.5944	1.4431			$A_x = 41 \times 10^{-4} cm^{-1}$ $A_y = 64 \times 10^{-4} cm^{-1}$ $A_z = 92 \times 10^{-4} cm^{-1}$	Subst.	Chang (1966)
Ta^{4+}	1.979	1.979	1.945			$A \sim 2.5 \times 10^{-4} cm^{-1}$	Subst.	Chester(1961)
Pt^{3+}	1.9777	1.9743	1.9436				Subst.	Chandrashekhar (1976)
Ce^{3+}	2.06	4.39	3.86				Subst.	Chester (1961)

amounts so that in general two transitions are observed (giving four absorption lines for an arbitrary field orientation). The lines are relatively narrow even at room temperature, enabling the detection of hyperfine splitting from the I = 3/2, Cr^{53} isotope (9.5% natural abundance). Although it was concluded that most of the chromium in rutile is in a trivalent state, it was also realised that it might not be possible to detect other Cr oxidation states (Cr^{2+} or Cr^{4+}) by e.s.r. if the zero magnetic field splittings were too large. Mirlin (1970) has suggested that some of the Cr^{3+} ions can be converted to Cr^{4+} by annealing the sample in an electric field, a view that was supported by Sochava (1972) in reporting a weak e.s.r. spectrum which was produced by the same technique and assigned to Cr^{5+} (3d').

Since a Cr^{3+} ion on a Ti^{4+} site has a negative charge with respect to the lattice there must also exist other defects of opposite polarity in order to retain overall charge neutrality. Such defects could be interstitial titanium or chromium, or oxygen vacancies. Analysis of relatively weak e.s.r. signals in heavily chromium-doped rutile crystals (Ikebe, 1969) showed that, in addition to the main substitutional Cr^{3+} spectrum, there were two other spectra, the angular variations of which, suggested that they represented complexes of substitutional Cr^{3+} with 2nd and 3rd nearest neighbour oxygen vacancies respectively. This shows that a small percentage of the Cr^{3+} ions are locally charge-compensated. Sochova (1970) found that the intensity of a Cr^{3+}-oxygen vacancy spectrum was increased by mild chemical reduction of the crystal, presumably due to the creation of more vacancies near previously unperturbed Cr^{3+} ions. Stronger reduction, however, had the effect of decreasing the spectral intensity while giving rise to an optical absorption band. This behaviour was interpreted as due to electrons being trapped at some of the oxygen vacancies.

4.3.2 Iron

Early e.s.r. studies (Carter, 1960) showed that iron also occupies a Ti^{4+} substitutional site in the rutile lattice in a trivalent state. Fe^{3+} has a $3d^5$ electronic configuration with a 6-fold degenerate singlet orbital ground state, which is split into three Kramers doublets by the crystal field, with zero-magnetic field splittings of 2.68 and 1.43 cm^{-1} which prevent transitions occurring between the different doublets, except at very high magnetic fields or microwave frequencies. At X-band frequencies only two transitions are usually observed, the lines being relatively narrow and easily detected at room temperature.

Because Fe^{3+} has a half-filled electronic shell ($3d^5$), it is an S-state ion with zero orbital angular momentum, so that there can be no significant spin-orbit coupling and the g-value is very close to 2. It is therefore necessary to turn to still higher orders of perturbation and introduce terms in S^4 in order to produce a complex spin Hamiltonian which will describe the observed energy splittings :-

$$\mathcal{H} = g\ \underline{H}\cdot\underline{S} + D\left(S_z^2 - \frac{35}{12}\right) + E\left(S_x^2 - S_y^2\right)$$

$$+ \frac{a}{b}\left(S_x^4 + S_y^4 + S_z^4 - \frac{707}{16}\right) + \left(\frac{7}{36}\right) F\left[S_z^4 - \left(\frac{94}{14}\right) S_z^2 + \frac{81}{16}\right] \qquad (4.1)$$

Iron has not been reported in any other oxidation state in rutile, though this may simply be due to other states, e.g. Fe^{2+} and Fe^{4+}, being invisible to e.s.r. detection and in fact the existence of valencies other than the trivalent state has been inferred (Sandin, 1969) from specific heat measurements. Johnson (1968) suggested that some iron may form as metal precipitates which impart a red-brown colour to rutile crystals.

Several extra e.s.r. spectra have been observed in Fe-doped rutile (Anderson, 1973) and assigned to complexes of substitutional Fe^{3+} with other nearby point defects. One was identified as Fe^{3+} with a nearest neighbour oxygen vacancy, another as Fe^{3+} associated with a proton in an interstitial site and a third spectrum was tentatively attributed to a Fe^{3+}-interstitial Ti^{3+} complex. The nature of the defect pairs suggest that Fe^{3+} has a stronger affinity than Cr^{3+} for positively charged defects in the rutile lattice.

When studying a rutile crystal which had been co-doped with iron and molybdenum, Faughnan (1968) observed that irradiating the crystal with 0.39- 0.43 μm radiation at 77 K had the effect of decreasing the intensity of the Fe^{3+} e.s.r. signal, increasing the Mo^{5+} signal intensity and also of inducing increased optical absorption at $\sim$ 20,000 cm^{-1}. This photochromism was then interpreted as due to a charge transfer mechanism of the type :-

$$Fe^{3+} \longrightarrow Fe^{4+} + e^{-} \qquad (4.2)$$

Clark (1970) also considered that the photochromic behaviour was due to a charge transfer involving iron, but thought that a different reaction took place :-

$$Fe^{3+}\square + e^{-} \longrightarrow Fe^{2+}\square \qquad (4.3)$$

where $\square$ signifies a nearest neighbour oxygen vacancy. Measurements of the bleaching rates of the radiation-induced absorption suggested that the photochromic centre is an electron trap with thermal and optical ionization energies of 0.5 and 2.5 eV respectively.

4.3.3 Nickel

Nickel occupies the octahedral interstitial site in the rutile lattice and e.s.r. spectra representing both the divalent and trivalent states have been reported (Gerritsen, 1962). Ni^{2+} is a $3d^{8}$, S = 1 ion

with a very anisotropic spectrum and a highly temperature-dependent linewidth which prevents its observation at temperatures above $\sim$ 100 K. Ni^{3+}, however, has a $3d^7$, $S = \frac{1}{2}$, electronic configuration with narrow, relatively isotropic lines which are easily detected at room temperature. Optical irradiation of nickel-doped rutile at room temperature produced a third e.s.r. spectrum which was labelled 'light-sensitive' Ni^{3+}. This spectrum had the symmetry of a centre on a substitutional site and its intensity slowly decayed again after irradiation had ceased.

4.3.4 Manganese

Manganese occupies the Ti^{4+} substitutional site in the rutile lattice and e.s.r. spectra representing both the trivalent (Gerritsen, 1963) and tetravalent (Andresen, 1960) states have been reported. Mn^{55} (100% natural abundance) has a net nuclear spin of 5/2, so that in general manganese e.s.r. spectra may be clearly distinguished by having six equally spaced resonance lines for each transition.

Mn^{4+} is isoelectronic with Cr^{3+}, having a $3d^3$ electronic configuration. The resonance lines are narrow and observable at room temperature, though at certain crystal orientations the spectrum becomes extremely complex due to the appearance of many 'non-allowed' hyperfine transitions giving rise to about forty closely spaced lines.

Mn^{3+} is a $3d^4$, $S = 2$ ion. The e.s.r. signal can only be detected at temperatures below $\sim$ 80 K, due to its rapid spin-lattice relaxation.

α-irradiation of a manganese-doped rutile crystal at 77 K (Gerritsen, 1963) caused a decrease in the Mn^{4+} intensity, and the simultaneous appearance of a new signal, which was interpreted as Mn^{2+}. This process was reversed by warming the sample to room temperature.

4.3.5 Other Dopant Ions

Cobalt occupies the substitutional site as Co^{2+} ($3d^7$, $S = \frac{1}{2}$), (Yamaka, 1962). The 7/2 nuclear spin causes each main transition to be represented by eight hyperfine absorption lines. Miyoko (1967) has

reported extra spectra in cobalt-doped crystals which were interpreted as resulting from complexes of Co^{2+} ions with nearest neighbour oxygen vacancies.

Vanadium also has a 7/2 nuclear spin and usually substitutes for Ti^{4+} as V^{4+} ($3d'$, $S = \frac{1}{2}$), (Gerritsen, 1960). The short spin-lattice relaxation time means that the absorption lines rapidly broaden as the temperature is raised above 77 K. Kubec (1972) concluded that some of the vanadium ions could be transferred from substitutional to interstitial sites by reducing the crystal in a vacuum at $900^{o}C$ and then annealing at $\sim 600^{o}C$.

Divalent copper ($3d^{9}$, $S = \frac{1}{2}$) can exist on either the substitutional (Ensign, 1969) or the interstitial (Kerssen, 1973) site in rutile. The e.s.r. spectra of copper are especially distinctive, due to the existence of the two isotopes, Cu^{63} (69%) and Cu^{65} (31%), both with nuclear spins of 3/2, but each with different nuclear magnetic moments, so that usually each main transition is split into two groups of four absorption lines, each with their characteristic hyperfine splitting constants.

Chester (1961) and Zimmerman (1973) have studied niobium-doped rutile, in which Nb^{4+} ($4d'$, $S = \frac{1}{2}$, $I = 9/2$) substitutes for Ti^{4+}. At temperatures below ~ 25 K the e.s.r. spectrum consists of ten distinct hyperfine components, but as the temperature is raised these broaden and appear to coalesce into one absorption line.

Molybdenum also occupies the substitutional site in rutile and e.s.r. spectra representing both Mo^{5+} ($4d'$, $S = \frac{1}{2}$) (Chang, 1964) and Mo^{3+} ($4d^{3}$, $S = \frac{3}{2}$), (Ohlsen, 1973) have been reported. Ohlsen deduced that molybdenum can exist as Mo^{3+}, Mo^{4+}, Mo^{5+} or Mo^{6+} in rutile and suggested that transitions between the different oxidation states could be induced by altering the Fermi level during reduction-oxidation heat treatments.

Superhyperfine interactions with neighbouring Ti^{4+} (7.7% natural

abundance) and Ti^{49} (5.5%) isotopes have been observed with several of the impurity ions mentioned above (Yamaka, 1964, Chang, 1964), the main criterion for observation being that the maximum field separation caused by the interaction is greater than the linewidth of the main e.s.r. signal.

E.s.r. spectra have also been reported from the following larger dopant ions in rutile :- W^{5+} ($5d^1$, Chang, 1966) ; Ta^{4+} ($5d^1$, Chester, 1961); Pt^{3+} ($5d^7$, Chandrashekhar, 1976); Ce^{3+} (Chester, 1961) and Gd^{3+} (Yamaka, 1963).

The data presented in this section and summarised in Table 2 shows that all of the first row transition metals can be doped into rutile and that most can exist in more than one valence state in the lattice. Charge transfer between the different states can be achieved by optically exciting transitions or by adjusting the Fermi level of the crystal. Kingsbury (1968) developed a technique for varying the Fermi level in a controlled manner which involved heavily doping the crystal with lithium. This forms a very shallow donor level and hence raises the Fermi level to just below the conduction band. Successive oxidation treatments then gradually reduce the lithium concentration and therefore lower the Fermi level, which is assumed to be at the centre of the band gap in a fully oxidised sample. This technique was later used (Mizushima, 1972) to give estimates of the relative positions which impurity ions occupy with respect to the rutile energy band structure. A single crystal was co-doped with iron, chromium, mangangese and vanadium and the intensities of the resulting e.s.r. spectra were monitored as the Fermi level was adjusted. The conclusions suggested that Fe^{3+}, Cr^{3+}, Mn^{4+} and V^{5+} levels are situated near the valence band, V^{4+} and Mn^{3+} are approximately at the centre of the band gap, V^{3+}, Mn^{2+} and Fe^{2+} are near the conduction band and the Cr^{2+} level is above the bottom of the conduction band.

4.4 NON-STOICHIOMETRIC RUTILE

When rutile is chemically reduced, by heating in a vacuum or a reducing atmosphere such as hydrogen, its colour changes to successively

darker shades of blue as the resistivity decreases to that of an n-type semiconductor. The increased conductivity is due to the creation of shallow intrinsic donor centres at energy levels just below the conduction band and the blue colour is caused by a broad free carrier absorption band centred on $\sim 1.7\mu m$ (Cronemeyer, 1952). There has been considerable uncertainty, however, concerning the exact nature of the defect structure in non-stoichiometric rutile.

In principle the defects may be either interstitial titanium ions:-

$$TiO_2 \rightarrow (1-x)\ TiO_2 + xO_2 + x\ Ti^{4+} + 4\ x\ e^- \qquad (4.4)$$

or oxygen vacancies, V_O :-

$$TiO_2 \rightarrow TiO_{2(1-x)} + x\ O_2 + 2x\ V_O^{2+} + 4\ x\ e^- \qquad (4.5)$$

Initial conclusions from electrical and optical properties (Breckenridge, 1953) favoured oxygen vacancies. Other workers supported interstitial titanium as the dominant defect, with evidence from internal friction results (Carnahau, 1963) proton beam scattering measurements (Yagi, 1977) and studies which showed that very strongly reduced rutile consisted of parallel sheets with the normal crystal structure, separated by grain boundaries with Ti in octahedral interstitial sites (Hurlen, 1959). Kofstad (1967) suggested that whether Eqn 4.4 or Eqn. 4.5 occurred on reduction depended on the reduction temperature and the oxygen partial pressure, a view which was supported by density measurements (Barbanel, 1969) and oxygen vacancy diffusion studies (Iguchi, 1972) which concluded that titanium interstitials only form at temperatures $\geq 600^{o}C$, when they become the dominant defect, though oxygen vacancies can form at much lower temperatures. Internal friction (Wachtman, 1966) and dielectric relaxation (Dominik, 1967) results have suggested that the donor centres in reduced rutile may not be simple isolated defects but rather complexes of either titanium interstitials or oxygen vacancies with one or more

trivalent substitutional impurities.

4.5 E.S.R. IN NON-STOICHIOMETRIC RUTILE

Much of the e.s.r. data gathered from reduced rutile crystals has also been the subject of considerable discussion, since the spectra are open to more ambiguous interpretation than those produced by impurity ions. A signal in hydrogen-reduced rutile (Chester, 1961), which was only detected at temperatures below $\sim$ 10 K, was assigned to interstitial Ti^{3+}, on the basis of its multiplicity and angular dependence, and was accepted as such and its detection was widely quoted in the literature as evidence of Ti^{3+}. This interpretation of the spectrum has since been disputed (Shen, 1974), however, and the signal is now thought to originate from interstitial hydrogen, which readily enters the lattice during chemical reduction, with an electron being loosely bound to it below 10 K, giving rise to the e.s.r. signal. Bogomolov (1968) observed a different e.s.r. spectrum in a sample which was reduced in hydrogen at 900^{o}C and measured at 77 K. and assigned it to an F centre. Ti^{3+} on a normal titanium site was reported by Gerritsen (1962). Another spectrum with similar g-values was produced in a rutile crystal which had been grown by an electrolytic technique and thereby heavily-doped with platinum (Chandreshekhar, 1976). This was also attributed to substitutional Ti^{3+}, with further supporting evidence coming from the observation of hyperfine interactions with Ti^{47} and Ti^{49}, with a significantly larger field splittings than those resulting from superhyperfine interactions that have been observed with other defects (Yamaka, 1964). Chester (1964) examined crystals which had been grown by a zone-refining technique and then subjected to different degrees of reduction by various methods. A large number of e.s.r. spectra, including those previously ascribed to interstitial and substitutional Ti^{3+}, were isolated. Several were only observed in crystals which had been heavily doped with aluminium and reduced in vacuo. Kerssen (1973) also investigated vacuum-reduced, Al-doped crystals and distinguished several more different

paramagnetic centres, two of which were interpreted as electrons trapped on Ti^{4+} ions near associated interstitial Al^{3+} ions.

A summary of the various e.s.r. spectra detected in reduced rutile is presented in Table 4.3, together with interpretation, where available. It appears that many of these 'intrinsic' e.s.r. spectra only appear in crystals which also contain extrinsic defects, notably aluminium. This suggests that the presence of these neighbouring impurity ions can sufficiently perturb the normal titanium (or oxygen vacancies) sites to alter their potential with respect to the lattice. The sites then become capable of trapping charge to form paramagnetic centres.

4.6 E.S.R. IN IRRADIATED RUTILE

Irradiation of rutile crystals can lead to the creation of two classes of defects which may be detected by e.s.r. First, the incidence of high energy (e.g. neutron) radiation can cause atomic rearrangements and produce new centres (e.g. interstitials and vacancies), which were not present in the unirradiated state. Lower energy (e.g. ultra-violet) radiation is usually insufficient to disturb the interatomic arrangement but can cause electronic transitions across the energy band gap. This may then lead to the filling of energy states in the band gap which are normally unoccupied in equilibrium conditions and which, by cooling to sufficiently low temperatures, may be thermally isolated from the transport bands to enable the detection of e.s.r. spectra from these post-irradiated meta-stable defect centres.

Young (1961) observed several e.s.r. signals in rutile samples which had been subject to γ-irradiation at 77 K. Two of the spectra had the symmetry of substitutional sites. It was also noticed that γ-irradiation had the effect of reducing the intensities of Fe^{3+}, Cr^{3+} and other impurity spectra. These effects could be reversed either by exposing the crystal to visible light or by annealing. Neutron irradiation of rutile (Weeks, 1961) produced

TABLE 4.3 E.S. R. Parameters of Defects in Non-Stoichiometric Rutile

g_{110}	$g_{1\bar{1}0}$	g_{001}	Remarks	Inter-pretation	Reference
g_x=1.974	g_y=1.977	g_z=1.941	x,y are 19° from <110>in (001) plane	Inter-stitial Ti^{3+}	Chester (1961) Shen (1974)
				Inter-stitial H^+	
1.965	1.965	1.935		F centre	Bogomolov(1968)
1.975	1.978	1.953		Subst. Ti^{3+}	Gerritsen(1962)
1.9777	1.9743	1.9436	seen in Pt-doped crystal	Subst. Ti^{3+}	Chandrashekhar (1976)
g_x=1.916	g_y=1.952	1.814	vacuum-reduced Al-doped	Ti^{3+}-Al^{3+} -Al^{3+}	Kerssen(1973)
g_x=1.850	g_y=1.885	1.932	"	Ti^{3+}-Ti^{3+} -Al^{3+}-Al^{3+}	"
g_x=1.962	g_y=2.040	1.709	"	"	"
1.965	1.965	1.965	"	F centre	"
g_x=1.885	g_y=1.915	1.825	"		"
1.980	1.978	1.956	Tr < 450°C	F centre trivalent impurity	Chester(1964)
1.923	1.896	1.793	Al-doped	Ti^{3+} with nearby Al	"
1.923	1.912	1.828	"		"
1.924	1.957	1.78	Reduced in H_2		"
1.985	1.989	1.932			"
1.964	1.971	1.971			"
1.964	1.994	1.928	Ti-doped		"
1.954	1.979	1.950	"		"

a new paramagnetic centre which was stable at room temperature.

Purcell (1971) made a study of paramagnetic defects in rutile which were produced by neutron reactor irradiation at 140 K and γ-irradiation at 77 K, with e.s.r. spectra recorded at 4.2 and 77 K prior to warm-up. At least four different species were isolated, all of which were annealed out by subsequent warming to room temperature. One spectrum, which was created by neutron irradiation and had substitutional site symmetry, was assigned to a singly charged oxygen vacancy. Isochronal annealing between 110 K and room temperature suggested that the oxygen ion recombines with the vacancy at temperatures above $\sim$ 233 K. This centre could not subsequently be recreated by γ-irradiation at 77 K. This sequence of treatments, however (neutron irradiation at 140 K, warm up to room temperature, followed by γ-radiation at 77 K) produced a new e.s.r. spectrum, which was interpreted as being due to the displacement, during reactor irradiation, of titanium ions to interstitial sites, where they were then able to trap electrons during γ-irradiation to give interstitial Ti^{3+} centres. This interpretation was supported by the detection of Ti^{47} and Ti^{49} hyperfine structure. The interstitial titanium ions slowly recombined if the crystal was left at room temperature. Two other weaker spectra were also tentatively assigned to Ti^{3+}, one with substitutional symmetry and the other with the symmetry of an interstitial or perturbed substitutional site. The spin-lattice relaxation times of these defects were too long to permit e.s.r. measurements at 4.2 K, due to power saturation effects.

Following u.v. irradiation of an aluminium-doped rutile crystal at 5 K (Zwingel, 1976), three separate e.s.r. spectra, all with the characteristic superhyperfine structure associated with the 5/2 aluminium nuclear spin, were identified as being due to holes trapped on one of the oxygen ions surrounding a substitutional Al^{3+} ion, with some having a second Al^{3+} ion in an adjacent unit cell. The single Al centres were thermally emptied after heating to 40 K. The double Al centres apparently

formed deeper traps, which were filled during the thermal emptying of the single Al centres and which were in turn emptied by heating to ∿ 55 K. Furthermore, it was noted that u.v. irradiation at 5 K caused both the disappearance of Fe^{3+} and Cr^{3+} e.s.r. lines and the creation of four new, unidentified lines. These photo-induced changes could all be reversed by heating the crystal to temperatures above 180 K. Table 4 summarises the e.s.r. spectra detected in irradiated rutile.

4.7 TRAPPING LEVELS IN RUTILE

Single crystals of rutile invariably contain relatively large concentrations of defect centres, with energy levels in the forbidden band gap, which are able to trap charge carriers. Their existence is mainly due to the comparatively crude crystal growth techniques which have to be employed, as a consequence of the high melting point of rutile. A desire to understand and characterise the trapping properties of these centres in rutile has led to a considerable amount of investigations by such techniques as thermally stimulated conductivity (TSC) and thermo-luminescence (T.L.). Basically these technqiues involve cooling the crystal to a cryogenic temperature, usually 77K, irradiating with ultra-violet (i.e. with radiation of energy greater than the band gap of ∿ 3.0 eV), thereby filling the traps with charge, then raising the temperature at a constant heating rate while measuring the conductivity (TSC) or luminescent emission (T.L.). As each set of traps is thermally reconnected with the transport bands, peaks in the luminescence and conductivity are detected as excess charge is freed and then recombines via the luminescence centres. Detailed analysis of the curves of current or luminescent intensity vs time can then lead to estimates of the traps' density, their capture-cross-section and their ionization energy, though such calculations involve several assumptions and require a knowledge of the trapping kinetics.

TABLE 4.4 E.S.R. Parameters of Defects created by Irradiation of Rutile

g_{110}	$g_{1\bar{1}0}$	g_{001}	Irradiation Conditions	Inter-pretation	Reference
1.92	1.89	1.80	γ-rays at 77 K		Young (1961)
2.00	4.50	3.43	"		"
1.964	1.914	1.935	"		"
1.935	1.985	1.989	neutrons at room temp.		Weeks (1961)
1.969	1.983	1.988	neutrons at 140 K	F centre	Purcell (1971)
1.991	1.9503	1.9503	"	Ti^{3+}	"
1.998	1.973	1.971	"	Ti^{3+}	"
1.966	1.980	1.987	neutrons at 140 K + anneal + γ at 77 K	Ti^{3+} inter-stitial	"
g_x=2.0192	g_y=2.0261	g_z=2.0034	U.V. at 10 K	Trapped hole near Al^{3+}	Zwingel (1976)
g_x=2.0197	g_y=2.0189	g_z=2.0030	U.V. at 10 K + anneal	Trapped hole near Al^{3+}	"

These techniques were first used to study rutile by Addis (1968), who detected the same eight shallow traps in 'pure' rutile crystals, by both T.S.C. and T.L. from a luminescence band at $\sim$ 850 nm. The peak temperatures of the glow curves (derived with a heating rate of 30^{o} per minute) are presented in Table 5, together with their trap depths which were calculated by Fermi analysis (Bube, 1960), with the assumption that fast-retrapping (bimolecular) kinetics prevailed.

It was concluded that they were all indicative of electron traps. Further measurements (Ghosh,1969), involving infra-red bleaching of T.L. curves, gave estimates of optical ionization energies which were generally $\sim$ x 2.5 greater than the thermally-generated values.

The presence of levels deeper into the band gap was inferred from photoconductivity and photoluminescence spectra and also from the fact that T.S.C. and T.L. curves could be generated, though with lower intensities, using radiation of wavelength greater than 0.4 μ. The wavelength at which thermoluminescence could no longer be generated ($\sim$ 0.6-0.7 μ) was interpreted as an indication of the optical ionization energy of the luminescence centre. No firm conclusions could be made with regard to the identity of the trapping centres, however, though it was speculated that the luminescence centre and the trap with a T.L. peak at 169 K may be due to interstitial Ti^{3+} and oxygen vacancies respectively. Increased resolution of the emission band at 850 nm by measurements made at 4.2 K in pure and chromium-doped crystals (Grabnev, 1970), have since suggested that the luminescence centre is substitutional Cr^{3+}.

Recent work performed in this department (Hillhouse, 1978) involved the detection of T.S.C., T.L. and photoconductivity spectra in order to compare the distribution of defect centres in commercial Verneuil -grown crystals and those grown by the plasma torch technique. The same trapping levels were found in both sets of crystals, though the trap densities

appeared to be considerably lower in the plasma-grown, stoichiometric samples. The trapping parameters were calculated by a variety of analysis methods and the main data is summarized in Table 4.5. The discrepancy between these trap depth estimates and those derived by Addis et al was explained by the initial assumption of fast-retrapping kinetics being inappropriate, a conclusion which was supported by a method of analysis used to predict the order of kinetics (Chen, 1969) which suggested that the recombination mechanism was in fact intermediate between the two extremes of monomolecular and bimolecular kinetics. The effect of reduction in vacuum on trap density was also studied, with the conclusion being reached that the concentrations of the three shallowest traps were increased as the conductivity of the sample was raised by reduction. The high temperature peaks of the T.S.C. curves were swamped by increased dark current in the reduced crystals. Again, no conclusions regarding the identities of the traps were made, though studies of crystals doped with various transition metal ions failed to directly associate chemical impurities with any of the trapping centres.

TABLE 4.5 T.S.C. data of defects in rutile, comparing peak temperatures (T_p) and estimated trap depths (E_t) derived by Addis (1968) and Hillhouse (1978).

Addis		Hillhouse	
T_p (K)	E_t (eV)	T_p (K)	E_t (eV)
91	0.27	92	-
106	0.28	104	0.13
121	0.32	121	0.24
169	0.48	176	0.37
200	0.56	-	-
241	0.62	245	0.51
296	0.76	300	0.61
334	0.87	330	0.69

CHAPTER 5

EXPERIMENTAL APPARATUS AND TECHNIQUES

5.1 APPARATUS

5.1.1. E.S.R. Spectrometer

Most of the e.s.r.measurements were made with a Varian V-4502-15 X-band spectrometer, a block diagram of which is presented in Fig 5.1. The following section is intended to summarize the basic features of the spectrometer, though more detailed information may be found in the books by C.P. Poole (1967).and Wilmshurst (1967).

The microwave source is an X-band klystron valve which can be tuned to adjust the output frequency over a range of $\sim$ 9.5 $\pm$ 0.5 GHz. The klystron is coupled to a waveguide which transfers the microwave output,via an isolator and a variable attenuator, to the 1st arm of a microwave bridge or magic Tee. This is a device which will not permit power to pass directly into the opposite arm. Thus the incoming source power is equally divided between the two adjacent arms, 2 and 3. Arm 2 is terminated by a matched load and arm 3 is terminated in a microwave cavity which is located in the magnet gap. Power will only enter the fourth arm of the bridge if either arm 2 or arm 3 reflects some of the incident power from arm 1.

The cavity consists of a resonant section of waveguide in which the microwave power builds up standing waves of high electric and magnetic fields and the sample is placed in a region of maximum r.f. magnetic field. This spectrometer uses a V- 4531 cavity, operating in the E_{102} mode, so that the sample is located in the cavity centre. Spaces at the top and bottom of the cavity permit the insertion of quartzwave for variable temperature measurements and slots in the front face allow direct irradiation of samples while still in the cavity.

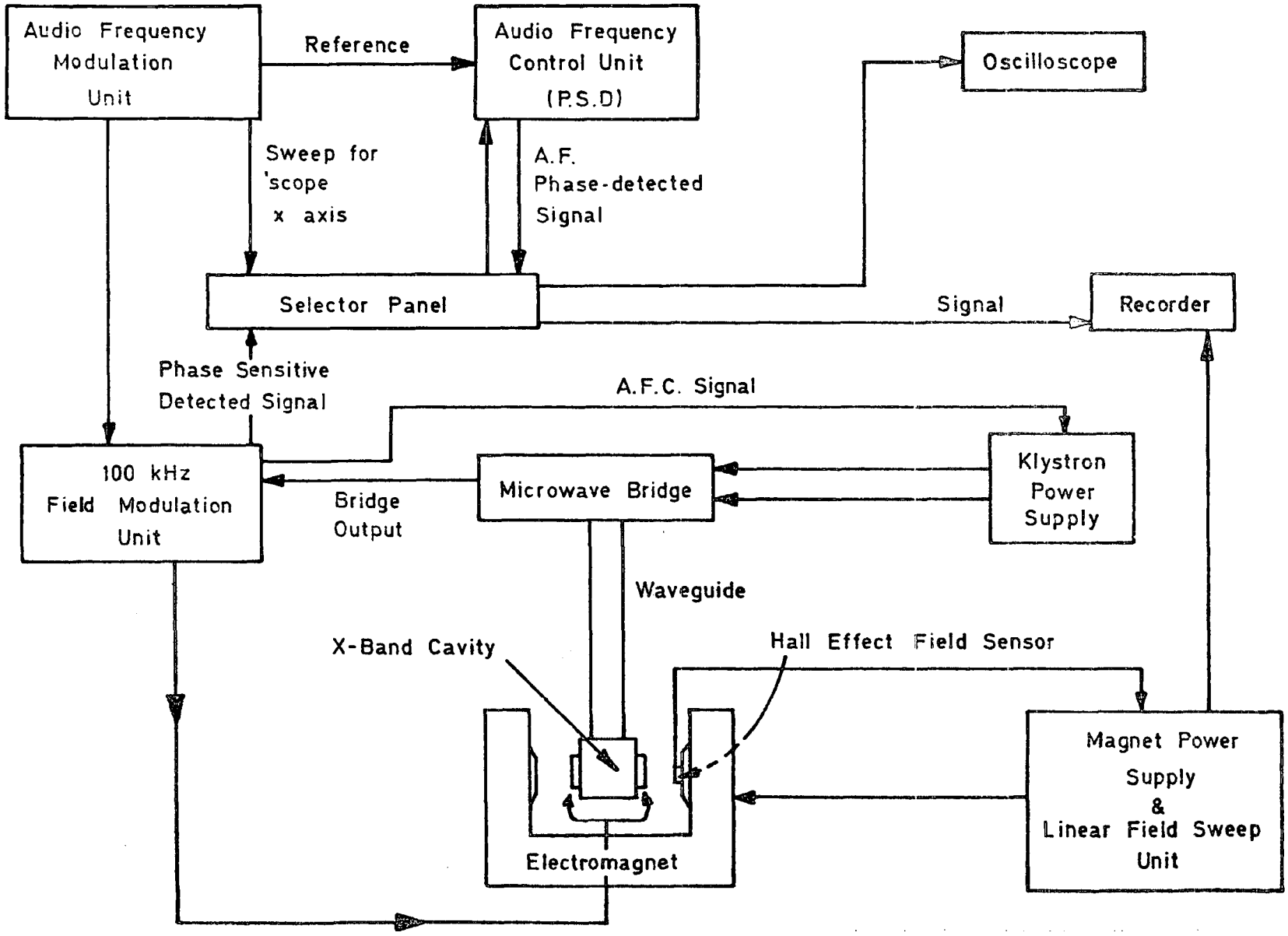

FIG. 5.1 BLOCK DIAGRAM OF E.S.R. SPECTROMETER

The klystron frequency has to be adjusted to the resonant frequency of the cavity. This frequency is determined by applying a sawtooth signal to the klystron reflector voltage. The resulting variation of power entering the fourth arm of the microwave bridge is detected by a diode and displayed as an oscilloscope trace in which the cavity resonant frequency is indicated by a dip corresponding to absorption of power. The sawtooth signal is removed and the klystron frequency is centred on to the value giving minimum output power by adjusting the D.C. reflector voltage. The klystron frequency is then locked to the resonant cavity frequency by an Automatic Frequency Control (A.F.C.) system. Basically this involves a low amplitude 10 kHz modulation being applied to the klystron reflector voltage with consequent modulations in frequency and detected output power. The output signal is fed, via a lock-in amplifier, to a phase-sensitive-detector, together with a reference signal from the 10 kHz oscillator. When the klystron frequency is exactly the same as the central cavity resonant frequency a 20 kHz modulation of power output is detected, but when the frequency deviates from the central value a 10 kHz component is detected and fed to the phase-sensitive-detector, which then applies a D.C. error voltage of appropriate polarity to the klystron to correct the frequency deviation.

In the off-resonance condition the coupling of the cavity is adjusted, by means of a nylon coupling screw, until the impedance of the cavity matches that of the waveguide and no power is reflected back to be detected in the fourth arm of the microwave bridge. In order to bias the detector crystal, however, some power is then reflected from the balancing arm (2) by adjusting a slide-screw tuner.

The external D.C. magnetic field is slowly swept by varying the current through the magnet coils. A linear sweep of field with respect to time and long term magnetic field stability is ensured by the use of a Hall effect field sensor attached to one of the magnet pole faces. A reference voltage, which is proportional to the required field, is compared

to the output Hall voltage,which is proportional to the actual field. If the two voltages are not equal an error signal is generated which causes the magnet current to be adjusted until the required field is reached.

Absorption of power by the sample as the field sweeps through the magnetic resonance condition changes the impedance of the cavity, causing power to be reflected back to the magic Tee and a resulting change of power to be detected. Since the amount of noise generated at the detector crystal is inversely proportional to frequency a high frequency modulation of the e.s.r. signal is introduced to increase the signal-to-noise ratio. A 100 kHz sinusoidal voltage is applied to a pair of modulation coils which are built into the walls of the cavity, so that the sample experiences both the large D.C. magnetic field together with the low amplitude (typically 0.1 to 1 Gauss) 100 kHz modulation field. When the D.C. magnetic field is slowly swept through a resonance line a 100 kHz modulation of the power absorption is also detected, the phase and magnitude of which are determined by the slope of the resonance absorption line. Hence, by using a lock-in amplifier and phase sensitive detector with a reference signal from the 100 kHz oscillator, a D.C. output, which approximates to a 1st derivative of the absorption line, is produced and displayed by a chart recorder. To give a true derivative the modulation amplitude should be significantly less than the linewidth of the absorption signal. Increasing the modulation amplitude increases the signal-to-noise ratio but may also lead to modulation line broadening. The signal-to-noise ratio may also be increased by raising the microwave power level, provided that this does not result in power saturation.

This spectrometer also has facilities for audio frequency modulation of the magnetic field, which is usually used in conjunction with a V4532-dual sample cavity for spin calibration measurements. This cavity operates in the E_{104} mode to give three regions of maximum r.f. magnetic field. The

sample to be measured is placed in one such region and a standard sample of known spin density is placed in another. Each sample is then subjected to magnetic field modulations of different frequency, so that e.s.r. signals from the two samples may be produced simultaneously but detected and displayed separately. This method is especially convenient in situations where both samples give rise to resonance signals in the same magnetic field region, which would otherwise be superimposed. The audio frequency modulation unit may also be used to obtain a 2nd derivative of an absorption line.

Samples are introduced to their location for e.s.r. measurements via 11mm diameter cylindrical spaces at the top and bottom of the cavity. For room temperature studies single crystals are placed on a PTFE rod which is inserted through the base of the cavity. Angular variation measurements in the horizontal plane are performed by rotating the rod, which is attached at its base to a pointer moving over a circular scale. Powder samples are placed in 3mm bore quartz tubes and are held in place at the cavity centre by a collet and O-ring assembly above the cavity.

5.1.2 Cryogenic Facilities

Initial low temperature measurements were made with a nitrogen gas V557 cryostat in which the gas passed through a 6mm bore quartz cavity insert containing the sample. Temperatures above that of the ambient, up to $\sim$ 450K , were attained by applying a voltage to a 20 Ω heater located in the path of the gas below the cavity. Lower temperatures, down to $\sim$ 110K,were achieved by first passing the nitrogen gas through a copper heat exchanger immersed in a dewar of liquid nitrogen, the sample temperature being controlled by a combination of gas flow rate and heater voltage adjustments. The temperature was measured with a pre-calibrated resistance thermometer, which was situated between the heater and the sample.

A significant drawback with this system was that during prolonged operation at low temperatures the whole cavity tended to ice-up, since it was not thermally insulated from the coolant gas which was exhausted into the atmosphere above the cavity. This meant that on reheating the sample the ice melted and the resulting water damped the cavity, thus hindering the use of temperature cycling techniques. To a certain extent, however, the N_2 gas cryostat complemented the liquid helium cryostat described below in that the former allowed measurements to be made above room temperature.

Most of the e.s.r. measurements reported in this work were made with the aid of a liquid helium continuous flow cryostat, supplied by Oxford Instruments, incorporating automatic temperature control between 3 K and 300K. The cryostat basically consists of a stainless steel capillary tube to direct the helium from an arm connected to a transfer tube to another arm comprising a quartz dewar assembly which passes through the cavity. The whole path of the helium in the cryostat is isolated from the ambient and is surrounded by a vacuum jacket. Liquid helium is continuously pumped from a storage vessel to the cryostat via a flexible transfer tube, which also consists of two concentric stainless steel tubes surrounded by a vacuum jacket. The coolant then flows through the capillary in the cryostat and emerges just below the cavity to strike a 3mm bore quartz tube containing the sample. This sample tube is introduced into the cavity and held in place by a gas-tight O-ring seal at the top of the quartz dewar cavity insert. For single crystal studies a gear-operated goniometer is used as a top fitting on the quartz insert to give control over the crystal orientation in the horizontal plane to $\pm$ 0.5^{o}. After striking the sample tube the coolant is pumped back through the cryostat transfer tube, hence helping to keep the incoming liquid cool. The exhaust gas then travels via a needle valve and flowmeter to a diaphragm pump and thence to a recovery system. The pressure in the cryostat vacuum space is maintained at

$\sim 6 \times 10^{-5}$ torr by a water-cooled oil vapour diffusion pump, backed by a single-stage rotary pump. When operating below $\sim$ 60K the valve connecting the vacuum pump to the cryostat is closed, thus allowing the pressure to be further reduced by cryo-pumping as the residual gases are condensed.

Coarse temperature control is achieved by adjusting the helium flow rate with needle valves. Fine adjustments and automatic temperature control is realised with a heater wound onto a copper heat exchanger which surrounds the tip of the capillary tube. The temperature is measured by a gold/iron-chromel thermocouple which is located in the path of the helium between the capillary and the sample tube.

5.1.3 Irradiation Facilities

A Philips 90 Watt Hg lamp provided a source of ultra-violet radiation with, when necessary, a $CuSO_4$ solution filter to absorb the infra-red component of the lamp's output. A 250 Watt Tungsten Lamp, together with a silicon filter, was used as an infra-red source. For the irradiation of samples in situ the relevant lamp and filter were arranged on a bench with a lens to focus the beam onto the optical window of the cavity. Figure 5.2 shows the spectrometer in operation during u.v. irradiation of the sample at 40K.

5.2 TECHNIQUES

5.2.1 Identification

Having initially detected an e.s.r. signal the next stage is to identify the spectrum and the species responsible for it. This involves an experimental determination of the spin Hamiltonian parameters which describe the spectrum and is achieved by measuring the variation of resonance field as the orientation of the crystal with respect to the magnetic field is varied at a constant frequency, a technique known as isofrequency plotting. It is therefore necessary to measure both the magnetic field and the microwave frequency with the greatest possible accuracy. The

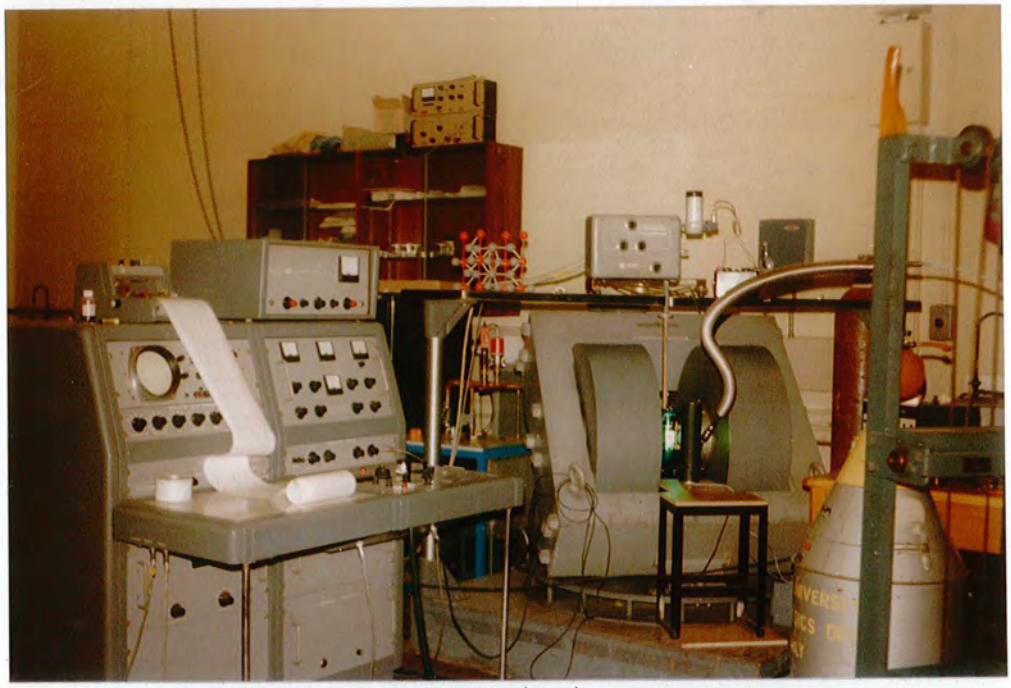

Figure 5.2 : Photographs of the E.S.R. spectrometer, taken during u.v. irradiation of a sample at 40 K.

magnetic field was measured with a Newport Instruments N.M.R. Magnetometer. The probe was placed adjacent to the cavity in the magnet gap and the frequency of the proton resonance signal was measured with a Malden Electronics frequency meter. The microwave frequency was measured with a Hewlett Packard X532B frequency meter. Field calibrations using diphenyl-picryl-hydrazyl (D.P.P.H, g = 2.0036) showed that reproducible g-value determinations could be made to within ± 0.0005.

5.2.2 Absolute Spin Calibration

Spin concentration measurements were carried out by comparing the total integrated intensity of an e.s.r. signal with that of a reference signal from a sample of known spin density, e.g. single crystals of freshly grown $CuSO_4.5H_2O$ or polycrystalline D.P.P.H., both of which contain one unpaired electron per molecule. The unknown sample and reference sample are placed in the two halves of the dual sample cavity and are subjected to 100 kHz and 400 Hz magnetic field modulation respectively during recording of their spectra. The positions of the two samples are then interchanged and the spectra are re-recorded, thus eliminating the different sensitivities and gains of the A.F. and 100 kHz detection systems from the calculation, so that the 1st moments of the derivative signals may then be directly compared. Under ideal conditions, when the unknown and reference signals have similar linewidths and intensities, spin concentration estimates can be accurate to within ± 20%. In practice, however, this rarely occurs and most of the spin density results reported in this work are only accurate to within a factor of two.

5.2.3 Relative Spin Calibration

Changes in spin density with respect to their own initial values can be measured with much greater accuracy than absolute spin calibrations, the experimental error being as low as ± 1% for spectra with a high signal-to-noise ratio. Provided that the signal linewidth remains constant as

the intensity changes, which is generally the case with dilute paramagnetic species at a constant temperature, then it is unnecessary to integrate the recorded (derivative) signal. The peak-to-peak amplitude of this signal gives an accurate measure of the relative concentration of the defect which is responsible for the resonance line, since the intensity of an absorption signal approximates to $K\ I\ H^2$, where K is a constant which depends on the lineshape, and I and H are the peak-to-peak amplitude and peak field separation respectively of the recorded 1st derivative signal.

5.2.4 Detection of Charge Transfer by Isochronal Annealing

Isochronal annealing is a technique in which relative changes in e.s.r. signal amplitudes are measured in order to determine the temperatures at which charge transfer reactions, initially caused by incident radiation (e.g. the filling of trapping centres with charge) are reversed by thermal energy ('ionization' of trapped charge). Basically the technique involves initially recording the spectra of interest, both before and after u.v. irradiation at a base reference temperature, then heating the sample to an anneal temperature for a set time, typically 5-10 minutes, before recooling to the reference temperature and re-recording the spectra. This cycle is repeated at successively higher anneal temperatures until the spectra have regained their pre-irradiation (as-cooled in the dark) intensities. By taking all measurements at the same temperature, and hence ensuring that spectrometer sensitivity and linewidth are unchanged, a plot of signal amplitude against anneal temperature gives a temperature profile of the defect concentration, with features corresponding to charge transfer. It is often of value to compare the information gained from isochronal annealing with data derived from similar techniques such as thermally stimulated conductivity and thermoluminescence.

Further useful information can be gained by measuring the relative rates at which charge transfer reactions, whether thermally or optically induced, proceed and this can be done by continuously sweeping through the

resonance line during and after irradiation at temperatures of interest. Great care must be taken when dealing with narrow resonance lines, that the rate of magnetic field sweep is not so great that the detection system and recorder are unable to fully respond to the signal. A study of the variation of charge transfer reaction rates with temperature may then lead to the determination of associated trapping parameters.

5.3 SAMPLE PREPARATION

All the rutile crystals studied in this work, whether bought in or grown by the plasma torch technique described in Chapter 2, were initially received as cylindrical boules, typically 1-2 cm in diameter and between 1 and 5 cm in length. The Verneuil-grown boules were delivered in a re-oxidised state and were either colourless or a pale straw colour. Some of the plasma grown boules were dark blue, indicating a heavily-reduced state and necessitating an oxidising treatment. This was done by placing the boule on a quartz boat inside a metre long 0.5" bore quartz tube which passed through a horizontal furnace. Oxygen was then passed along the tube via Edwards 0.5" couplings, the flow rate being controlled by a needle valve and monitored with a glycerol bubbler, and the temperature was raised to $1000^{\circ}C$ for 24 hrs by a Eurotherm temperature controller with a Pt/Pt Rh thermocouple. The boule was annealed by being left in the furnace as it cooled at a rate of $\sim 200^{\circ}$ perhour.

In order to produce samples of a suitable size for e.s.r. measurements, the oxidized boules were mounted on a Logitech goniometer with Durafix adhesive and aligned by back reflection Laue photography to within $\pm 0.5^{\circ}$ of the <001> crystal axis, using a Philips X-ray machine. Fig. 5.3 shows some Laue X-ray photographs taken with the beam parallel to (a) the <001> axis and (b) the <100> axis, and demonstrates the overall fourfold symmetry along the <001>, in contrast to the twofold symmetry of the <100> and <110> type axes. After aligning, the boules were then cut into 2 mm thick

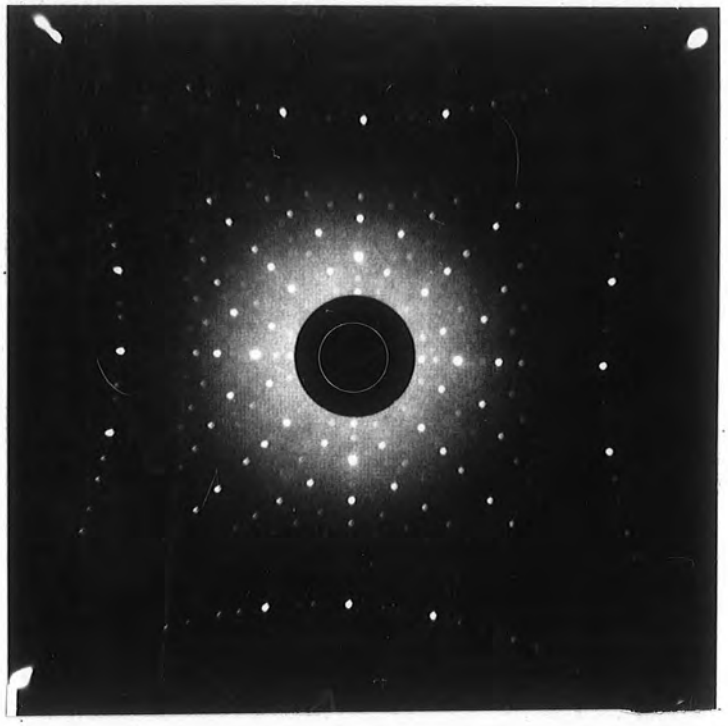

(a)

(b)

Figure 5.3 : X-ray back-reflection photographs of rutile crystals ; (a) <001> axis, (b) <100> axis.

slices by the diamond wheel of a Meyer and Burger T.S.3 slicing machine. The slices were remounted and aligned along the <110> axis to be cut into $8mm^3$ cubes for use with the liquid helium cryostat, though larger samples were used for room temperatures studies. The cubes had the same principal axes as the magnetic axes of the substitutional lattice site i.e. <110> , <$1\bar{1}0$> and <001> , in order to allow rotation of the sample in the (001) and (110) planes. In most cases the as-cut faces of the samples were sufficiently smooth and transparent to permit direct optical irradiation of the bulk of the crystal. Samples with a rough surface finish were polished with diamond paste.

5.4 DOPING TECHNIQUES

Two approaches were adopted to introduce dopant ions into the rutile lattice. The first technique involved the evaporation of a thin film of the dopant metal onto a pre-polished (001) face of the rutile sample, followed by diffusion at 1000-1150^{o}C for 24 hrs in an oxygen atmosphere. Due to the open channel structure along the <001> axis of rutile this treatment was sufficient to allow most ions to diffuse rapidly and evenly into the bulk of the sample. Using this technique, crystals were doped with :- iron, by evaporating powder from a Molybdenum boat ; manganese, evaporated from Mn flakes in a helical basket tungsten filament ; chromium, from Cr-plated tungsten filaments ; and aluminium, from pre-coated filaments. The rutile crystals were cleaned in concentrated nitric acid both before evaporation and again after diffusion to remove any unwanted or surplus metal.

The other doping technique consisted of sealing the crystal together with some of the dopant metal in a quartz tube at a pressure of 10^{-5} torr and then heating to $\sim$ 1100^{o}C for 24 hrs, during which some of the metal vaporized and diffused into the crystal. Since this treatment also led to the chemical reduction of rutile, a 2nd heat treatment in oxygen was needed to restore full stoichiometry. This method was used to dope samples with nickel, manganese, chromium,copper and cobalt. The Cr-doped crystals

were badly cracked, suggesting that the lattice was unable to accommodate all the available dopant. Attempts to dope rutile with a rare earth ion, terbium, by this technique were apparently unsuccessful, due either to the Tb vapour pressure being too low at 1150^{o}C or the Tb ionic radius being too great to permit rapid diffusion along the <001> axis.

In addition to the introduction of extrinsic defects described above other heat treatments were employed with the aim of introducing intrinsic defects into the lattice. Some samples were reduced by heating to 600^{o} C in a vacuum. In other cases, high temperature defects were frozen in by quenching crystals from 1000^{o}C instead of allowing them to anneal in the cooling furnace. This was achieved by rapidly pulling the whole quartz tube,containing the boat and sample, out of the furnace and directing a jet of compressed air onto the sample so that its temperature dropped in a few seconds to a level at which diffusion was negligible.

CHAPTER 6

SINGLE CRYSTAL RESULTS

6.1 INTRODUCTION

As a precursor to the subsequent study by e.s.r. methods of the formation and behaviour of trapping centres in doped rutile, an extensive examination was made, using a Varian 9 GHz spectrometer, of the e.s.r. characteristics of each specimen. Single crystal boules from several sources, i.e. American, Japanese, Swiss and British, were employed as the starting materials. Some of these crystals were later used (in the trapping centre studies) in their 'as-received' state while others were utilised for further doping experiments in order to maximise the concentration of specific dopants. A summary of the origin and subsequent preparative treatment of each specimen is given in Table 6.1.

Most of the paramagnetic defects responsible for e.s.r. spectra in the 'as-received' crystals studied in this work were identified as extrinsic impurities by a comparison of the spectral angular dependence and resulting Spin Hamiltonian parameters with those quoted in the literature for various dopant ions in the rutile lattice. The latter information has been summarized in Chapter 4. Every boule examined contained a comparatively large concentration of substitutional Fe^{3+}, which invariably gave rise to the most intense e.s.r. signals. The strong anisotropy of the Fe^{3+} spectrum proved to be a valuable aid in aligning crystals in the spectrometer cavity with respect to the magnetic field and allowed orientation to $\pm$ 0.5° within the plane of crystal rotation. It was noticeable that the crystals which had been grown under carefully controlled conditions by the plasma-torch technique contained, generally speaking, fewer paramagnetic impurities than the American, Swiss or Japanese boules, all of which were understood to have been grown by the Verneuil method.

Sample No.	Growth Method and Origin	Subsequent treatment	Comments
1	Plasma torch (TIL)	-	Doped during growth with 1000 ppm AL, grown in oxidized state - B.S.16.
2	Plasma torch (TIL)	Oxidized -24 hrs at 1000°C in O_2	Nominally undoped, grown in reduced state - B.S.10
3	Verneuil (National Lead)	-	Doped during growth with 1000 ppm Al.
4	Verneuil (National Lead)	Doped with Ni by vacuum diffusion	Cut from the same boule as sample 3, Mn also introduced during doping
5	Verneuil (Nakazumi)	Doped with Al by evaporation and diffusion	Contained several low angle grain boundaries
6	Verneuil (Swiss)	-	Aluminium-doped during growth
7	Verneuil (Swiss)	Reduced in vacuum at 600°C	Doped during growth with ∿ 5000 ppm Fe.

TABLE 6.1: Summary of origin and preparative treatment of E.S.R. specimens

6.2 CHARACTERISATION DETAILS

6.2.1 Stoichiometric Al-doped TiO_2 (B.S.16) - Sample 1

The Fe^{3+} spectrum was the only e.s.r. signal obtained from the Al-doped stoichiometric boule (B.S.16).

6.2.2 Nominally Pure TiO_2 (B.S.10) - Sample 2

This crystal, which was prepared from nominally pure starting materials, was chemically reduced during growth and subsequently reoxidized and gave e.s.r. spectra associated with both iron (as Fe^{3+}) and copper (as substitutional Cu^{2+}).

6.2.3 National Lead (1000 ppm Al) TiO_2 - Sample 3

(a) The boule which was purchased from the National Lead Company, nominally doped with 1000 ppm Aluminium, gave spectra attributed to Fe^{3+}, Cr^{3+} and interstitial Ni^{3+}, together with a much weaker signal which could not be matched to any data in the literature.

The spectrum of this centre (labelled I) was extremely complex, consisting up to 20 absorption lines at some orientations. Isofrequency plotting in the (001) (Fig.6.1), and (110) (Fig.6.2) planes, however, showed that several of the absorptions formed groups of four approximately equally-spaced lines, indicative of a hyperfine interaction with a nearby ion of nuclear spin I = 3/2. The spectrum is further complicated by the fact that (a) at several orientations each individual transition is further split into two closely-spaced lines, and (b) with the magnetic field parallel to the < 001 > axis the spectrum does not resolve into the four hyperfine lines of a single transition, as would be expected from theory. This suggests that either there are two slightly different impurity centres or, more likely, that the crystal was not initially aligned accurately enough, so that the isofrequency plots were not in fact quite in the (001) and (110) planes.

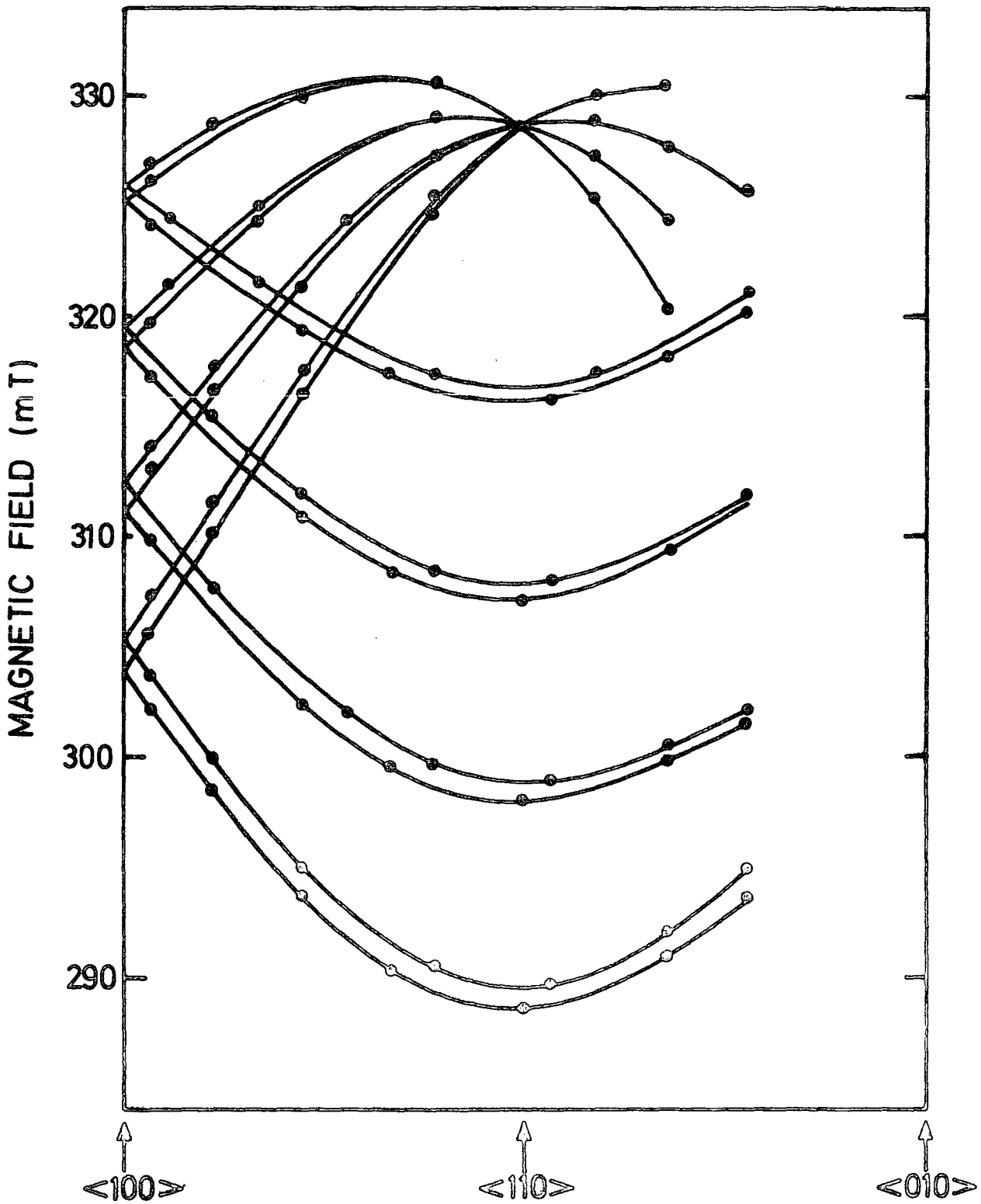

FIG. 6·1 ISOFREQUENCY DIAGRAM OF SPECTRUM I IN THE (001) PLANE. (V = 9·515 GHz ; NATIONAL LEAD UNDOPED).

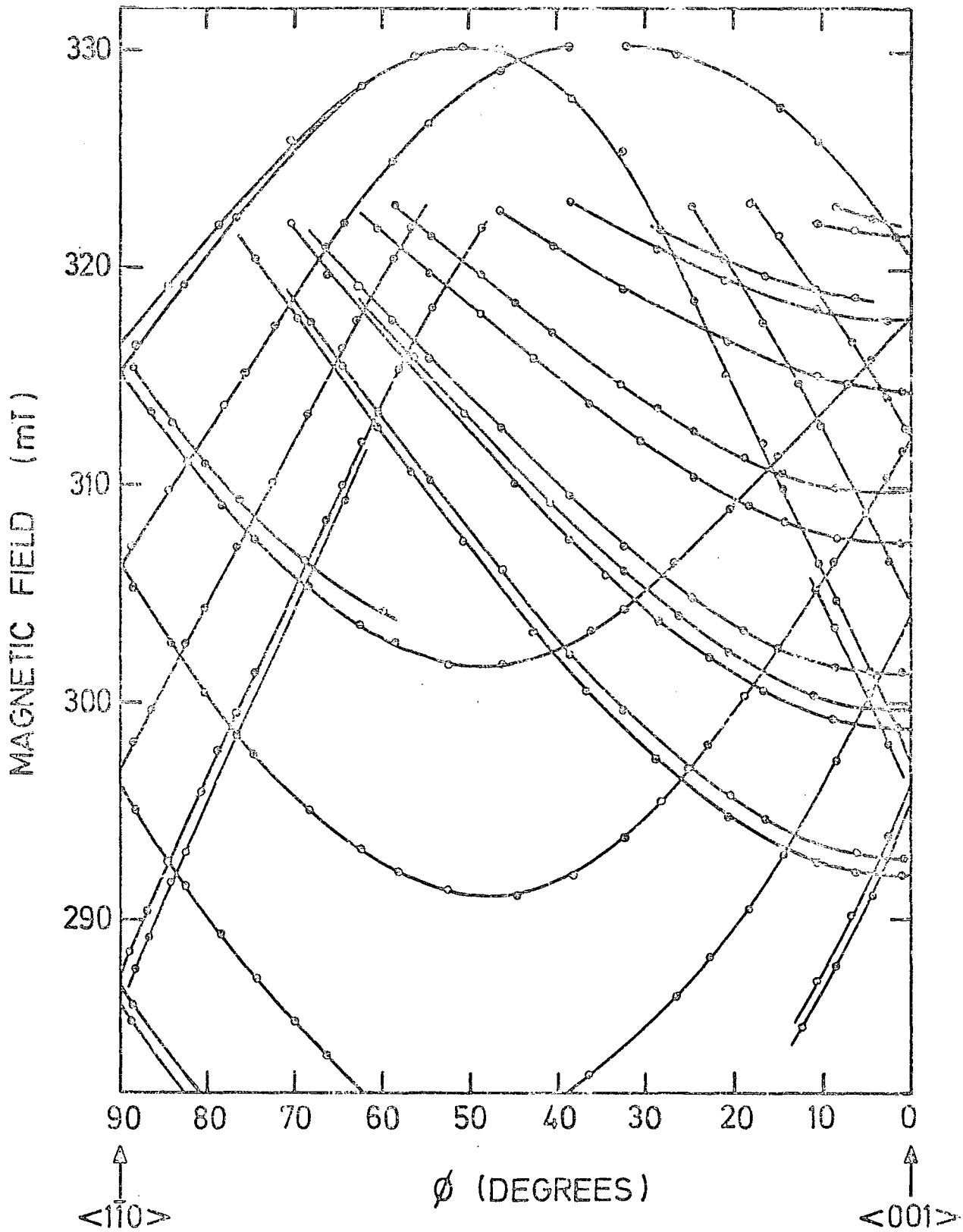

FIG. 6·2 ISOFREQUENCY DIAGRAM OF SPECTRUM I IN (110) PLANE. (V = 9 474 GHz, NATIONAL LEAD UNDOPED).

If the isofrequency diagrams are simplified by plotting the centre-of-gravity of each group of four hyperfine lines, it becomes clear that this centre does not have the simple symmetry of either the substitutional or octahedral interstitial sites. The principal magnetic axes of centre I appear to be (1) $+ 50^{\circ}$ from the 001 axis in the (110) plane, (2) -40° from the 001 axis in the (110) plane, and (3) the 110 axis, with corresponding Spin Hamiltonian parameters of :-

$$g_1 \sim 2.372, \qquad g_2 \sim 2.065, \qquad g_3 \sim 2.069$$

$$A_1 \sim 3.6 \times 10^{-2}\ cm^{-1}, \quad A_2 \sim 4 \times 10^{-3}\ cm^{-1}, \quad A_3 \sim 0$$

The g-values being greater than that of the free electron (2.0023) suggest that I is a hole centre. Reference to the crystal structure (see Fig.4.2) shows that the magnetic axes of centre I are similar to the bond directions of O^{2-} ions. A tentative model for this centre is of a hole trapped at an oxygen ion, e.g. at (x,x,0), stabilised by an impurity ion with a nuclear spin of I = 3/2 on an adjacent titanium site, e.g. at $(\frac{1}{2}, \frac{1}{2}, \frac{1}{2})$.

(b) A sample (4) from this National Lead boule was doped with nickel using a vacuum encapsulation technique. Analysis of the resulting e.s.r. spectra showed that there was only a moderate increase in the interstitial Ni^{3+} concentration but that the interstitial Ni^{2+} spectrum had now appeared, indicating that most of the additional nickel was entering the lattice in a divalent state. Furthermore, the distinctive spectra of both Mn^{3+} and Mn^{4+} appeared, following nickel doping. The manganese may have originated as an impurity in the nickel which was used for doping. The identification of several other weak resonance lines in this sample was not possible since they were superimposed with the many Mn^{4+} non-allowed hyperfine transitions, though it is probable that some, if not all, of these extra lines belong to centre I. Because the nickel-doped crystal contained such a large number of different impurities, this specimen (4) was the most extensively studied in the subsequent trapping centre measurements.

6.2.4 Japanese, TiO_2 - Sample 5

A crystal from the Japanese (Nakazumi) boule was doped with aluminium by the evaporation and diffusion technique and exhibited interstitial Ni^{3+} and substitutional Fe^{3+} e.s.r. spectra, together with evidence of low-angle grain boundaries; the latter feature rendered this crystal less suitable for detailed examination than some of the others, since some of the e.s.r. lines in an already complex spectrum were doubled.

6.2.5 Swiss, TiO_2

Of the two Swiss single crystal boules, one (sample 6) was nominally pure and only produced an Fe^{3+} e.s.r. spectrum. The other (sample 7) was doped during growth with 5000 ppm iron and was consequently a deep red colour. The e.s.r. spectra of the Fe-doped boule were very complex, though isofrequency plotting enabled the most intense lines to be assigned to substitutional Fe^{3+} and an adjacent interstitial proton c.f. Anderson (1973), while other lines had a similar angular dependence to some which Anderson tentatively assigned to a Fe^{3+} - interstitial Ti^{4+} complex. The effect of reducing this crystal by heating to 600^{o} C at a pressure of 10^{-5} torr for two hours was to reduce slightly the Fe^{3+} and Fe^{3+}-H^{+} concentrations (presumably by converting some Fe^{3+} to Fe^{2+}), but to decrease greatly the intensities of the other spectra. Re-oxidation had little effect on the intensity of the main Fe^{3+} spectrum but caused a decrease of the Fe^{3+}-H^{+} and Fe^{3+}-Ti^{4+} concentration and also the appearance of a spectrum attributed to the association of a substitutional Fe^{3+} ion and a nearest neighbour oxygen vacancy.

The impurities present in each crystal examined, as detected by e.s.r. measurements, are presented in Table 6.[2] together with their approximate concentrations, derived from spin calibrations with D.P.P.H.

Sample No.	Impurity Ion	Concentration (p.p.m)
1	Fe^{3+}	-
2	Fe^{3+}	$\sim$ 7
	Cu^{2+}	-
3	Fe^{3+}	$\sim$ 20
	Cr^{3+}	$\sim$ 1
	Ni^{3+}	$\sim$ 3
4	Fe^{3+}	$\sim$ 40
	Cr^{3+}	$\sim$ 4
	Ni^{3+}	$\sim$ 6
	Mn^{4+}	$\sim$ 2
5	Fe^{3+}	-
	Ni^{3+}	-
6	Fe^{3+}	$\sim$ 4
7	Fe^{3+}	$\sim$ 7000

TABLE 6.2 : Summary of the identity and concentrations (as estimated from spin calibrations with D.P.P.H) of impurities giving e.s.r. spectra in rutile single crystal specimens.

6.3 OPTICALLY INDUCED E.S.R. SPECTRA IN DOPED RUTILE

Initial studies of the effects of low temperature optical irradiation were made with sample 4, from the Al-doped National Lead boule, which showed spectra from Fe^{3+}, Cr^{3+}, Mn^{3+}, Mn^{4+}, Ni^{2+} and Ni^{3+}. Of these, the resonances of Fe^{3+}, Cr^{3+}, Mn^{4+} and Ni^{3+} were all observable at room temperature, but the presence of Mn^{3+} and Ni^{2+} could only be detected at temperatures below about 100 K due to their shorter spin-lattice relaxation times.

6.3.1 Effect of U.V. Irradiation at Low Temperatures

The specimen was cooled to 40 K in the dark and resonance lines from each of the six impurity spectra were recorded. The specimen was then subjected to ultra-violet irradiation for ten minutes, after which the spectra were re-recorded. The irradiation caused no significant change in spectrometer sensitivity. However, marked changes were observed in the e.s.r. spectra, as illustrated by Figure 6.3. The intensities of all the spectra were changed ; with those of Fe^{3+}, Cr^{3+}, Mn^{3+} and Ni^{2+} lines being decreased while, in contrast, the Ni^{3+} and Mn^{4+} intensities increased by about 100% and 40% respectively. This suggested that light-induced reactions of the type,

$$Ni^{2+} \longrightarrow Ni^{3+} + e^{-} \qquad (6.1)$$

$$Mn^{3+} \longrightarrow Mn^{4+} + e^{-} \qquad (6.2)$$

had occurred, which may be interpreted as Mn^{3+} and Ni^{2+} each releasing an electron or trapping a hole to become activated recombination centres. The photoelectronic roles of Fe^{3+} and Cr^{3+} could not, however, be determined at this stage since neither the divalent nor tetravalent states of these ions can be detected by e.s.r. The 'light-generated' substitutional Ni^{3+} spectrum, reported by Gerritsen (1962) was not seen in this sample, though it was later found in other crystals which were not deliberately doped with nickel.

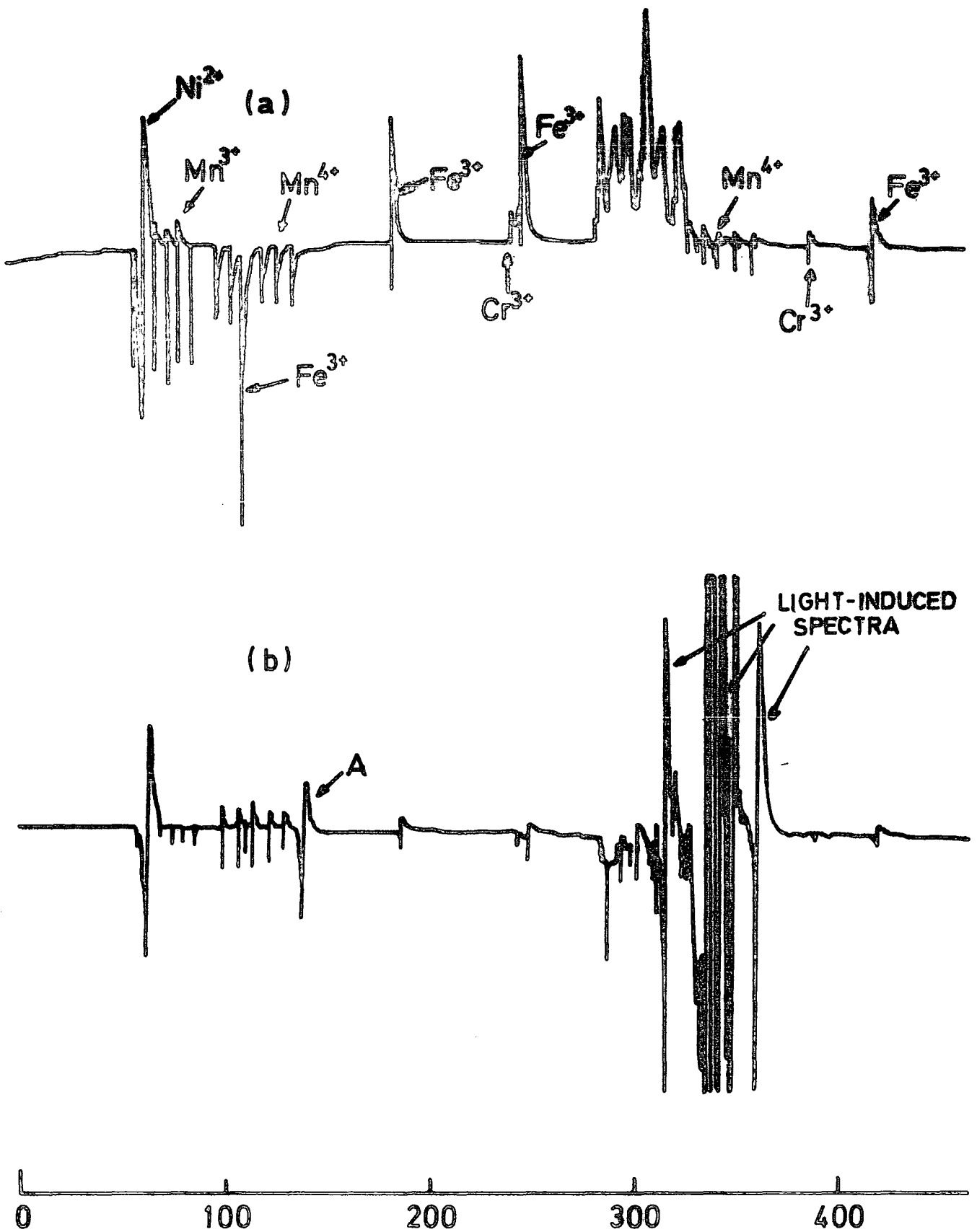

FIG.6·3. E.S.R. SPECTRA RECORDED (a) BEFORE AND (b) AFTER U.V. IRRADIATION AT 40K. (H//⟨110⟩, V = 9·129 GHz.); Ni/TiO_2(NL).

In addition to the intensity changes outlined above, several new resonance lines appeared following u.v. irradiation at 40 K. Figure 6.3, which shows the spectra for 0-5000 G sweeps of the magnetic field with the field parallel to the < 110> crystal axis, both before and after irradiation, gives a qualitative indication of the intensity changes involved though the sweep time (10 minutes) was too short to allow the detection system to respond fully to some of the narrow lines. Most of the new lines are in the magnetic field region corresponding to $g \sim 1.9$, with the significant exception of line A at $\sim$ 1400 G.

The post-irradiation intensities of all the lines remained unchanged for more than an hour, suggesting that the metastable light-induced states were thermally disconnected from the transport bands at 40 K. The effect of irradiating at lower temperatures was to produce similar changes in the impurity spectra, but the intensity of some of the light-induced spectra were reduced by power saturation when approaching liquid helium temperatures. Similar behaviour was reported with the e.s.r. spectra of γ-irradiated rutile (Purcell,1971). Variation of the microwave power level showed that saturation did not occur at 40 K and so this temperature was chosen as a reference in much of the subsequent work. The insertion during irradiation of a Chance OX1A filter, which is a band pass filter, centred on 3650 Å, had the effect of partially reducing the magnitude of the light induced intensity changes, suggesting that radiation of less than band gap energy may also be used to fill trapping centres by the direct excitation of charge from impurity centres deep in the forbidden energy gap.

In order to find the temperatures at which these optically-stimulated reactions could be thermally reversed and with the aim of producing some correlation with T.S.C. and T.L. data, the technique of isochronal annealing was employed, using a base temperature of 40 K. Fig. 6.4 demonstrates the

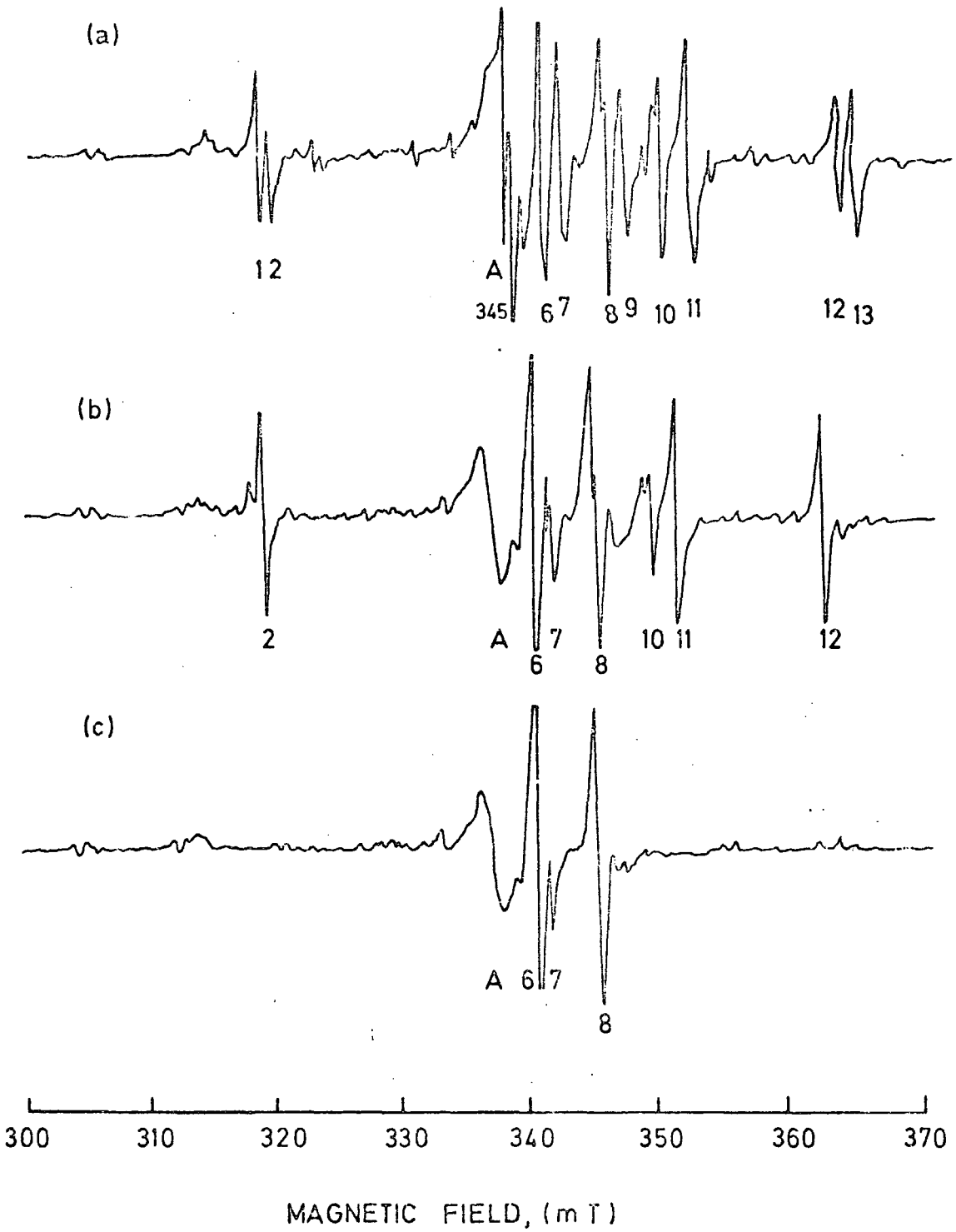

FIG 6·4 SPECTRA RECORDED AFTER (a) U.V. IRRADIATION AT 40 K (b) SUBSEQUENT HEATING TO 90K FOR 10 MINUTES, (c) HEATING TO 100K FOR 10 MINUTES ; ALL SPECTRA RECORDED AT 40K , ν = 9·129 GHz , H//⟨110⟩; Ni/TiO_2(NL)

effect of isochronal annealing on the e.s.r. spectra induced by u.v. irradiation at 40K. Following irradiation there are at least thirteen lines, Fig. 6.4(a). After heating to 90K and cooling back to 40K, some of the defects have been annealed out by being thermally reconnected with the relevant transport band and hence several of the e.s.r. lines have disappeared (Fig.6.4(b)). More lines are removed by annealing at 100K (Fig.6.4(c)). The results of this isochronal annealing at 10K intervals, between 40 and 100K,are summarized in Figure 6.5. From the temperature dependence of the amplitudes of the various lines there appear to be at least four different light-generated centres, three of which have thermal ionization tempeatures of $\sim$ 55K, $\sim$ 75K and $\sim$ 95K respectively. A fourth centre, corresponding to lines 6 & 8, and labelled centre B, was thermally emptied after heating to 120K. The amplitude-temperature profiles in Fig.6.5 are interpreted as representing the initial capture of charge by shallow trapping centres during band-gap irradiation and the subsequent release of the charge when sufficient thermal energy is available. The apparent increase in the concentration of the deeper centres as the shallow traps are emptied, representing retrapping, suggests that the centres all trap charge of the same sign, and also indicates that the traps are not initially saturated by the irradiation.

Isochronal annealing of manganese and nickel spectra produced amplitude-temperature profiles with less well-defined features (Fig.6.6). The u.v.-induced charge transfers of equation 6.1 and equation 6.2 appear to be reversed after heating to $\sim$ 100K. The coincidence of this with the temperatures at which the light-induced traps are thermally emptied suggests that the latter may correspond to electron traps and that when the trapped electrons are freed some recombine at the activated Mn^{4+} and Ni^{3+} recombination centres. An apparent slight increase in the concentration of these recombination centres with subsequent isochronal annealing to 200K is tentatively attributed to the thermal release and retrapping of holes from shallow traps of unknown identity.

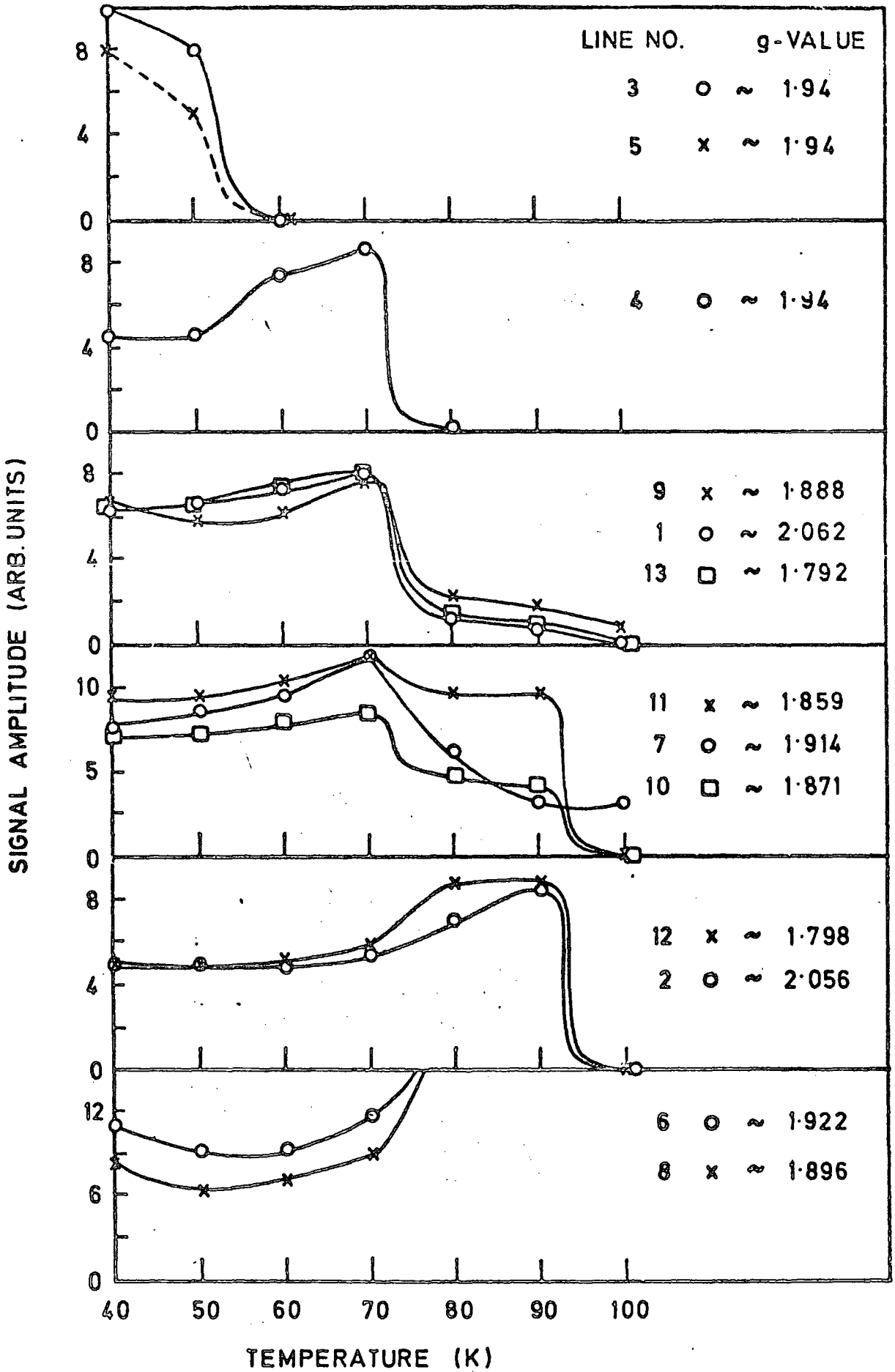

FIG. 5 EFFECT OF ISOCHRONAL ANNEALING ON E.S.R. LINE INTENSITIES, FOLLOWING U.V. IRRADIATION AT 40K. (ALL SPECTRA RECORDED AT 40K; H // ⟨110⟩.); Ni/TiO_2 (NL).

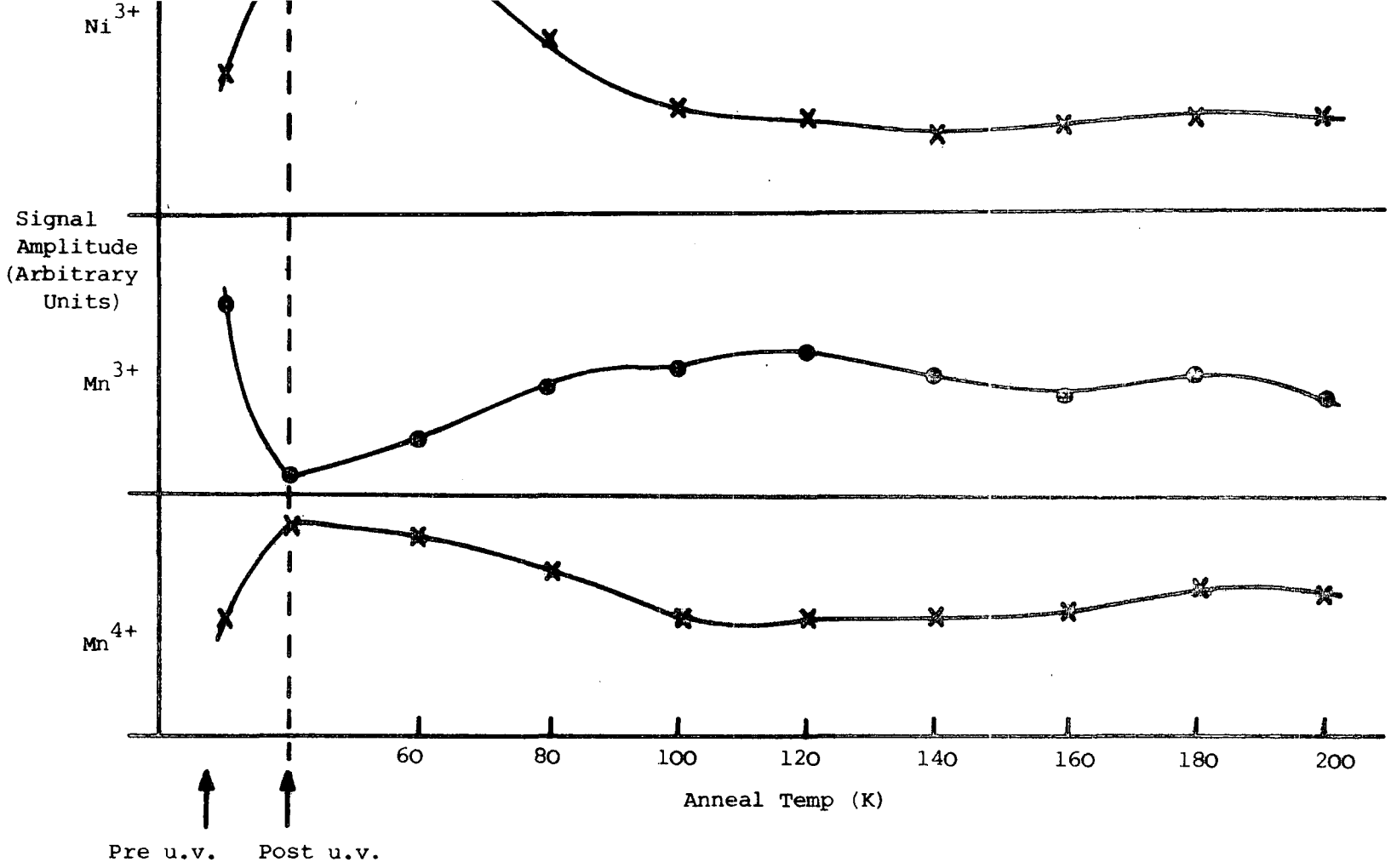

Figure 6.6 : Isochronal annealing of Ni^{3+}, Mn^{3+} and Mn^{4+} spectra, following u.v. irradiation at 40 K ; Ni/TiO_2 (N.L.)

A comparison (Fig.6.7) of the isochronal annealing curves of Fe^{3+} and centre 'A' e.s.r. spectra reveals apparently complementary features in the concentration-temperature profiles, both of which may be interpreted in the same way. In each case there are two distinct regions of population changes, at ∿ 120K and ∿ 210K for Fe^{3+} and at ∿120K and ∿ 195K for centre 'A'. Since in each case the concentration change at 120K produces a partial restoration towards pre-irradiation levels, this process cannot correspond to electrons freed from 'B' centres being recaptured at deeper electron traps, but a consistent model would designate 'A' as a recombination centre and Fe^{3+} as an empty hole trap or unactivated recombination centre which may be converted to Fe^{4+} upon u.v. excitation, with both centres being at energy levels in the lower half of the bandgap. The high temperature features of Fig.6.7 suggest either that 'A' and Fe^{4+} are thermally reconnected with the valence band at 195K and 210K respectively, or that electrons from deeper traps are recombining via these centres, which is less likely since the two events appear to occur at different temperatures. Furthermore, the distinct kinks in both profiles at ∿ 150K support the idea of the existence of a shallow hole trap which is thermally emptied at this temperature, the charge being retrapped to form more Fe^{4+} and 'A' centres. Thus the presence of defect centres not exhibiting e.s.r. spectra themselves may be inferred from their interaction and effect on the e.s.r. spectra of other centres.

The effect of isochronal annealing on Cr^{3+} spectral intensity suggested that, like Fe^{3+}, some Cr^{3+} ions are converted to Cr^{4+} by u.v. irradiation at 40K as compensation for the many shallow electron traps. With Cr^{3+}, however, the full pre-irradiation concentration is restored by annealing at ∿ 100K with no further intensity changes occurring between 100 and 300K.

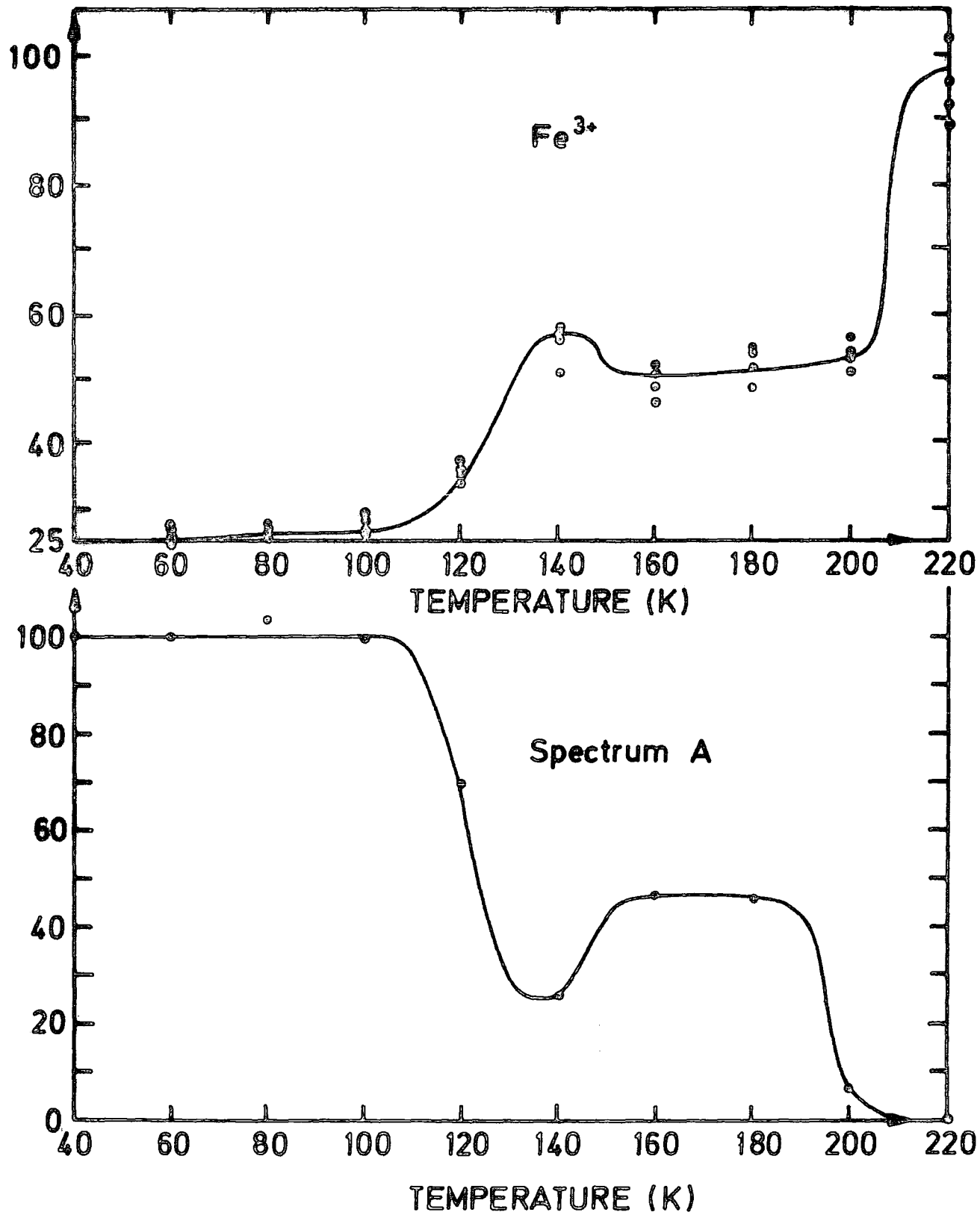

FIG6-7 EFFECT OF ISOCHRONAL ANNEALS, FOLLOWING U.V. IRRADIATION AT 40K, ON THE E.S.R. SIGNAL AMPLITUDES OF 4 Fe^{3+} LINES AND ONE LINE OF SPECTRUM A. ALL SPECTRA RECORDED AT 40K; Ni / TiO_2 (N.L).

6.4 ISOFREQUENCY ANALYSIS OF U.V.-GENERATED SPECTRA

With the aim of identifying the centres created by u.v. irradiation at 40K, isofrequency diagrams of the angular dependence of their e.s.r. spectra in the (001) and (110) planes were constructed to aid the determination of Spin Hamiltonian parameters and site symmetries.

The isolation of the 'A' centre lines from those of the other centres was relatively straightforward and the isofrequency diagram is given in Fig.6.8. This shows that the 'A' centre has the symmetry of a substitutional site. Only one transition was observed and the spectra may be described by :-

$$g_{001} = 3.36, \qquad g_{110} = 4.59, \qquad g_{1\bar{1}0} = 1.94.$$

These g-values are fairly similar to those reported by Young (1960) to describe a spectrum produced by γ-irradiation of rutile at 77K.

Isofrequency diagrams of the other light-induced spectra in the (001) and (110) planes are presented in Figs. 6.9 and 6.10 respectively. Many transitions from different spectra occur in the same magnetic field region and so, as an aid to the isolation of spectra belonging to different centres, a thermal cleaning technique was used. This involved thermally emptying the shallower traps at 100K after irradiation at 40K to allow isofrequency plotting of spectra from the deepest centre, followed by re-irradiation and subsequent thermal cleaning at successively lower temperatures, so that the spectra from the shallow centres were gradually introduced and the I.F. diagrams became more complex.

The deepest trap, centre 'B', appears to correspond to another species reported by Young et al (1960) in γ-irradiated rutile. The spectrum also has substitutional symmetry, except for an unexpected splitting with the magnetic field parallel to the <001> axis, at which orientation the theory

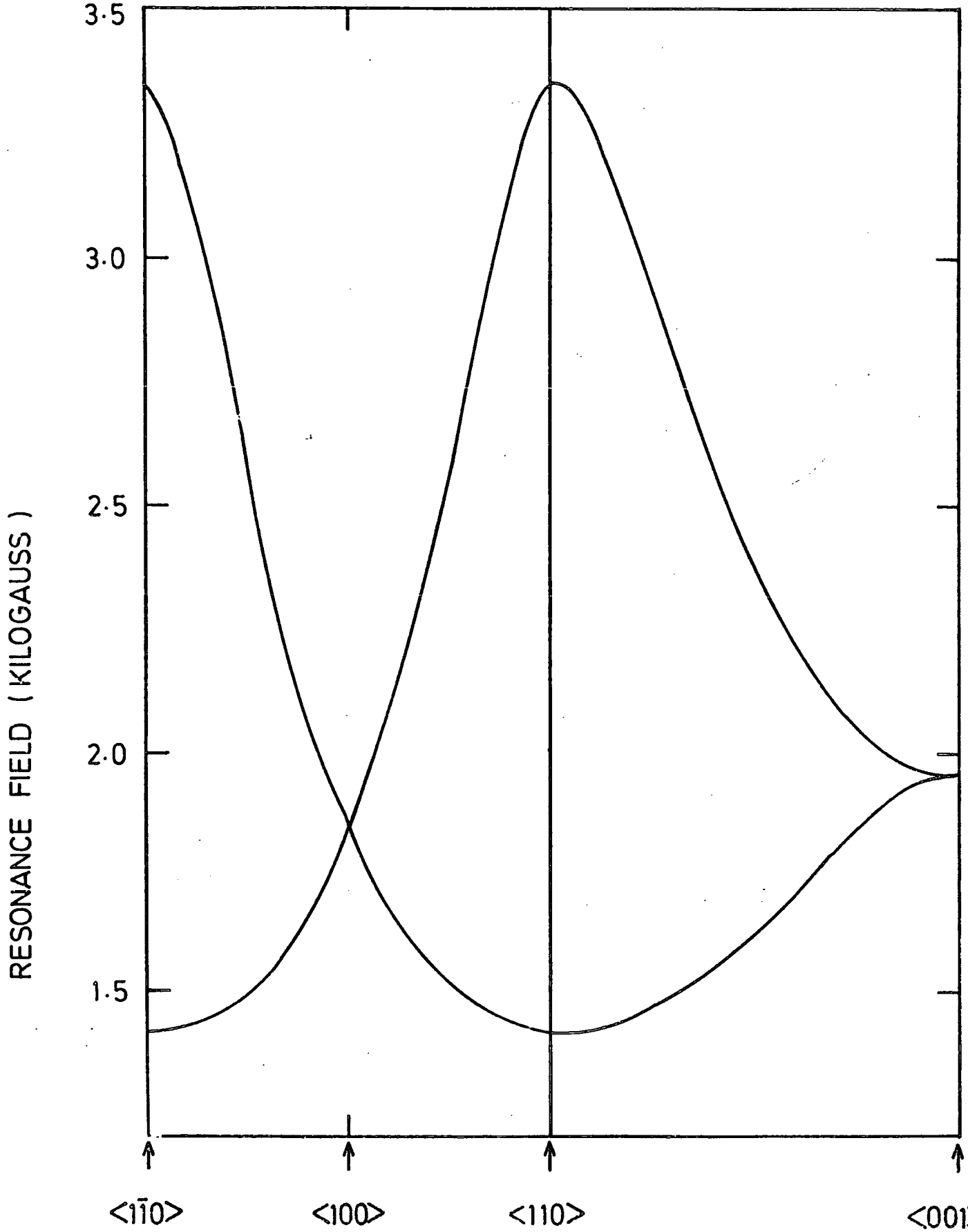

FIG. 6·8 ISOFREQUENCY DIAGRAM OF SPECTRUM A AFTER UV IRRADIATION AT 40K. ν = 9·36 GHz.

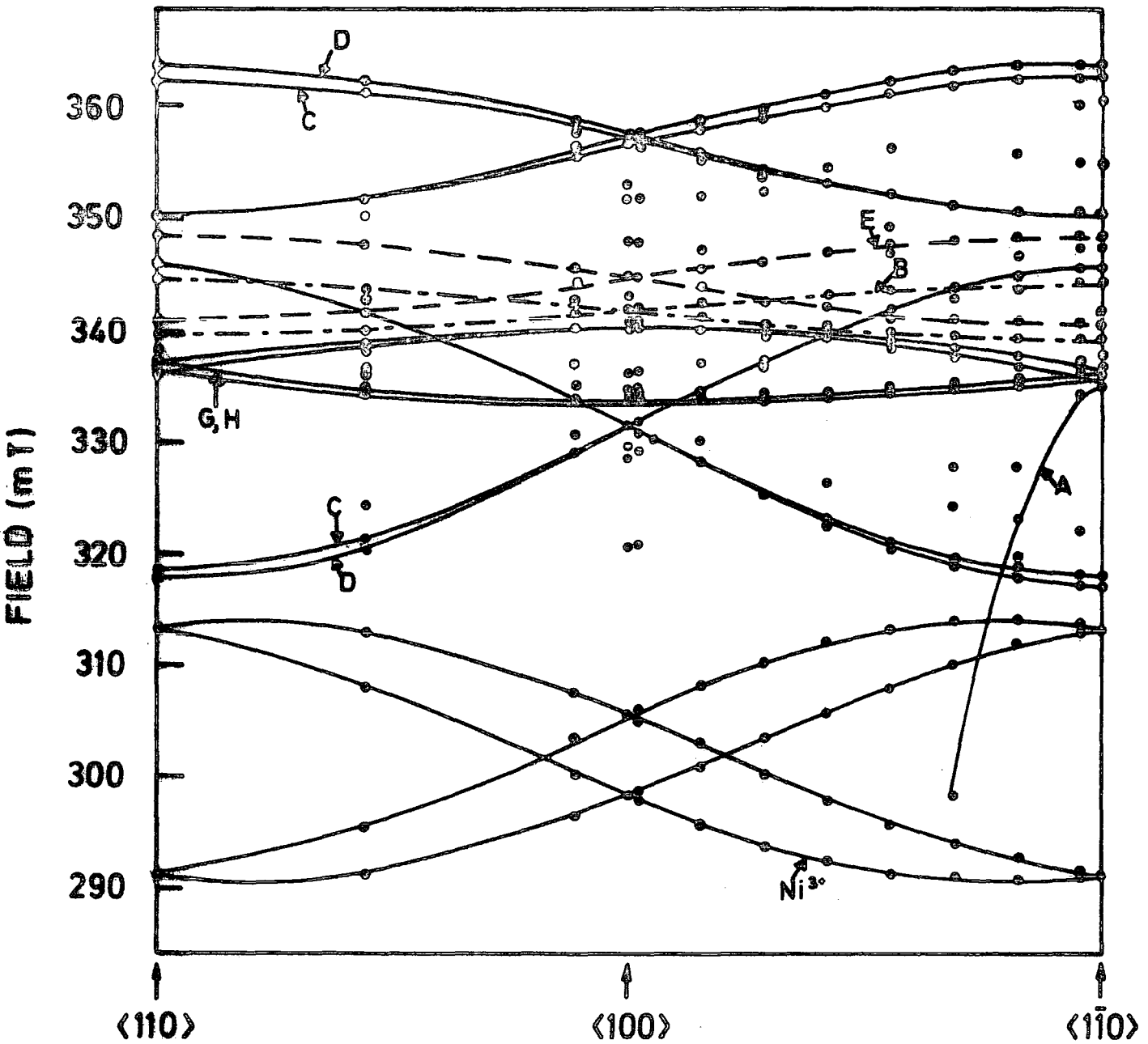

FIG.6.9. ISOFREQUENCY DIAGRAM IN (001) PLANE OF SPECTRA AFTER U.V. IRRADIATION AT 40K; ν = 9·129 GHz, Ni / TiO_2(NL).

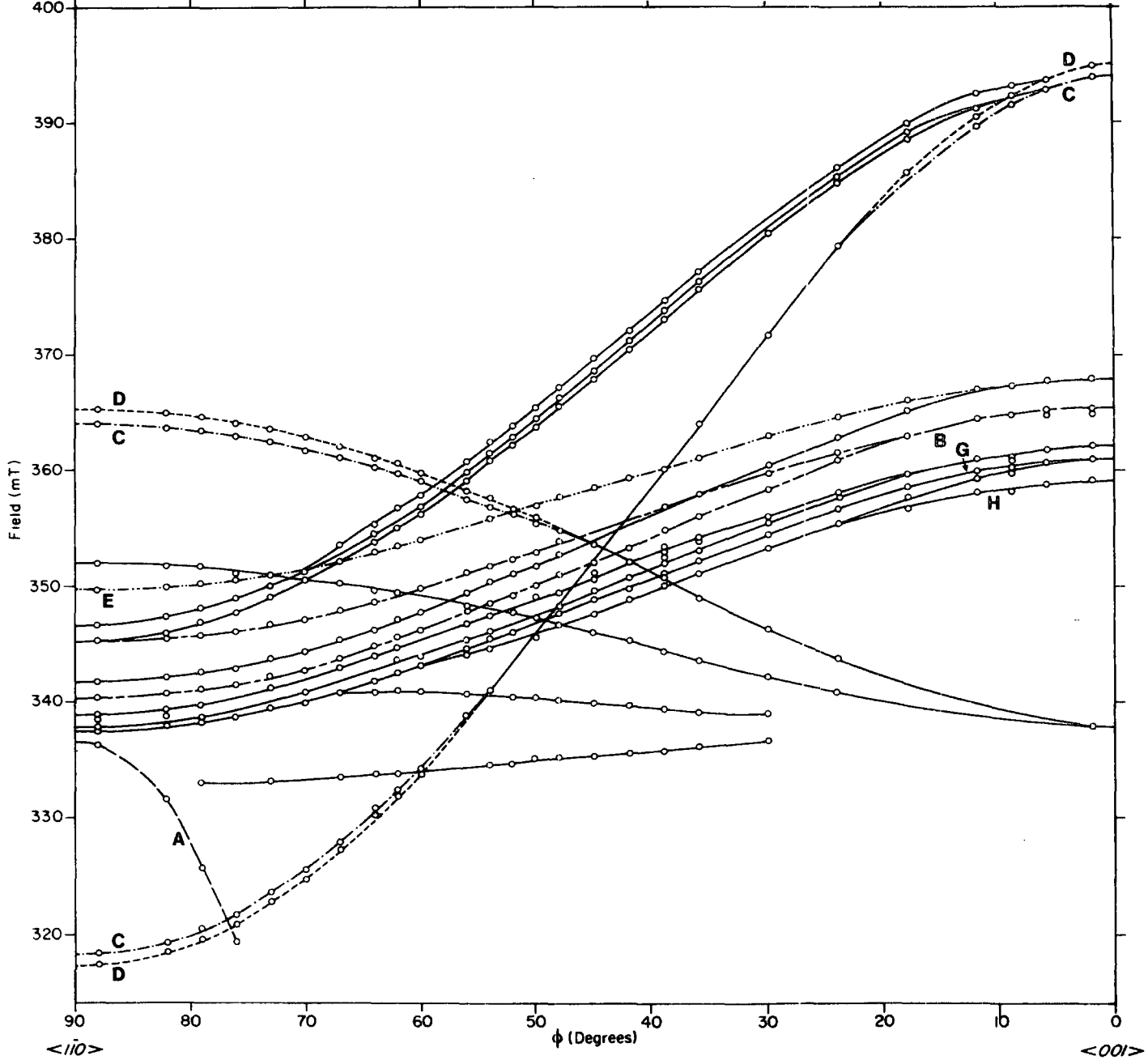

Fig. 6·10 ISOFREQUENCY DIAGRAM IN (110) PLANE OF SPECTRA PRODUCED AFTER U.V. IRRADIATION AT 40K; 9·159GHz, Ni/TiO_2(NL)

predicts that all lines should coincide. The spectrum can be described by $g_{001} = 1.793$, $g_{110} = 1.922$ and $g_{1\bar{1}0} = 1.896$. These parameters are also very similar to those reported by Chester (1964) for an e.s.r. spectrum in a heavily aluminium-doped, vacuum-reduced rutile crystal. In addition to the doublet splitting with the field along the c-axis, Chester also observed some weak hyperfine splitting by Ti^{47} and Ti^{49} isotopes at some orientations which suggested a tentative interpretation of the centre as Ti^{3+}. No Ti hyperfine lines were found in this work.

Centre C, which is thermally emptied at $\sim$ 95 K, appears to have two transitions, as would be expected for an S = 1 centre, and the spectrum can be fitted to a Spin Hamiltonian of the form

$$\mathcal{H} = g \beta H S + D \left[S_z^2 - \frac{1}{3} S (s + 1) \right] + E(S_x^2 - S_y^2)$$

The Spin Hamiltonian parameters for centre C are

$$g_{001} = 1.788, \quad g_{110} = 1.846, \quad g_{1\bar{1}0} = 1.953,$$

$$D = 0.701 \text{ GHz}, \quad E = 0.072 \text{ GHz}.$$

This centre has substitutional symmetry, with a small c-axis splitting of one of the transitions, similar to that found in centre B.

Centre D is thermally emptied at $\sim$ 75K, but its spectrum has a very similar angular dependence to that of centre C, with the lines coinciding at several orientations. The Spin Hamiltonian parameters are :

$$g_{001} = 1.785, \quad g_{110} = 1.839, \quad g_{1\bar{1}0} = 1.956,$$

$$D = 0.712 \text{ GHz}, \quad E = 0.078 \text{ GHz}.$$

Centre 'E' also thermally ionizes at $\sim$ 75K, has substitution symmetry

and only one transition, described by the following parameters :

$$g_{001} = 1.778, \quad g_{110} = 1.872, \quad g_{1\bar{1}0} = 1.915.$$

The remaining spectra were more difficult to separate, consisting of many closely-spaced lines and corresponding to at least two more centres. One, centre G, empties after isochronal annealing at $\sim$ 75K and another, centre H, by annealing at $\sim$ 55 K. Both of these shallow centres appear to have the symmetry of perturbed substitutional sites, with magnetic axes approximately parallel to the <100> , <010> and <001> crystal axes. Centre G has corresponding g-values of :

$$g_{001} = 1.811, \quad g_{100} = 1.919, \quad g_{010} = 1.956$$

Centre H has a spectrum described by :-

$$g_{001} = 1.822, \quad g_{100} = 1.92, \quad g_{010} = 1.955$$

These parameters are very similar to those of a spectrum observed by Kerssen (1973) in vacuum reduced, Aℓ-doped rutile, which was interpreted as a $Ti^{3+} - A\ell^{3+} - A\ell^{3+}$ complex.

For convenience of reference it is helpful to summarise the symbolism used to refer to the individual trapping centres and the e.s.r. lines to which they give rise.

The relation between the line numbers in Figs. 6.4 and 6.5 and the centres to which the lines belong is given below :-

Centre	Lines
B	6,8
C	2,9,11,12
D	1,9,11,13
E	7,10
G,H	3,4,5

6.5 DYNAMIC E.S.R. MEASUREMENTS

One advantage of using the electron spin resonance technique to study low-temperature photo-stimulated charge transfers is that, providing the irradiation does not affect spectrometer sensitivity, for example by causing excessive photoconductivity, it is possible to measure changes in the concentrations of the paramagnetic defects involved, both during and after irradiation, by repeatedly sweeping through the resonance lines at regular intervals. This can then lead to a determination of relative reaction rates and their variation with temperature.

Fig. 6.11 shows the simultaneous growth of signal amplitude with time of irradiation of resonance lines from centres B,C,D & E, and Fig.6.12 provides a plot of $\ell n(I_\infty - I_t)$ against time, where I_t is the peak-to-peak amplitude at time t and I_∞ is the amplitude when an equilibrium condition has been reached where no further change takes place. This shows that the filling of the trapping centres follows an exponential growth which can be characterized by time constants, τ. The relative magnitude of these time constants provide an indication of the relative capture cross-sections of the centres in competing for the excess charge in the conduction bands. From Fig.6.12 it may be concluded that centre B has the highest capture cross-section (shortest τ) of those measured and that C & D have the smallest. That there is no further change of amplitude, and hence of defect concentrations, after irradiation, suggests that the electrons in the traps are effectively isolated from each other and from the conduction band at this temperature ($\sim$ 40 K). This may be contrasted with the behaviour shown in Fig.6.13 which presents the growth of 'A' centre concentration during and after u.v. irradiation. During irradiation there is an exponential growth, which can be characterised (Fig.6.14) by a time constant, τ, of $\sim$ 3-5 min. and which reaches an equilibrium state after $\sim$ 12 minutes. On closing the shutter on the cavity optical window, however, the signal amplitude undergoes a further exponential growth

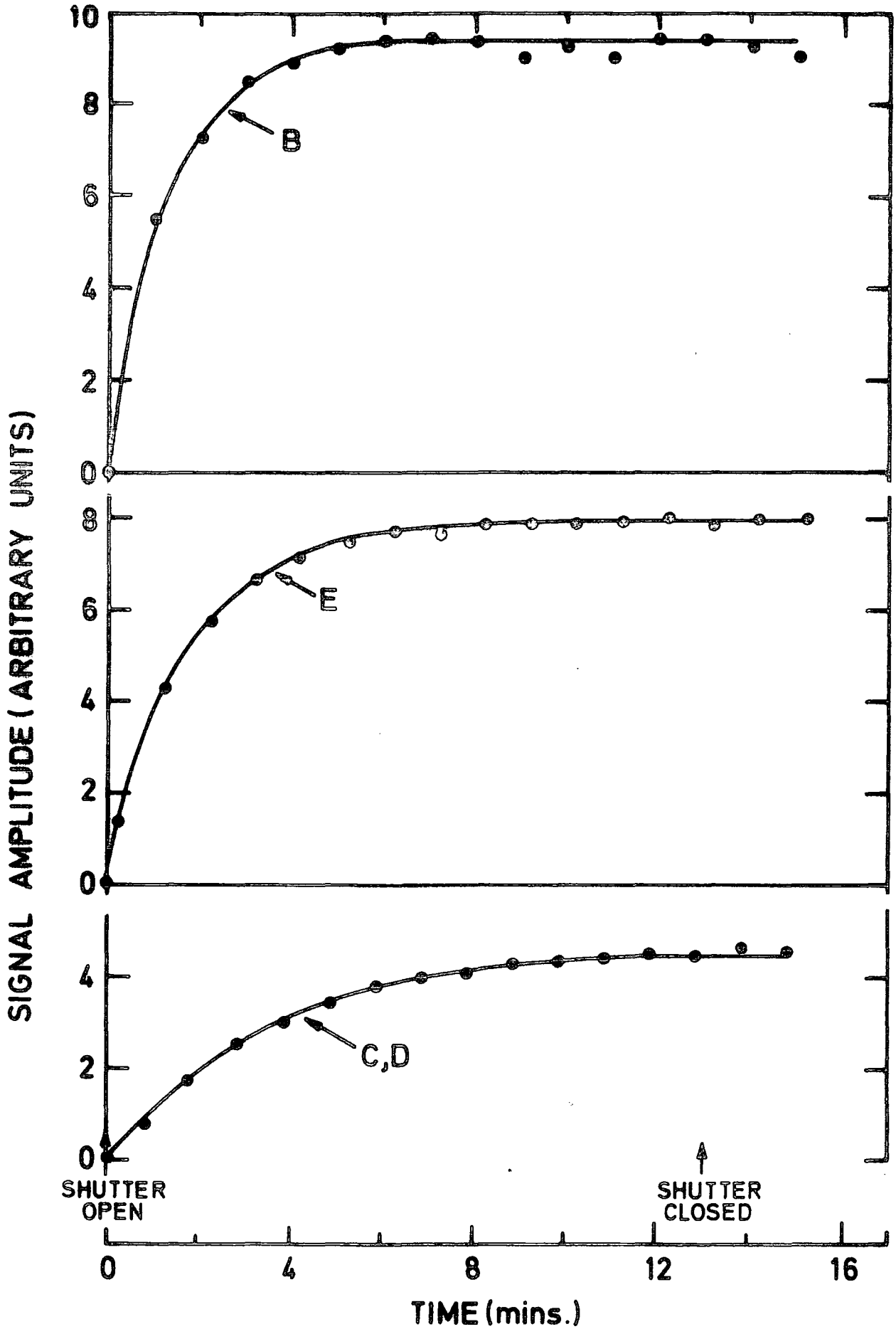

FIG.6·11 Growth of signal amplitude of species B,C,D & E during u.v. irradiation at 40K; Ni/TiO_2 (NL).

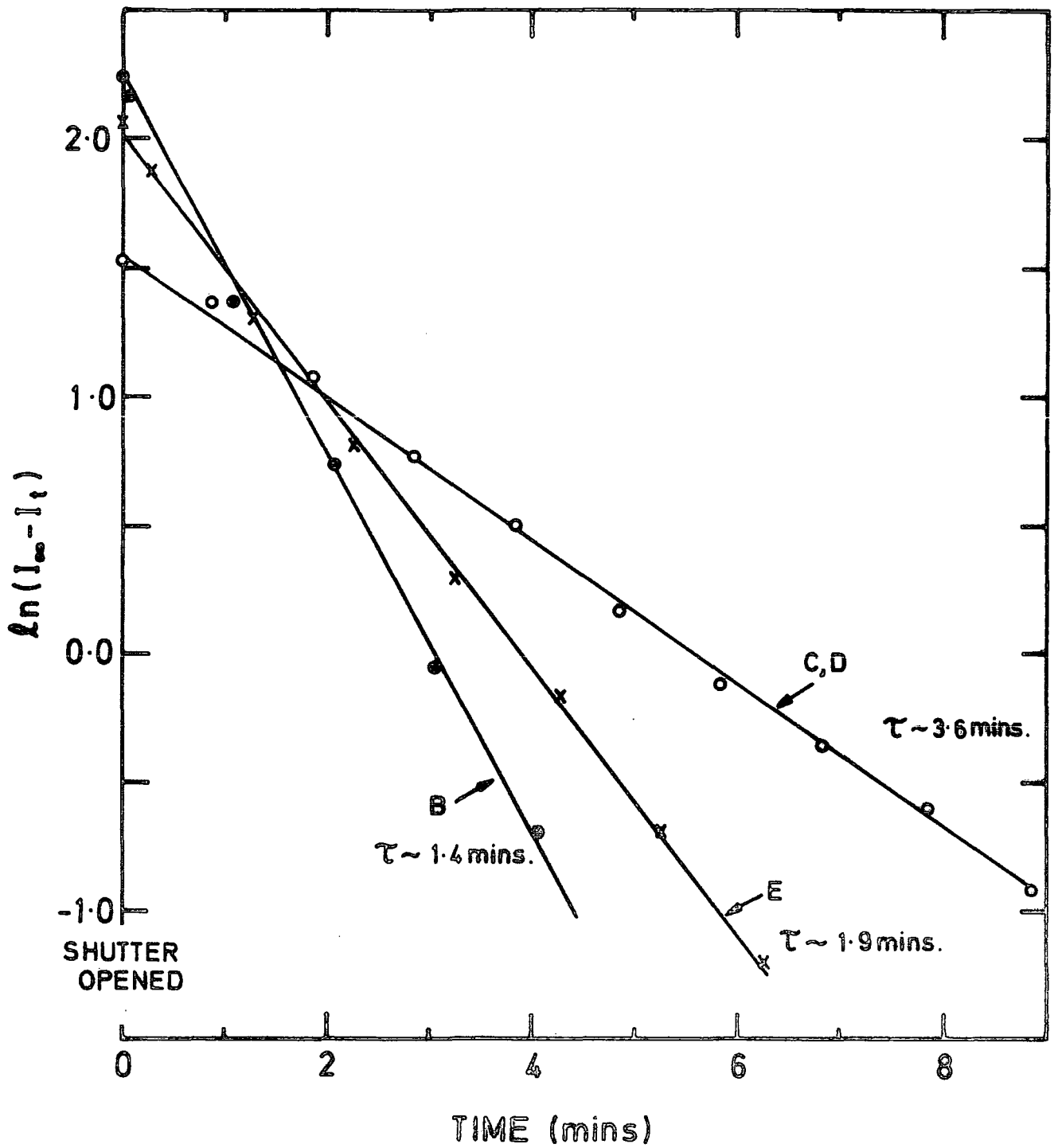

FIG.6·12 Variation of $\ell n(I_\infty - I_t)$ of signals B,C,D and E during u.v. irradiation at 40K.

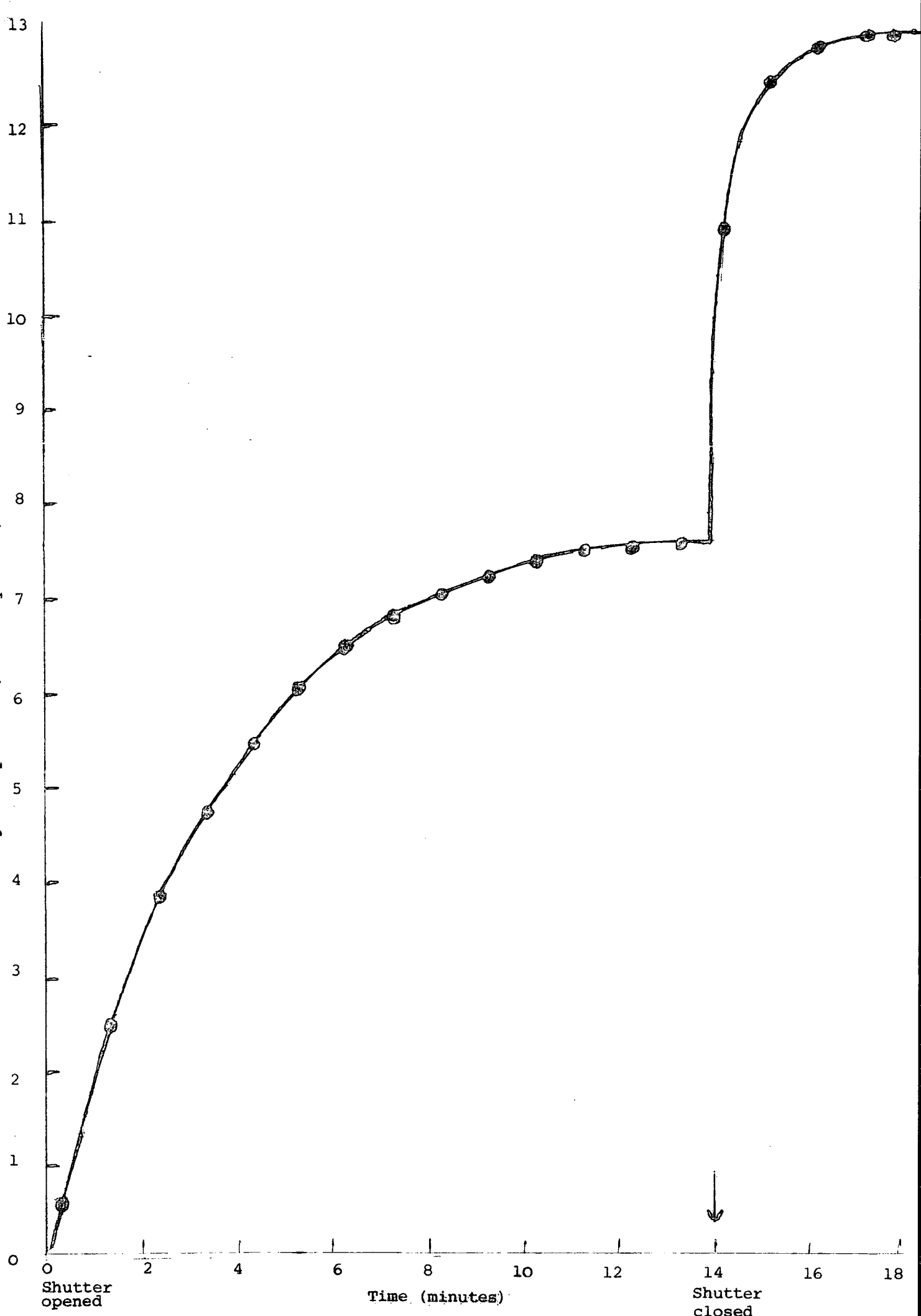

Figure 6.13 : Growth of amplitude of signal A during and after u.v. irradiation

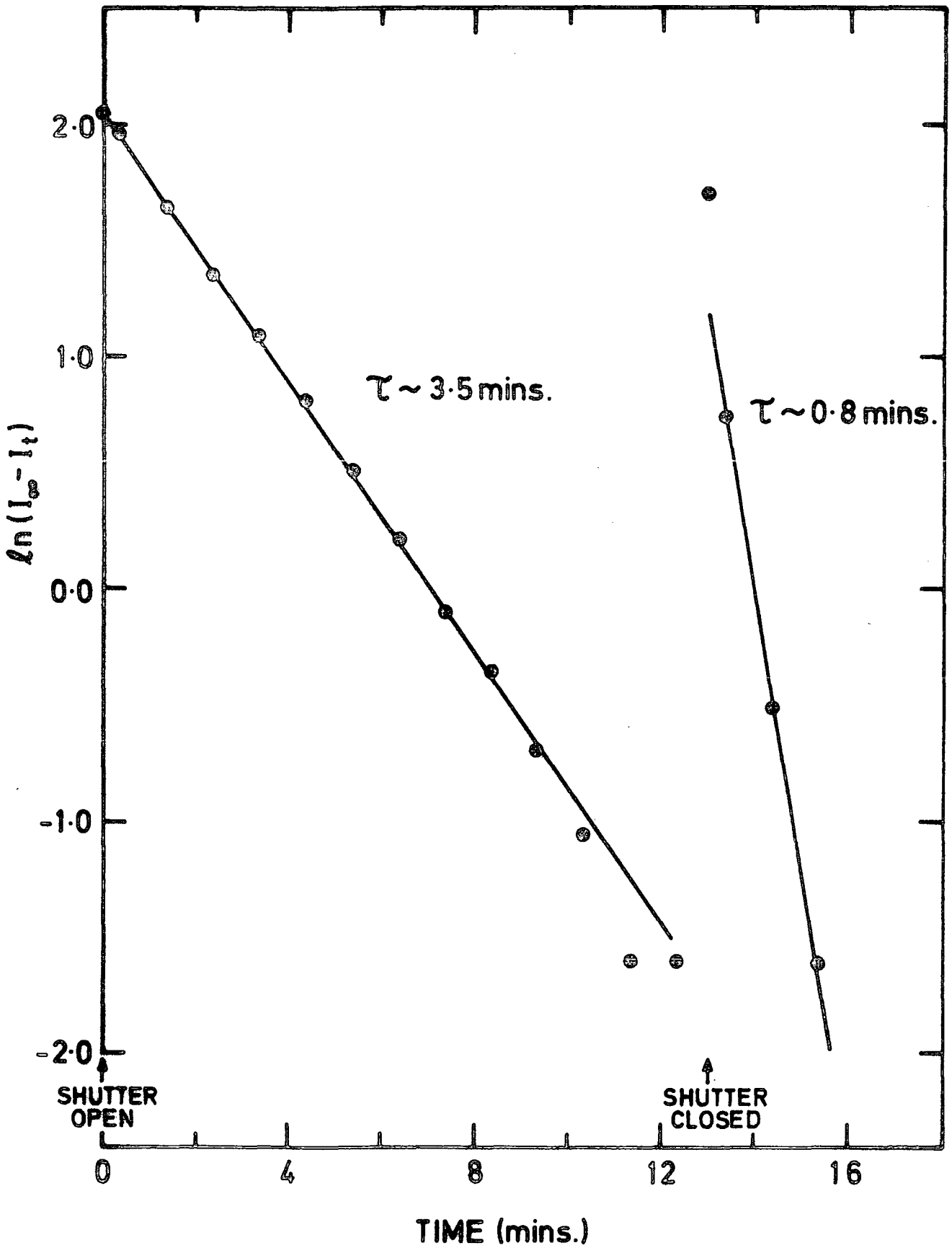

FIG.6-14 Variation of $\ell n(I_\infty - I_t)$ of signal 'A' with time, during and after u.v. irradiation at 40K.

with a time constant of $\sim$ 1 minute. A similar behaviour was observed with the decay of the Fe^{3+} spectra following irradiation at 40 K where an exponential decay of amplitude during irradiation was followed by a faster decay when the shutter was closed. This post-irradiation effect on the concentrations of defects which have already been designated as hole traps suggests the existence of another, relatively shallow, hole-trapping defect which is, however, still in thermal equilibrium with the valence band at 40K. Thus, during irradiation these traps are at least partially filled with holes, but when the irradiating source is removed, the traps rapidly empty and the holes are retrapped at Fe^{3+} and 'A' centres. Further evidence to support this interpretation is provided by the lack of any corresponding post-irradiation changes in the concentrations of filled electron traps, centres B-H.

6.6 THE EFFECT OF VARYING IRRADIATION TEMPERATURE

With spectra which do not broaden appreciably as the temperature is raised it is possible to use the effect of irradiating at varying temperatures, as an alternative method to isochronal annealing, in the investigation of the thermally stimulated charge-transfers. A series of isothermal measurements at temperatures of interest can then yield further information which may lead to estimations of trapping parameters such as ionization energies.

Fig.6.15 summarizes a series of isothermal measurements of the variation of Fe^{3+} spectral amplitude, during and after u.v. irradiation at a range of temperatures between 60 and 230 K. Between each set of measurements the sample was heated to 250 K for 10 minutes in order to empty the traps and to provide a standard pre-irradiation equilibrium condition. For ease of comparison, the signal amplitudes in Fig.6.15 are normalized with respect to their pre-irradiation values. The main conclusions to be drawn from this experiment are broadly in agreement with those from isochronal annealing data, that there are two temperatures, $\sim$ 120 and 200 K, at which thermally-stimulated charge

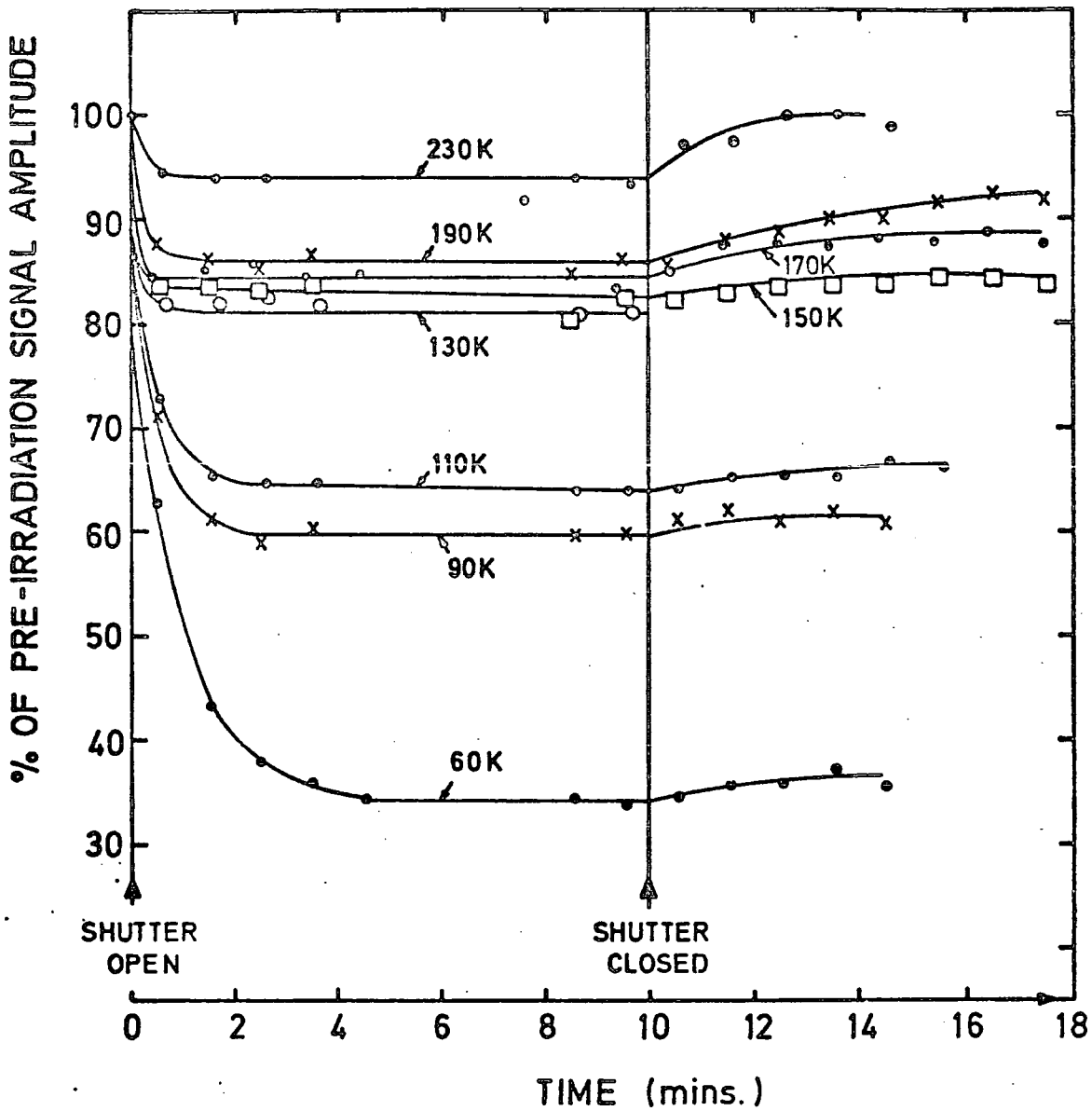

FIG 6.15 VARIATION OF AMPLITUDE OF Fe^{3+} LINE, DURING AND AFTER IRRADIATION, AS A FUNCTION OF TEMPERATURE OF IRRADIATION.

transfers take place to affect Fe^{3+} concentrations. At temperatures above $\sim$ 200 K the Fe^{4+} energy level is in good thermal contact with the valence band, i.e. Maxwell-Boltzmann statistics dictate that any electron excited by optical energy from a Fe^{3+} ion to the conduction band can be rapidly replaced by another electron from the valence band. Hence, at 230 K only about 6% of the Fe^{3+} ions are converted to Fe^{4+} by u.v. irradiation and the reaction is quickly reversed when irradiation ceases. Between 130 K and 190 K, however, the degree of optically-induced concentration change remains fairly constant, though the rate of the recovery reaction decreases as the temperature is lowered because the probability of charge having sufficient energy to escape is reduced. Irradiating at 110 K causes a significantly larger fall in Fe^{3+} concentration and this is interpreted as a greater number of Fe^{4+} centres, i.e. holes trapped at Fe^{3+}, being required to compensate for the electrons being trapped at B centres (e^- traps) at temperatures below about 120 K. Similarly, at 60 K many of the other shallow centres are capable of trapping electrons and so a correspondingly larger number of Fe^{4+} ions is needed for compensation. Fig. 6.16 shows the approximate temperature profiles corresponding to the effect on the signal amplitudes of four Ni^{3+}, two Cr^{3+}, and four Fe^{3+} lines of u.v. irradiation at temperatures between 60 K and 230 K. The Cr^{3+} concentration appears to be unaffected by irradiation at temperatures above about 120 K. At lower temperatures the intensity decrease profile is similar to that of Fe^{3+}, which suggests that Cr^{3+} ions are trapping holes to compensate for shallow electron traps. This is in agreement with isochronal annealing data. Similarly, it appears that below 120 K the large increase in Ni^{3+} concentration is due to the loss of electrons by Ni^{2+} ions, which then behave as hole traps or recombination centres. The behaviour at higher temperatures, however, suggests that here Ni may be acting as an electron trap, since irradiation at temperatures between 130-230 K causes a decrease in Ni^{3+} concentration, presumably due to some ions being converted to Ni^{2+} by trapping

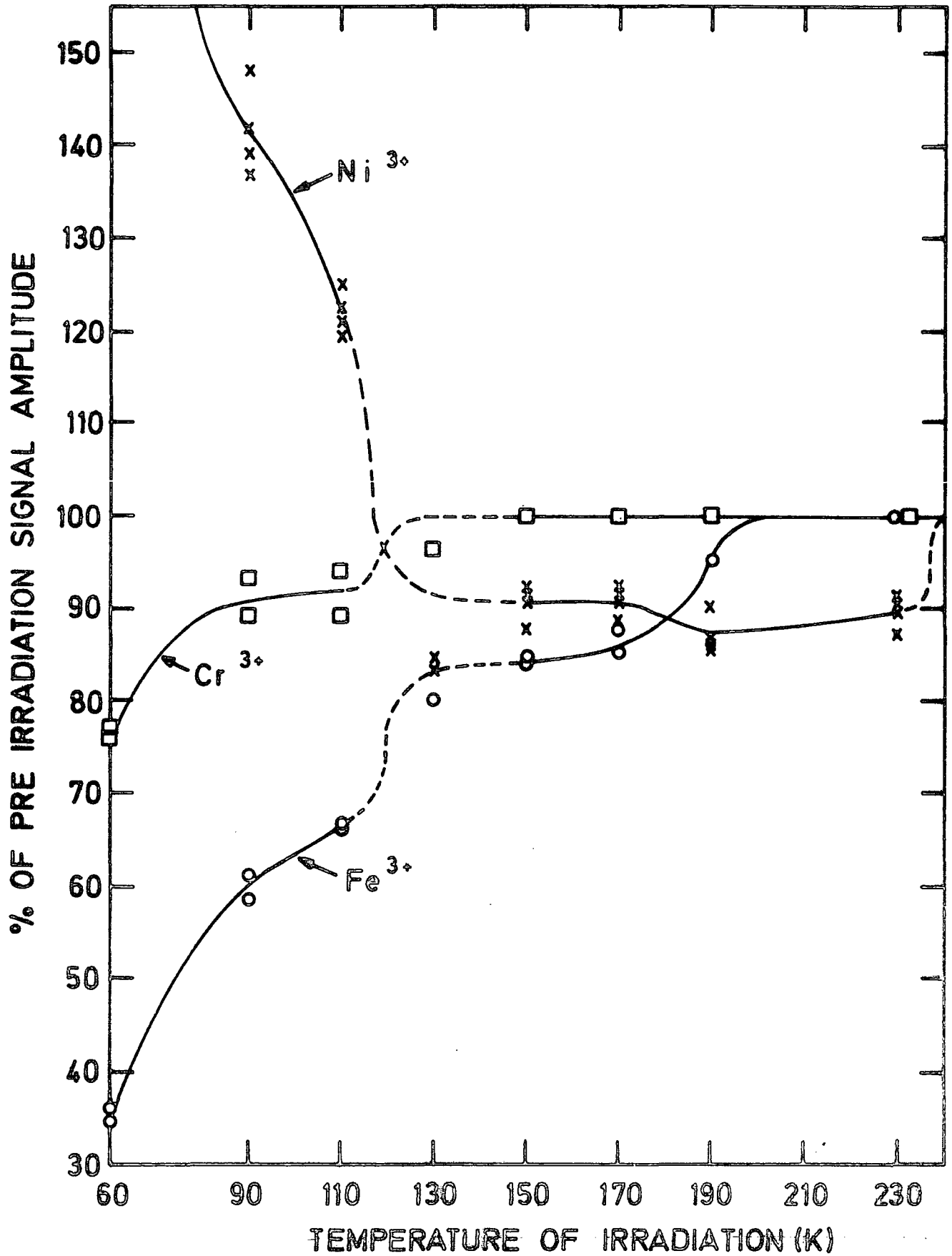

FIG.6·16 THE EFFECT OF U.V. IRRADIATION ON THE E.S.R. SIGNAL AMPLITUDES OF TWO Fe^{3+}, TWO Cr^{3+} AND FOUR Ni^{3+} LINES, AS A FUNCTION OF THE TEMPERATURE OF IRRADIATION. THE SAMPLE WAS HEATED TO 250 K FOR 10 MINUTES BETWEEN EACH SET OF MEASURMENTS. Ni / TiO_2 (NL).

electrons, though this cannot be verified, as the Ni^{2+} resonance spectrum broadens rapidly at temperatures above 100 K. If this interpretation is correct then either electrons trapped at the Ni ions are thermally freed, or holes released from other centres are retrapped, at $\sim$ 240 K, since the same decrease of Ni^{3+} concentration was observed with irradiation at each temperature between 130 and 230 K even though the temperature was cycled up to 250 K between each set of measurements to provide a standard pre-irradiation condition.

6.7 ESTIMATION OF ACTIVATION ENERGIES FROM ISOTHERMAL RECOVERY RATES

When the optical filling of traps takes place at temperatures where the trapped charge is in good thermal contact with the relevant transport band, measurement of the variation of post-irradiation thermally activated ionization rates with temperature can lead to the determination of trap depths using the simple theory outlined below.

This theory assumes a model of a single set of trapping levels in the forbidden energy gap, separated from the conduction band by an energy E, together with a single set of recombination centres near the centre of the band gap. If all the traps are initially filled by the incidence of band gap radiation then, at a given temperature, the probability, P, of a trapped electron being released into the conduction band is given by :-

$$P = \nu \exp\left\{\frac{-E}{kT}\right\} \qquad (6.4)$$

where k is Boltzmann's constant, T, is the temperature and ν is the attempt-to-escape frequency, which is the product of the electron velocity, the density of states in the conduction band and the electron capture cross-section in the conduction band. If ν is assumed to be independent of temperature, which is reasonable over small temperature ranges, then a plot of $\ell n\ P$ vs. $1/T$ will give a line of gradient $-E/k$ and hence a value of the trap depth, E.

Assuming that first order, monomolecular kinetics prevail, i.e. neglecting retrapping by assuming that the capture-cross-section of the recombination centre is much greater than that of trapping centre, then the number, n_t, of trapped carriers at time t can be described by :

$$n_t = n_o \exp^{(-pt)} \qquad (6.5)$$

where n_o is the number of filled traps when t = 0. Hence a plot of $\ell n\ n_t$ vs. t will yield a straight line of slope-p.

Providing microwave power saturation does not occur, the peak-to-peak amplitude of an electron spin resonance signal is a parameter which is directly proportional to defect concentration and therefore a series of isothermal measurements of amplitude, I, should also lead, via a plot of ℓn I vs. t (or $\ell n(I_\infty - I_t)$ vs. t when measuring the relative concentration of empty traps as with Fe^{3+}) to a value of trap-emptying probability, P. Furthermore, the variation of P with temperature can be measured and hence, using eqn. 6.4 the trap depth may be determined.

Obviously, some of the assumptions adopted in this model constitute gross over-simplifications of the real situation. First, it has already been shown that there are a wide variety of defects in rutile which occupy different energy levels in the band gap. Moreover, the assumption of monomolecular-kinetics is probably unjustified in rutile, where it appears that the kinetics are intermediate between the two extremes of fast-retrapping and no-retrapping. If this is so, however, estimates of trap depth may still be made, by studying the initial sections of thermal recovery curves, since in these regions the number of centres available to retrap charge is comparatively small and hence the reaction is essentially monomolecular.

Isothermal recovery curves of Fe^{3+} spectra following u.v. irradiation

in the temperature range of 180-200 K are presented in Fig.6.17 and corresponding plots of $\ell n(I_\infty - I_t)$ vs. time, where I_t and I_∞ are the peak-to-peak amplitudes at time t and when equilibrium is reached respectively, are shown in Fig.6.18. The apparently large fluctuations in some of the points is due to the fact that only relatively small changes in signal amplitude were being measured in this case. Nevertheless, it is still possible to fit the points of Fig.6.18 to straight lines with confidence,indicating an exponential decay of trap density and enabling the calculation of nominal values of escape probabilities, P, at the various temperatures. Fig.6.19 is a plot of ℓn P vs. $^{1}/_{T}$ which gives an activation energy, E, of $\sim$ 0.52 eV.

Unfortunately, it was not possible to perform this type of experiment on all of the spectra which undergo reversible intensity changes with irradiation, since some of them, e.g. spectra A, B and E, broaden at temperatures below those sufficient to allow thermal activation of the trapped charge, and others, e.g. Cr^{3+}, C and D experienced relative intensity changes which were too small to yield quantitative results.

The technique was used, however, to investigate the thermal emptying of centre H, one of the shallow electron traps. The isothermal decay curves following u.v. irradiation at temperatures between 40 and 49 K are shown in Fig.6.20 and corresponding plots of ℓn I vs. time, which appear to show initial monomolecular decay, followed by a slower bimolecular decay as retrapping beings to dominate, are presented in Fig. 6.21. A plot of ℓn P vs. $^{1}/_{T}$ (Fig. 6.22) shows that this trap is situated at an energy level about 0.12 eV below the conduction band.

Isothermal decay measurements on signal 'G' only gave useful results at two temperatures (shown in Fig.6.23), from which the variation of escape probability with temperature, as indicated in Fig. 6.24, suggests that this centre also has a trap depth of $\sim$ 0.12 eV.

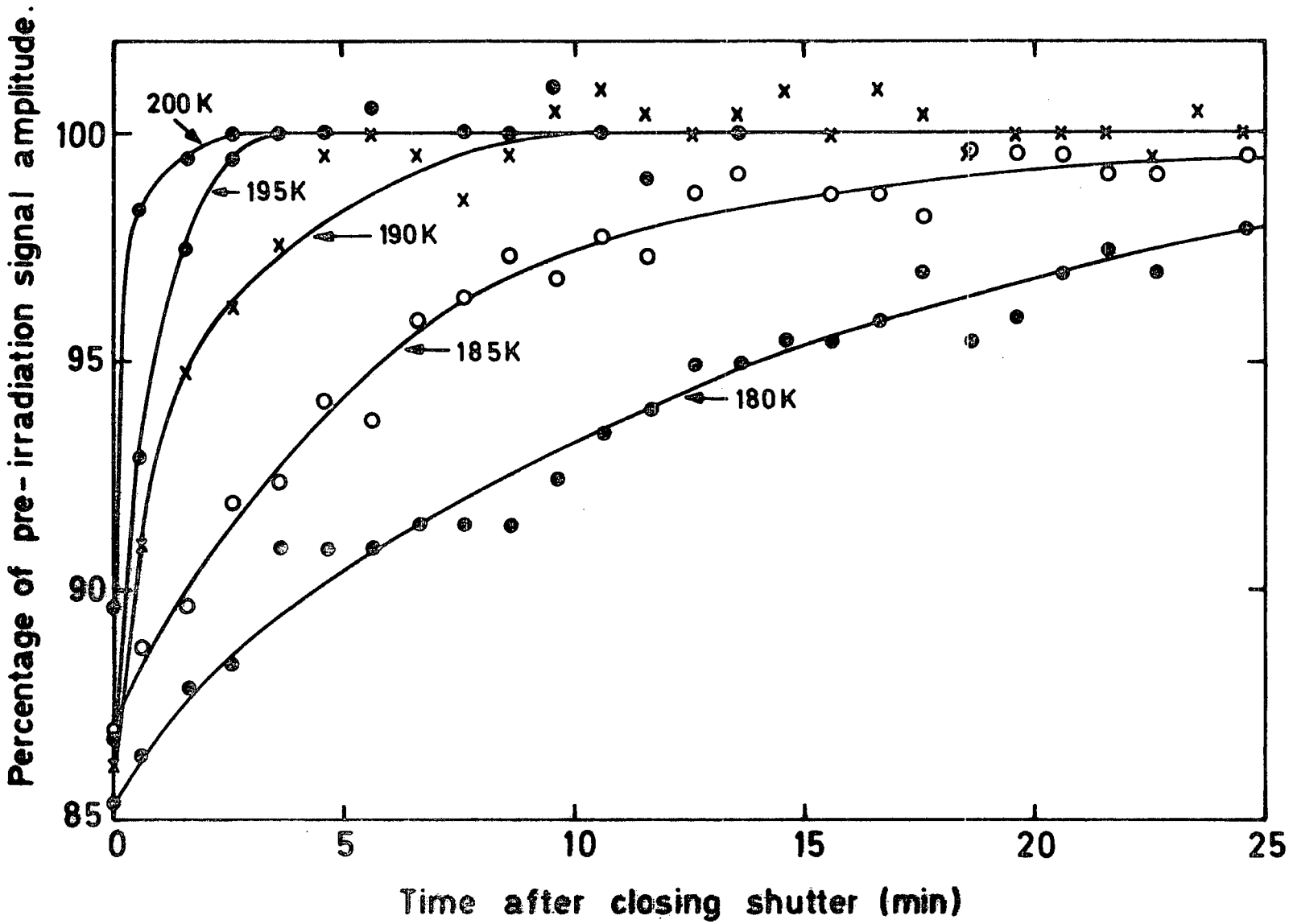

FIG.6·17 Isothermal recovery of Fe^{3+} signal amplitude following u.v. irradiation at temperatures between 180 and 200K ; Ni/TiO_2(NL)

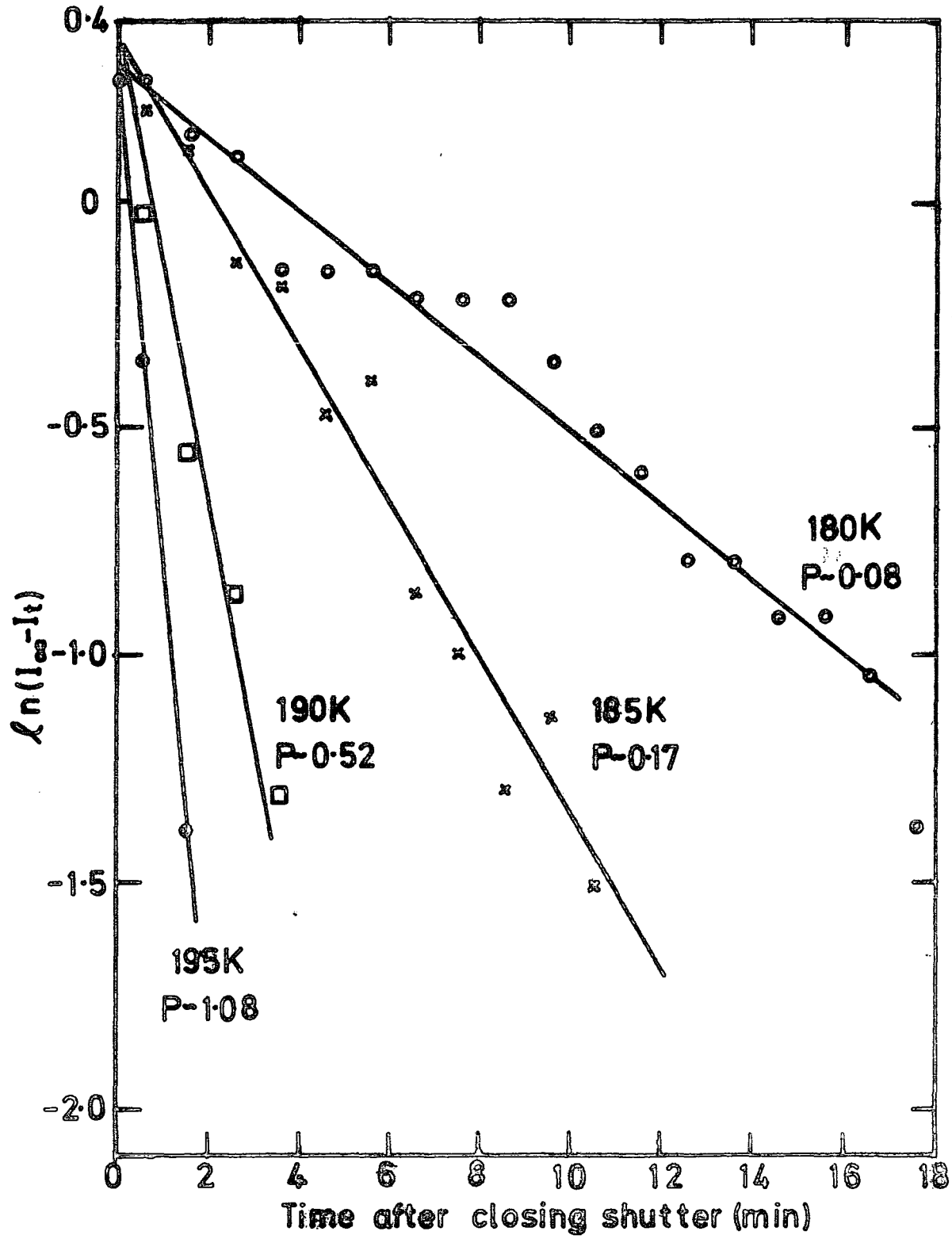

FIG.6·18 Variation of $\ell n(I_\infty - I_t)$ with time, for the isothermal recovery rates of Fe^{3+} following u.v. irradiation; Ni/TiO_2(NL).

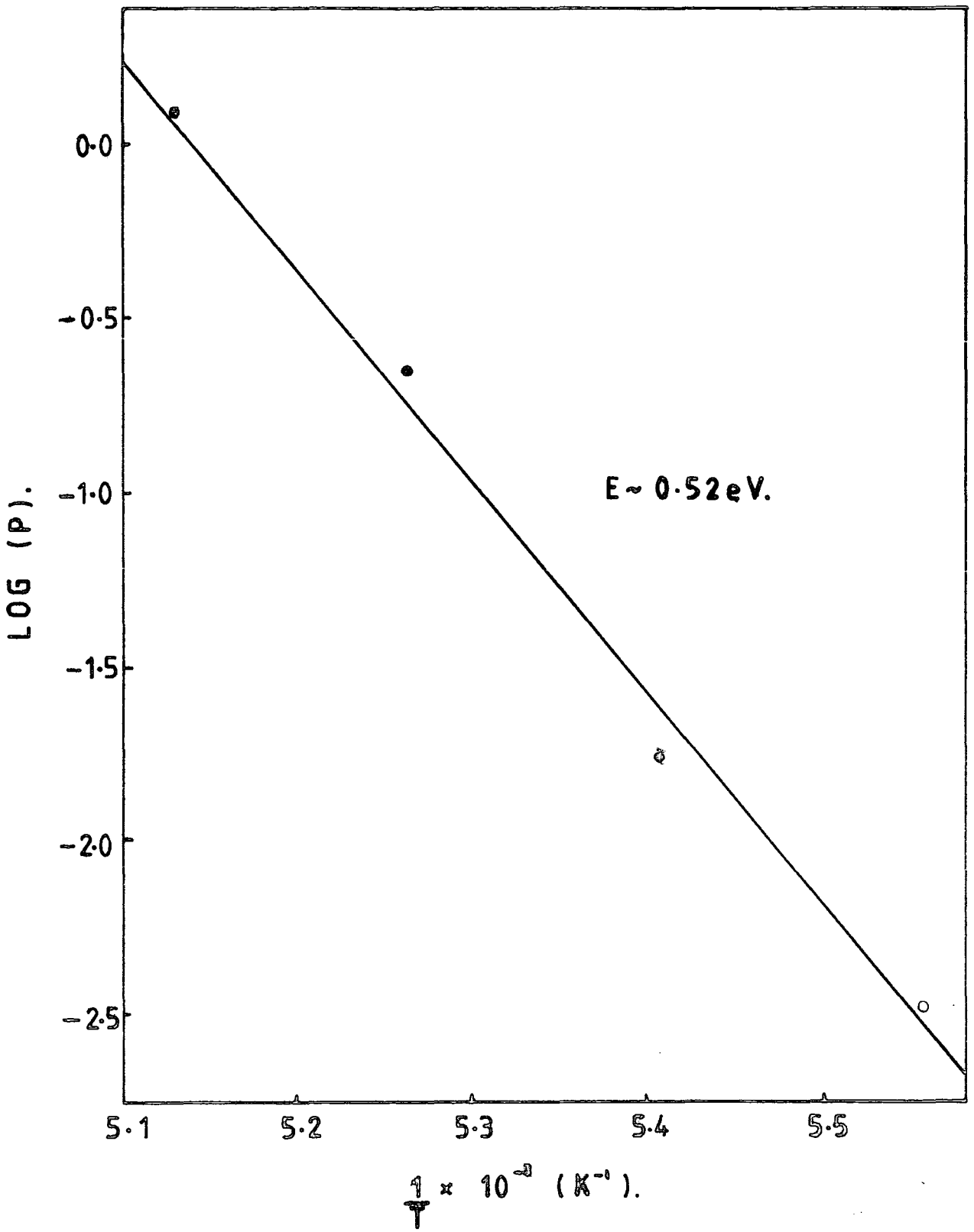

FIG.6·19 VARIATION OF LOG (P) WITH $\frac{1}{T}$,

FOR Fe^{3+} IN Ni/TiO_2 (N.L.).

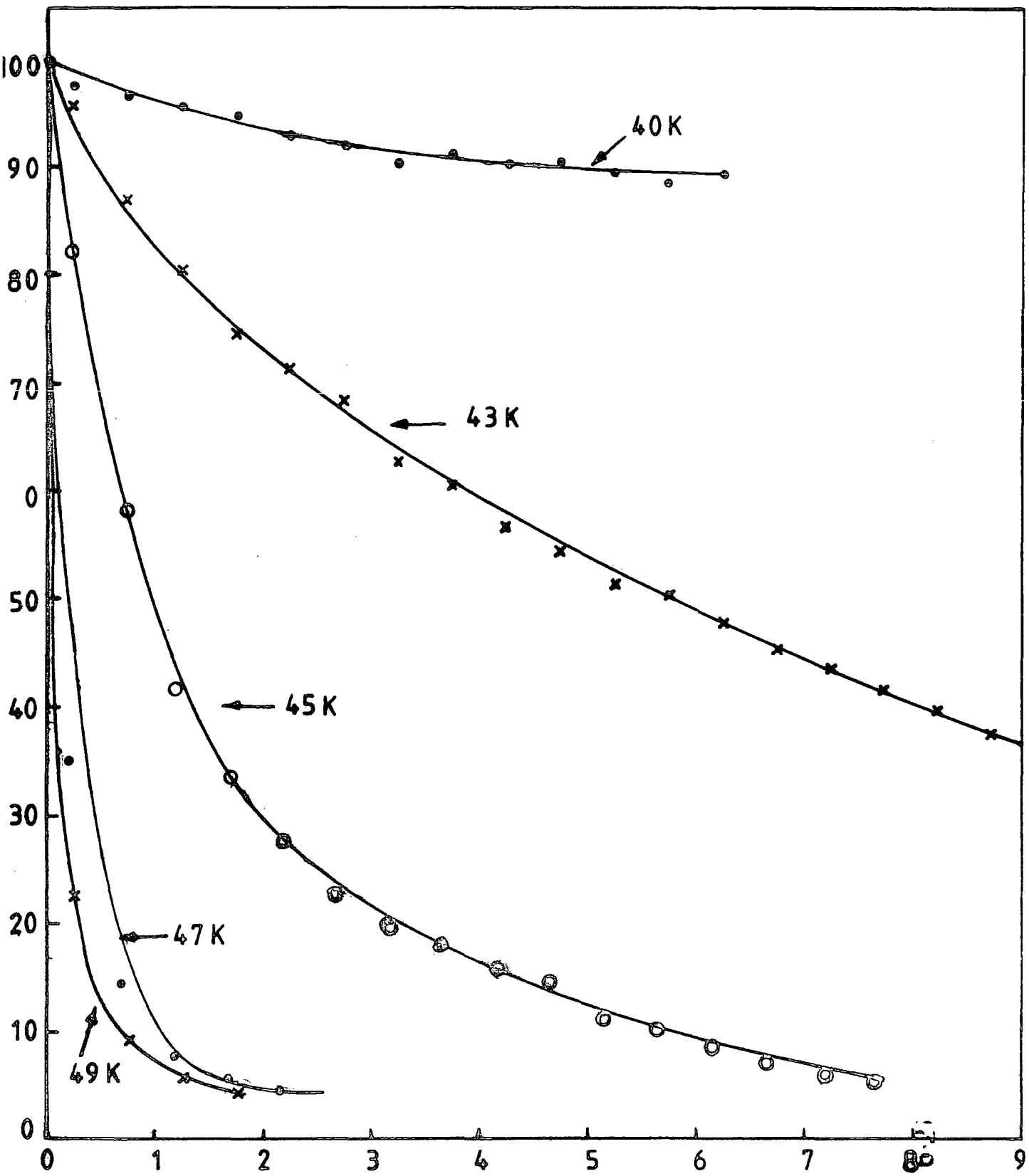

FIG. 6·20 ISOTHERMAL DECAY OF SIGNAL H FOLLOWING u.v. IRRADIATION ; Ni/TiO_2 (N.L.).

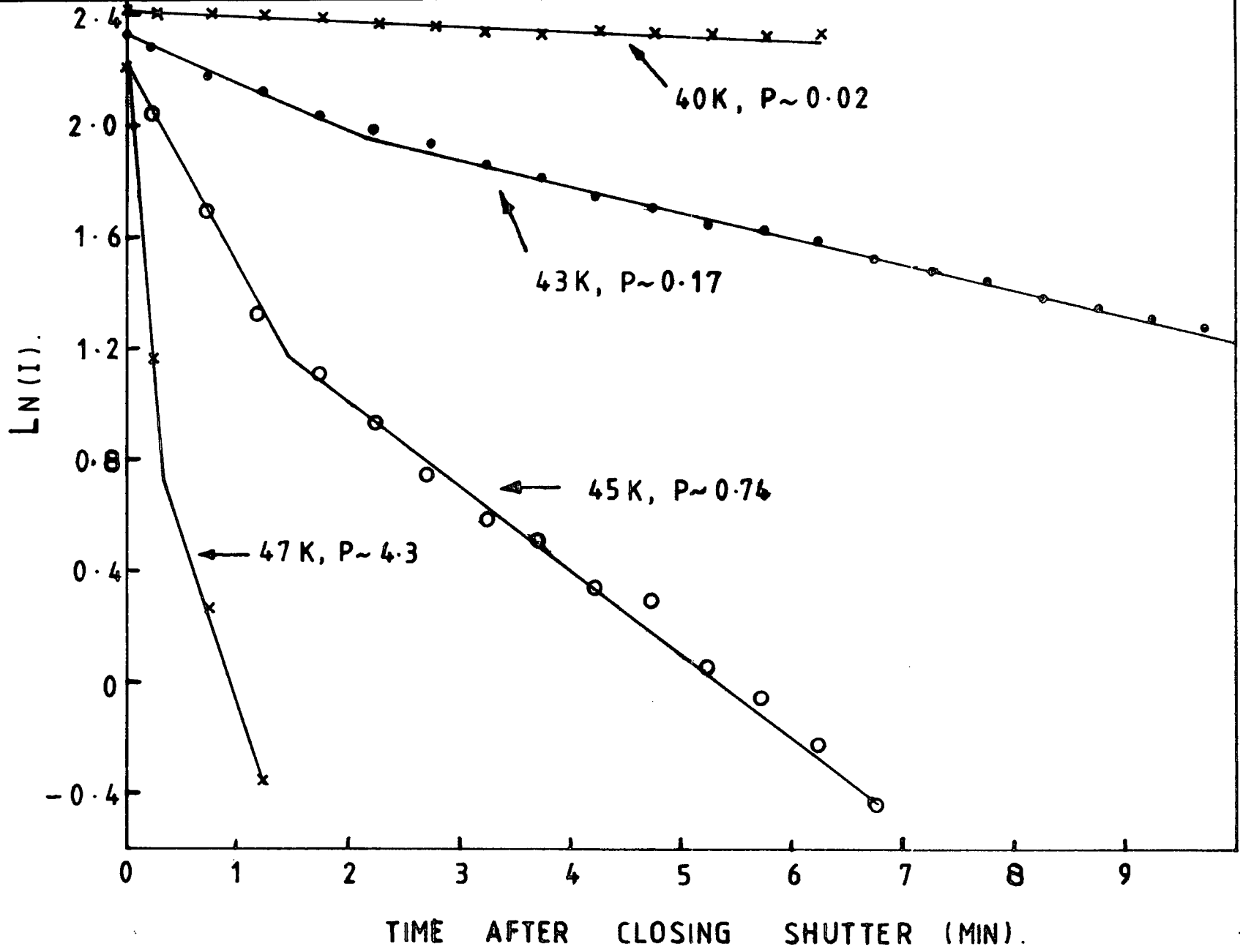

FIG. 6·21 VARIATION OF LN(I) OF SIGNAL H WITH TIME FOLLOWING u.v. IRRADIATION ; Ni/TiO_2 (N.L.).

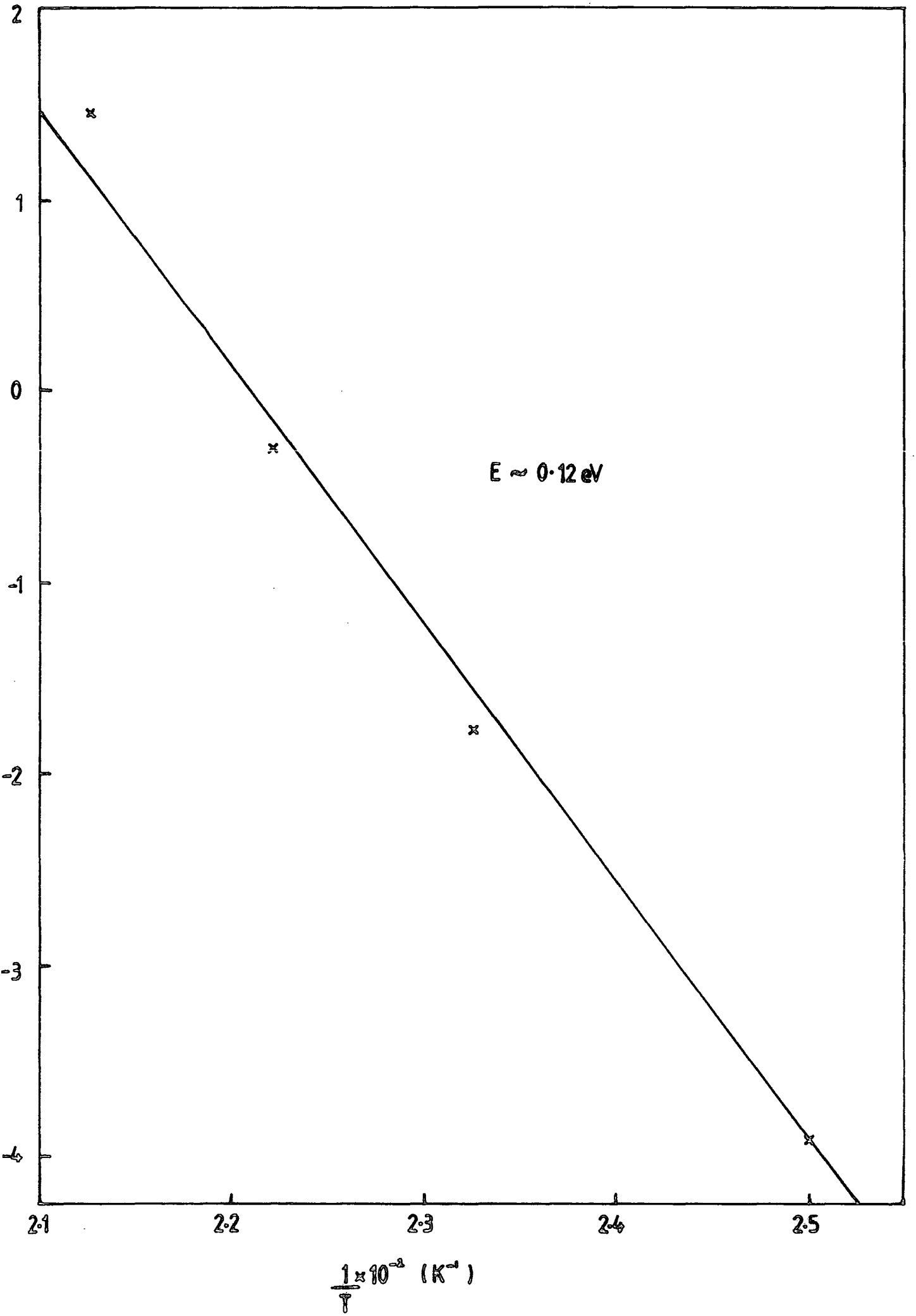

FIG 6.22 VARIATION OF $\ln(R)$ WITH $\frac{1}{T}$ FOR SIGNAL H N'/Ti O (N.L.)

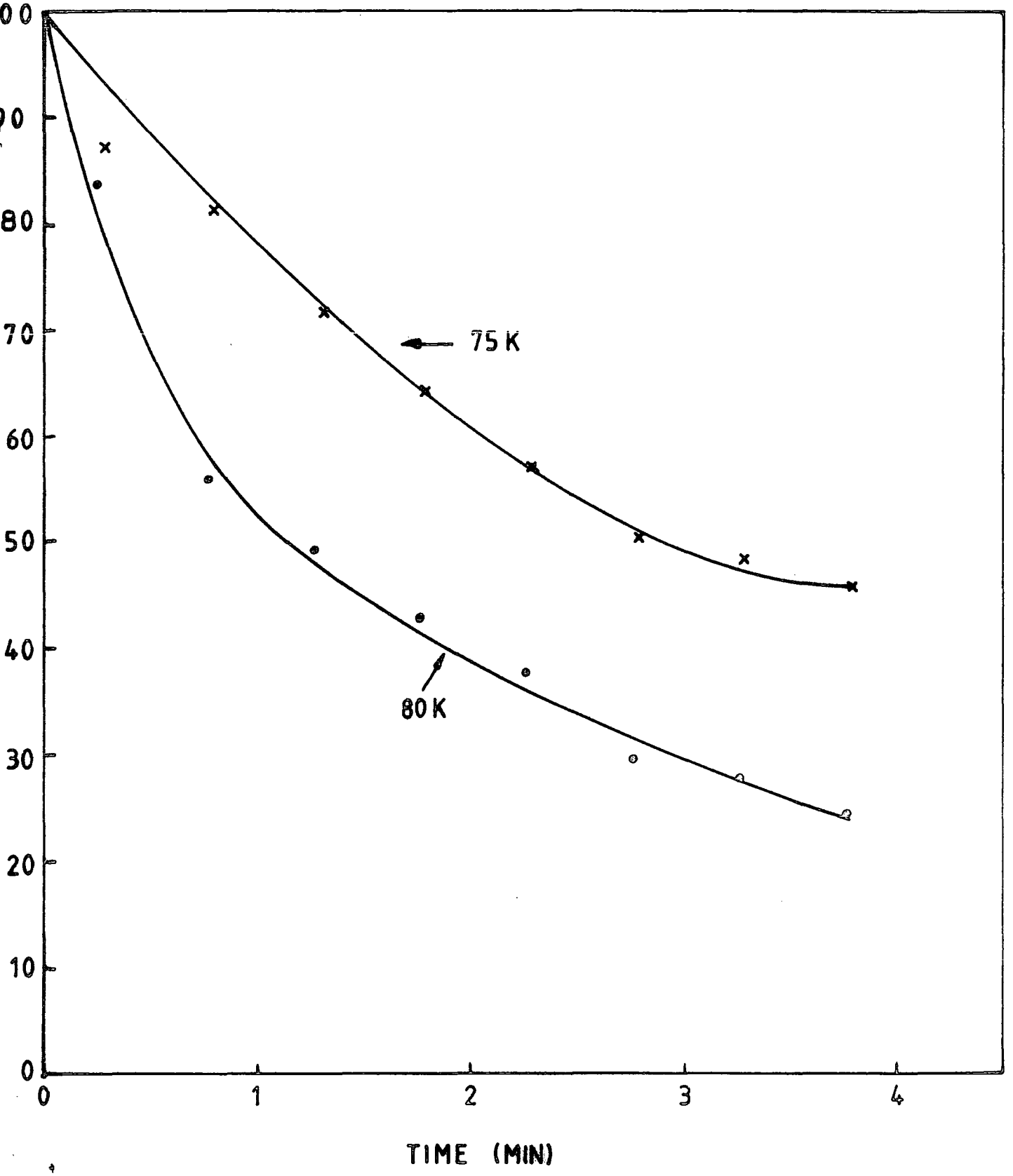

FIG. 6·23 ISOTHERMAL DECAY OF SIGNAL G FOLLOWING u.v. IRRADIATION ; Ni/TiO_2 (N.L.).

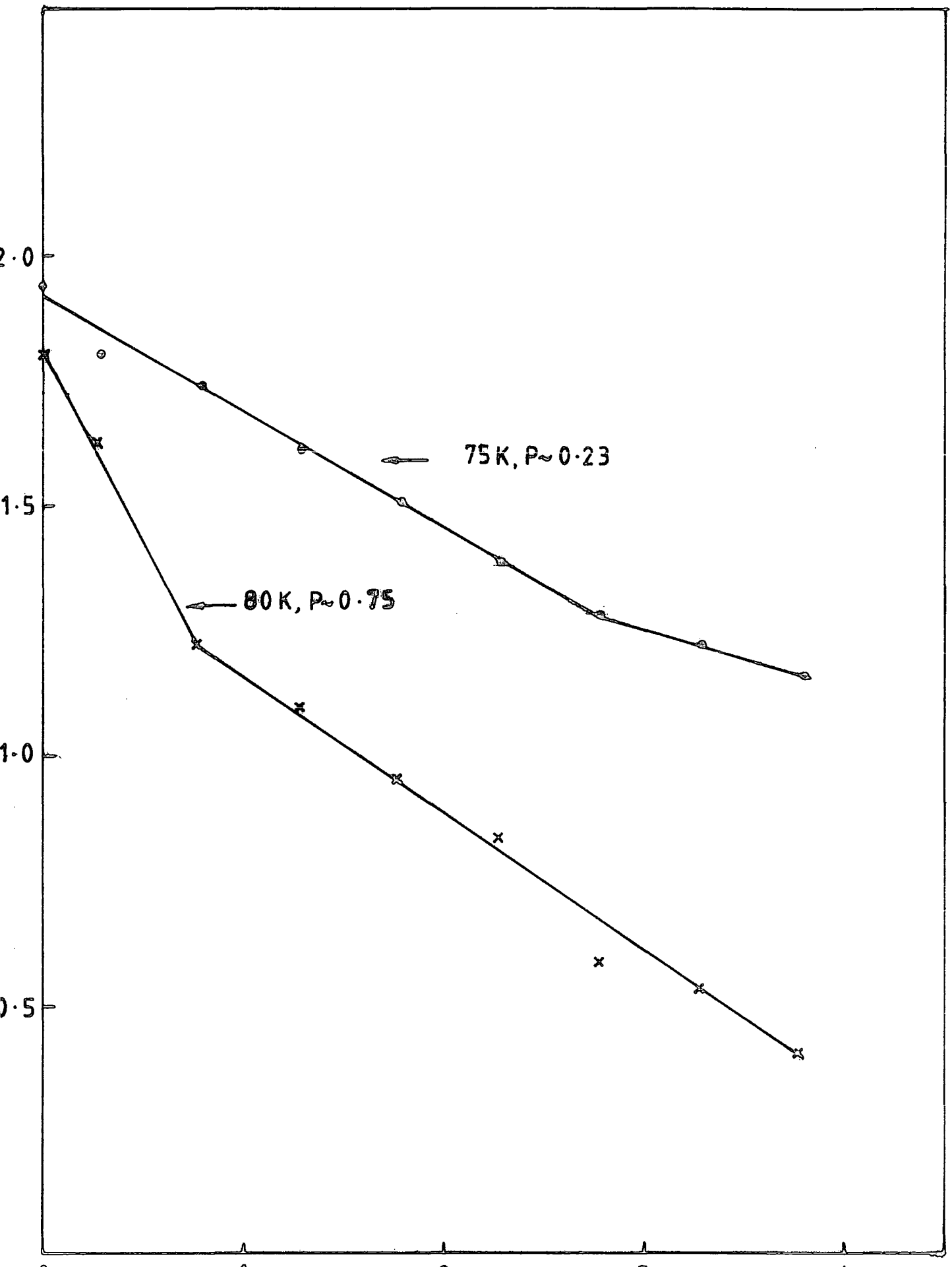

FIG.6·24 VARIATION OF LN(I) WITH TIME SIGNAL G;

Ni/TiO (N.I.)

Although no direct measurement of the isothermal decay of 'B' centres could be made, it was still possible to detect the thermal release of electrons from these traps into the conduction band, by monitoring their subsequent recombination at Ni^{3+} sites. Hence Fig. 6.25 illustrates the change of recombination rate with temperature by showing the decay of Ni^{3+} amplitude after u.v.irradiation at temperatures between 100 and 110 K. The initial isothermal reaction rates may be directly related to attempt-to-escape probabilities of electrons trapped at 'B' centres (Fig. 6.26), assuming that charge from other traps is not being released in significant amounts in this temperature range. Variation of probability, P, with temperature leads (Fig. 6.27) to a trap depth of $\sim$ 0.22 eV for B centres.

A similar approach was used to estimate the activation energy of the shallow hole traps, whose presence was deduced from the post irradiation increase of signal A (Fig. 6.13), at low temperatures, by measuring variations in the rate of this increase with temperature, Fig. 6.28, representing the change in rates at which holes were released following initial capture during irradiation. The corresponding escape probabilities of the shallow trap are derived from Fig. 6.29 and their variation with temperature (Fig. 6.30) places the hole trap $\sim$ 0.075 eV above the valence band.

Many of the thermally induced intensity changes examined by the isothermal decay technique appear to occur at slightly lower temperatures than those initially suggested by isochronal annealing measurements. This may be due to the fact that the crystal was cut after the isochronal annealing experiments in order to allow isofrequency measurements to be made in both the (001) and (110) planes, so that the sample subsequently used in isothermal decay measurements had a smaller thermal mass. It is therefore thought that the lower thermal recovery temperatures indicated by the isothermal decay technique are the more reliable.

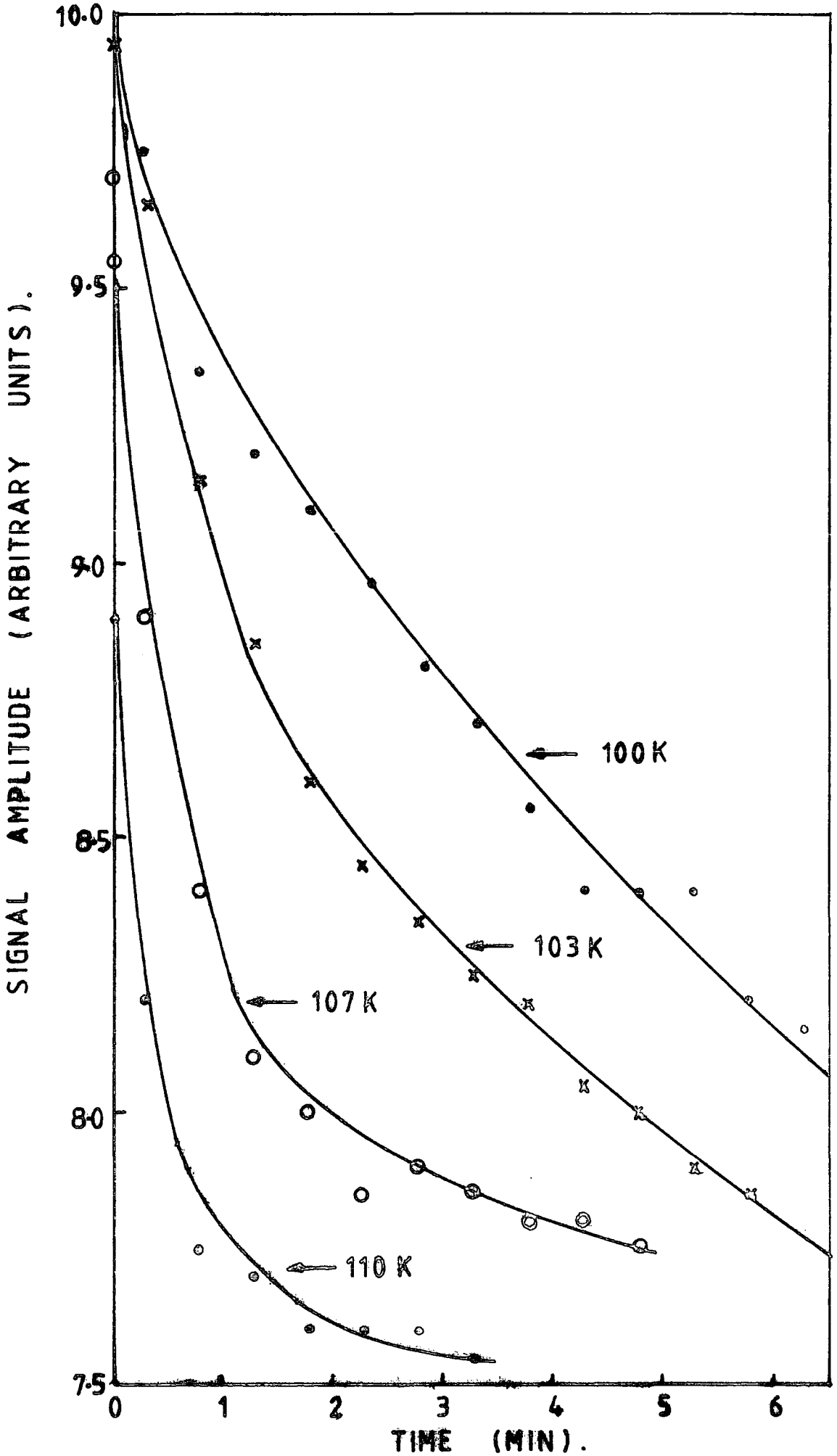

FIG.6·25 ISOTHERMAL DECAY OF Ni^{3+} AFTER u.v. IRRADIATION 100K - 110K TEMPERATURE RANGE. Ni/TiO_2 (N.L.).

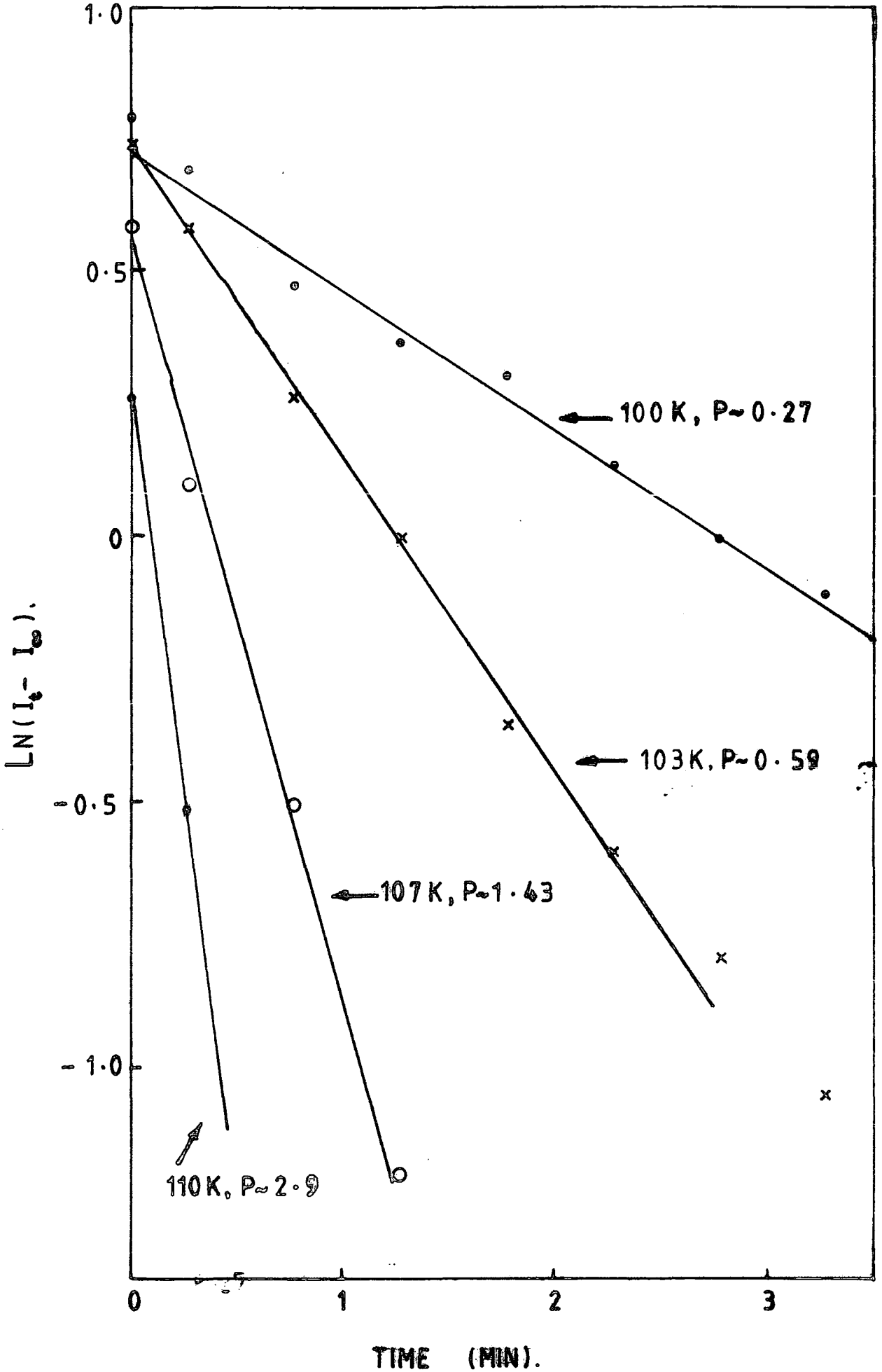

FIG.6·26 VARIATION OF Ni^{*} AMPLITUDE WITH TIME AFTER u.v. IRRADIATION; Ni/TiO_2 (N.L.).

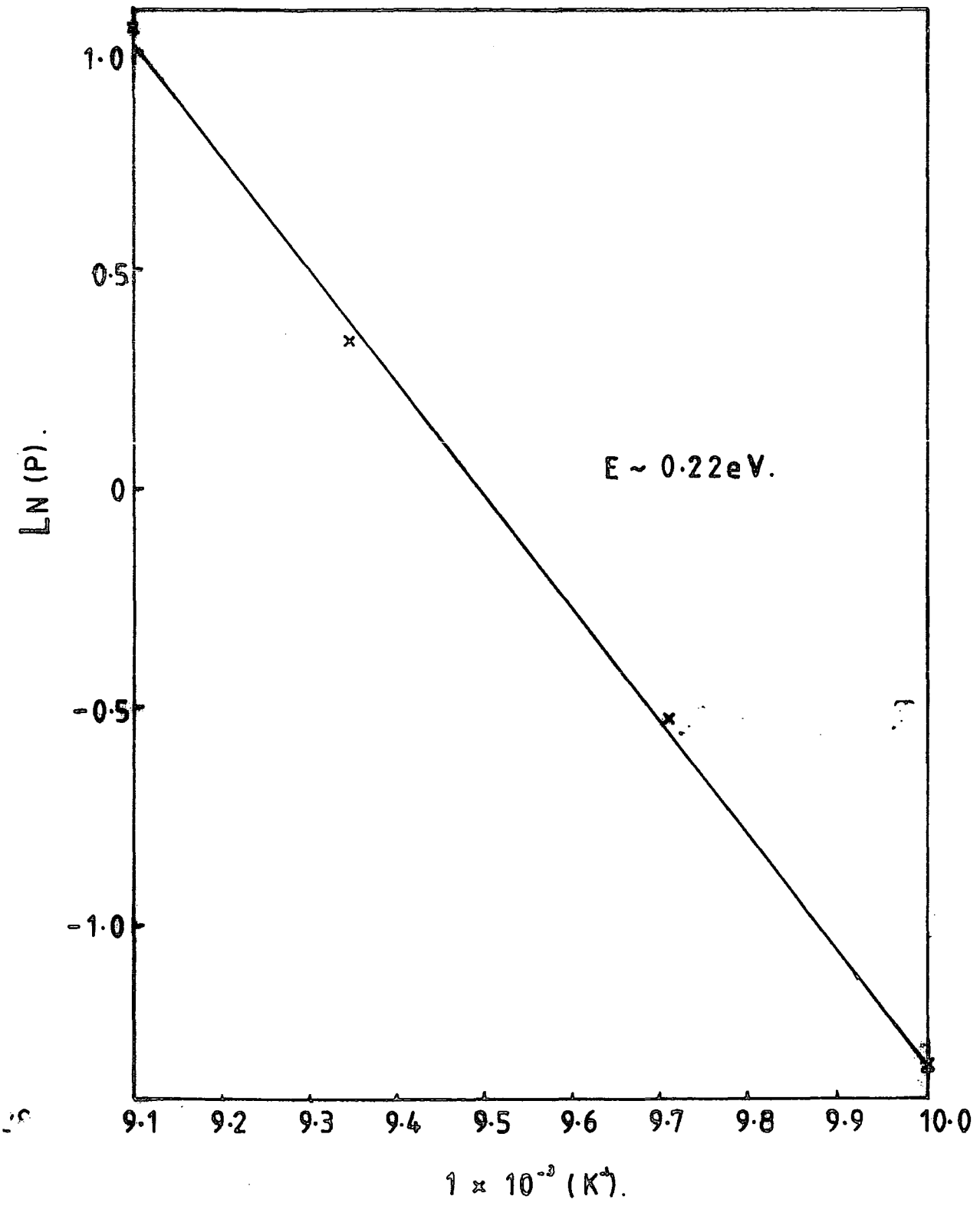

FIG.6·27 VARIATION OF P WITH TEMPERATURE; FOR B CENTRES IN Ni/TiO_2 (N.L.).

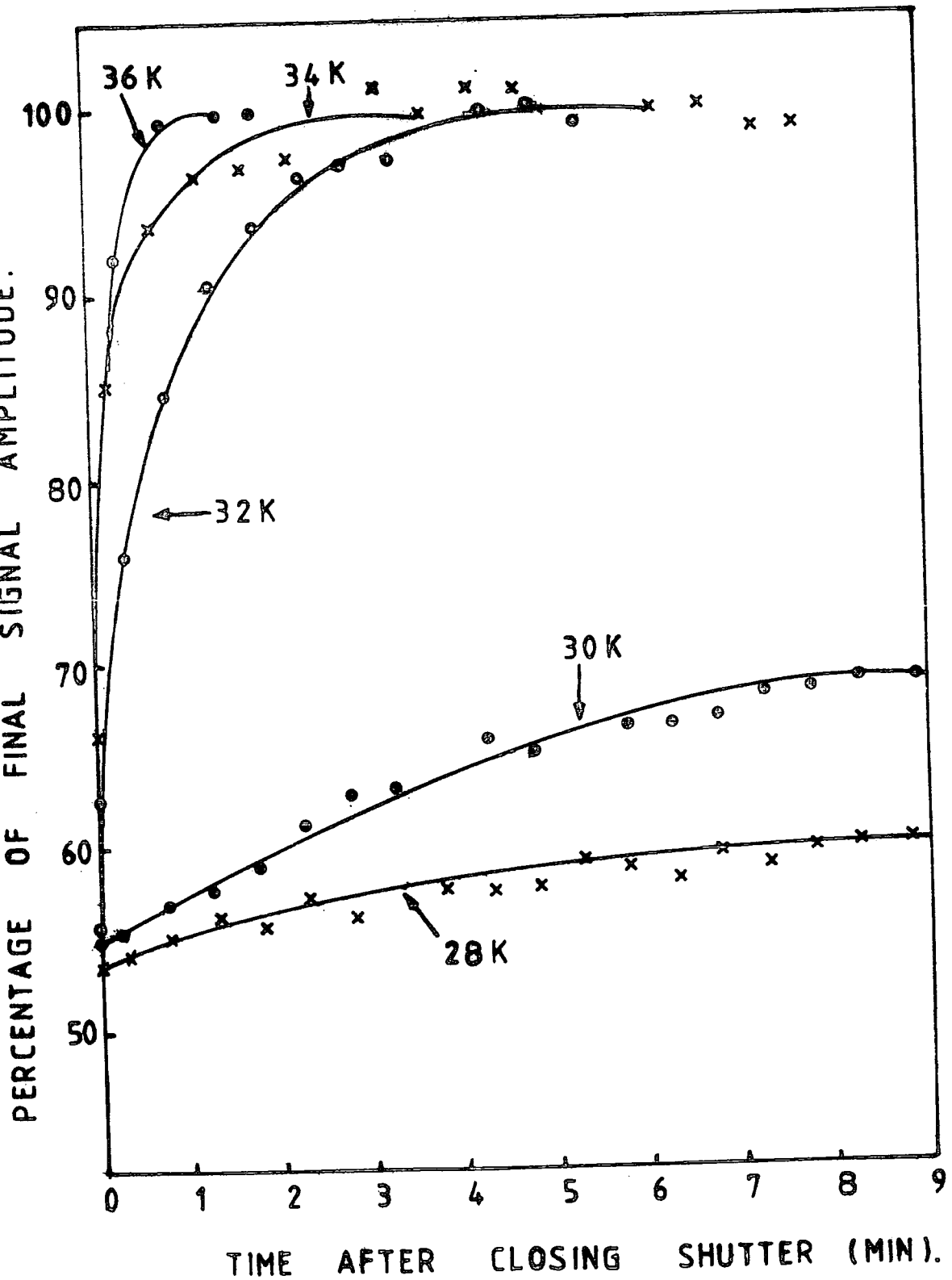

FIG. 6·28 ISOTHERMAL INCREASE IN AMPLITUDE OF SIGNAL A AFTER u.v. IRRADIATION, REPRESENTING THE RECAPTURE OF CHARGE RELEASED BY A SHALLOW HOLE TRAP; Ni/TiO_2 (N.L.).

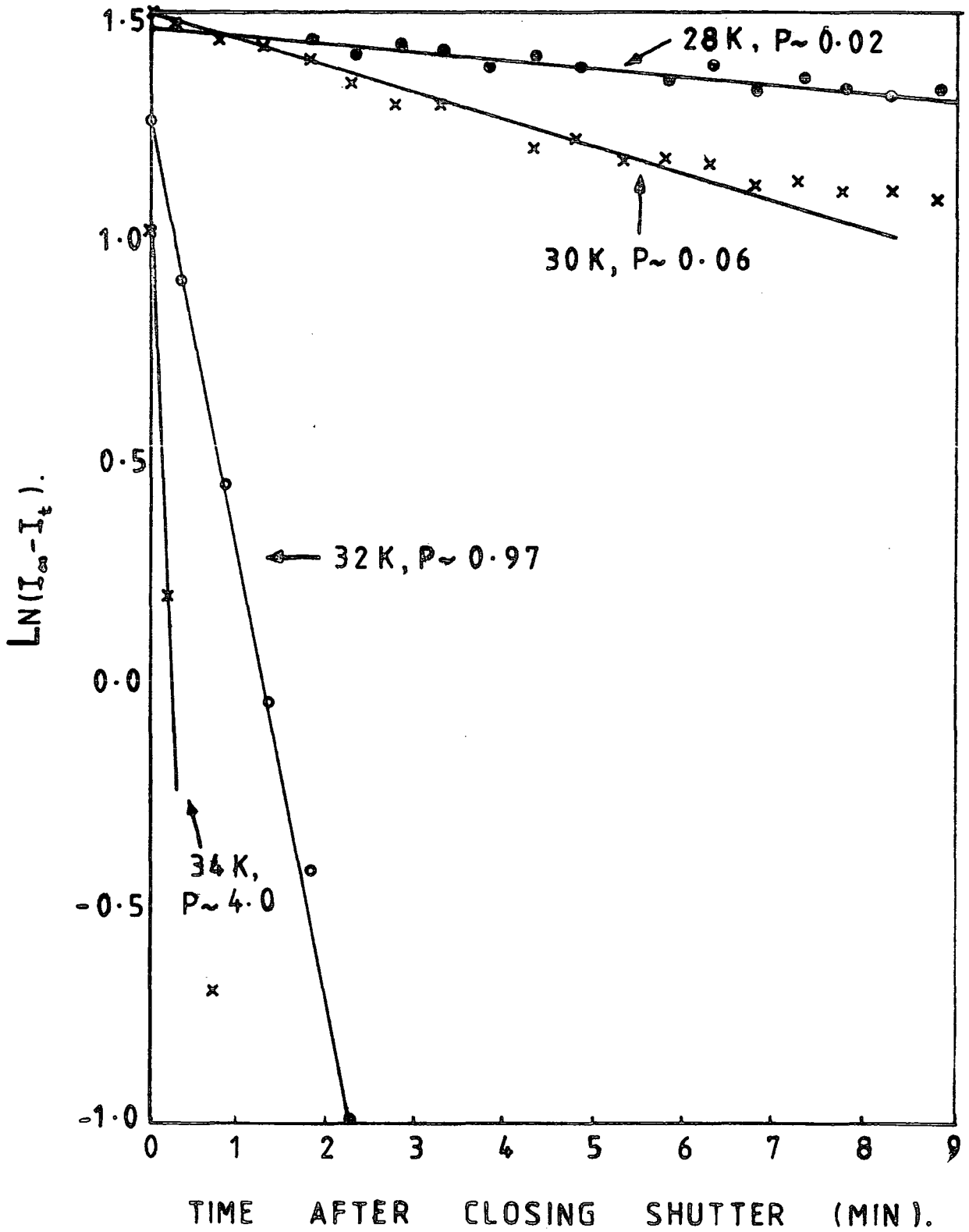

IG.6·29 $LN(I_\infty - I_t)$ vst; SIGNAL A FOLLOWING u.v. IRRADIATION AT TEMPERATURES IN THE RANGE OF 28K-34K; Ni/TiO_2 (N.L.).

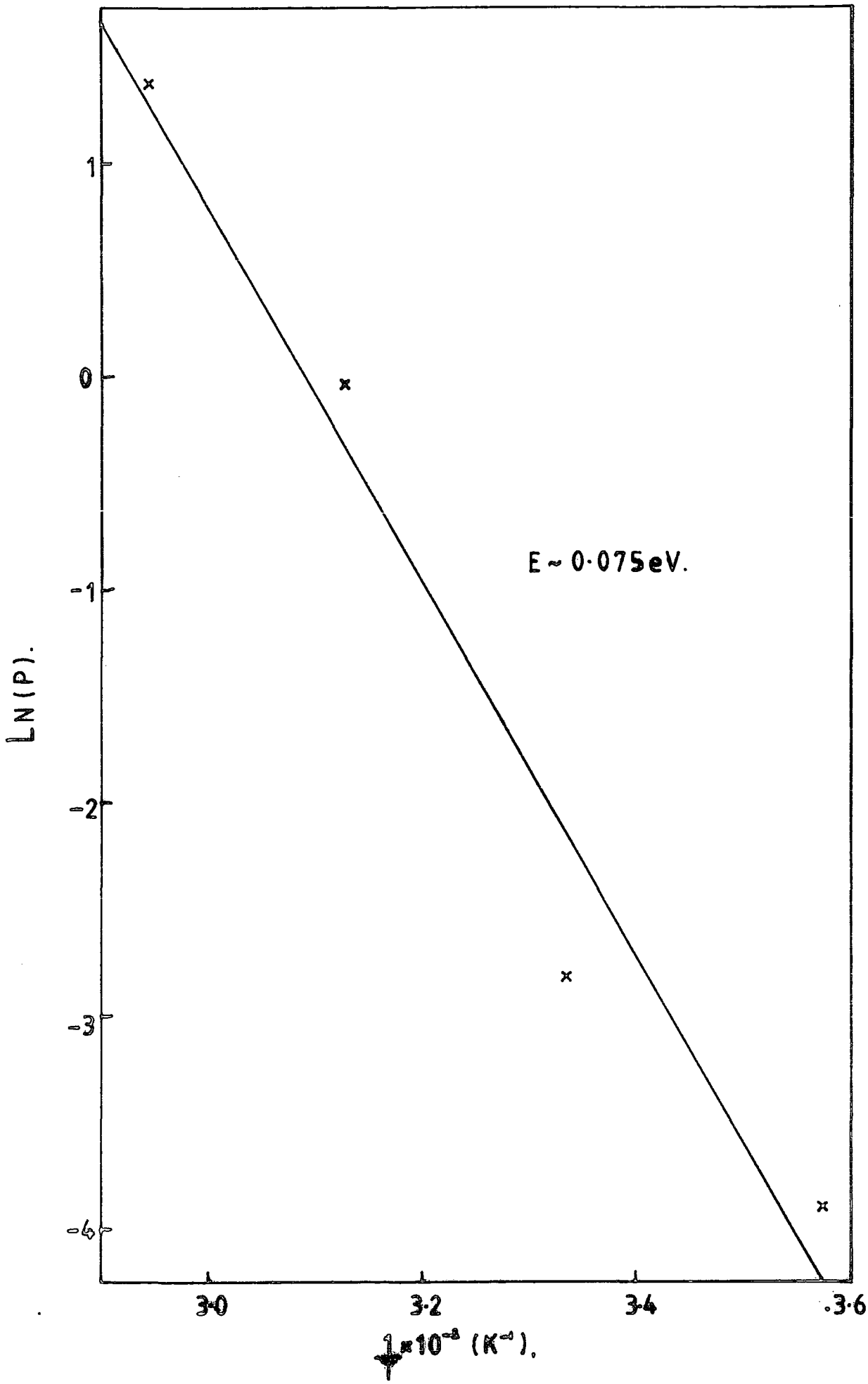

FIG.6·30 VARIATION OF P WITH TEMPERATURE TO GIVE ACTIVATION ENERGY OF SHALLOW HOLE TRAP; Ni/TiO_2 (N.L.).

6.8 INFRA-RED IONIZATION

An alternative to the thermal release of trapped charge by isochronal annealing, is to use direct optical ionization by incident radiation of energy equal to or greater than the trap depth, which, for most of the traps considered so far, means the infra-red region of the spectrum. This section summarizes a preliminary investigation into the effect of I.R. radiation on the spectra previously formed by u.v. irradiation.

Initially the effect of the infra-red component of the Hg lamp output was studied by placing a Cu SO_4 solution filter, which absorbs infra-red radiation, between the lamp and the sample during irradiation. Fig. 6.31 depicts the variation of amplitude of signal 'A', during and after irradiation, with and without the filter. The signal amplitude, and hence the number of filled traps (A centres) is clearly greater when the infra-red component is removed from the incident radiation, suggesting that without the filter an equilibrium condition is reached in which u.v. trap-filling is opposed by I.R. trap-emptying which therefore limits the total amount of trapped charge. The effect of inserting the I.R. filter during irradiation on the other u.v. induced spectra (B-H) however, was much smaller, with the removal of the I.R. component causing increases in intensity of only $\sim$ 5% for most spectra and having no detectable effect at all on the amplitude of signal B. Such variations are thought to reflect differences in the photon capture cross-sections of the trapping centres.

In order to study infra-red ionization of trapped charge after u.v. irradiation at 40 K, a 250 Watt Tungsten lamp, together with a Si filter which absorbed radiation of energy greater than 1.1 eV, was used as an infra-red source. The decay of the intensities of e.s.r. spectra with time of I.R.ir-radiation is shown in Fig. 6.32. Fig 6.33 shows that these decays have two exponential components, probably correspondng to initial monomolecular and subsequent bimolecular kinetics. The bimolecular decay time constants of the

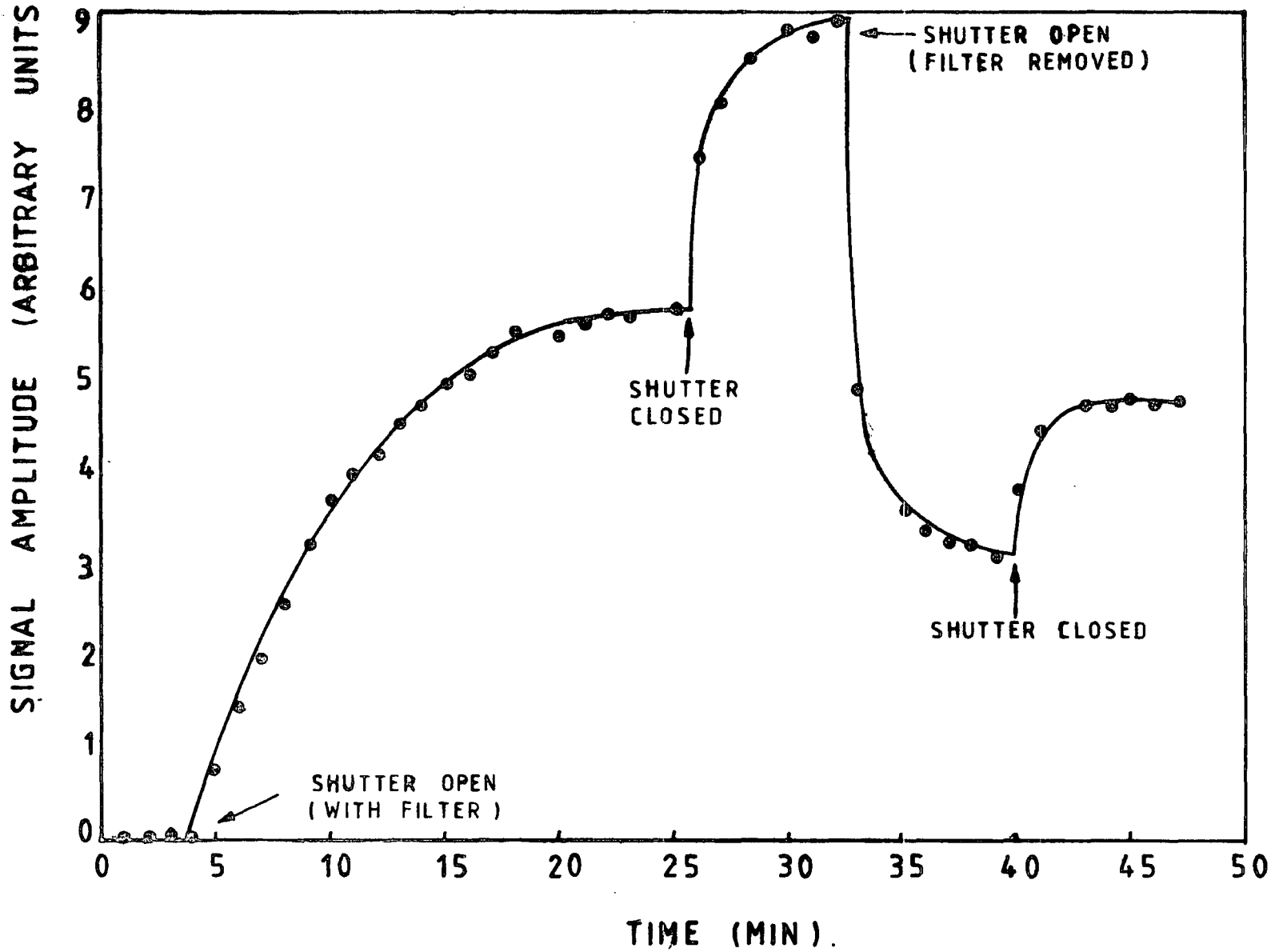

FIG.6·31 VARIATION OF SIGNAL AMPLITUDE CENTRE A, DURING AND AFTER u.v. IRRADIATION AT 40K, WITH AND WITHOUT A $CuSO_4$ SOLUTION FILTER.

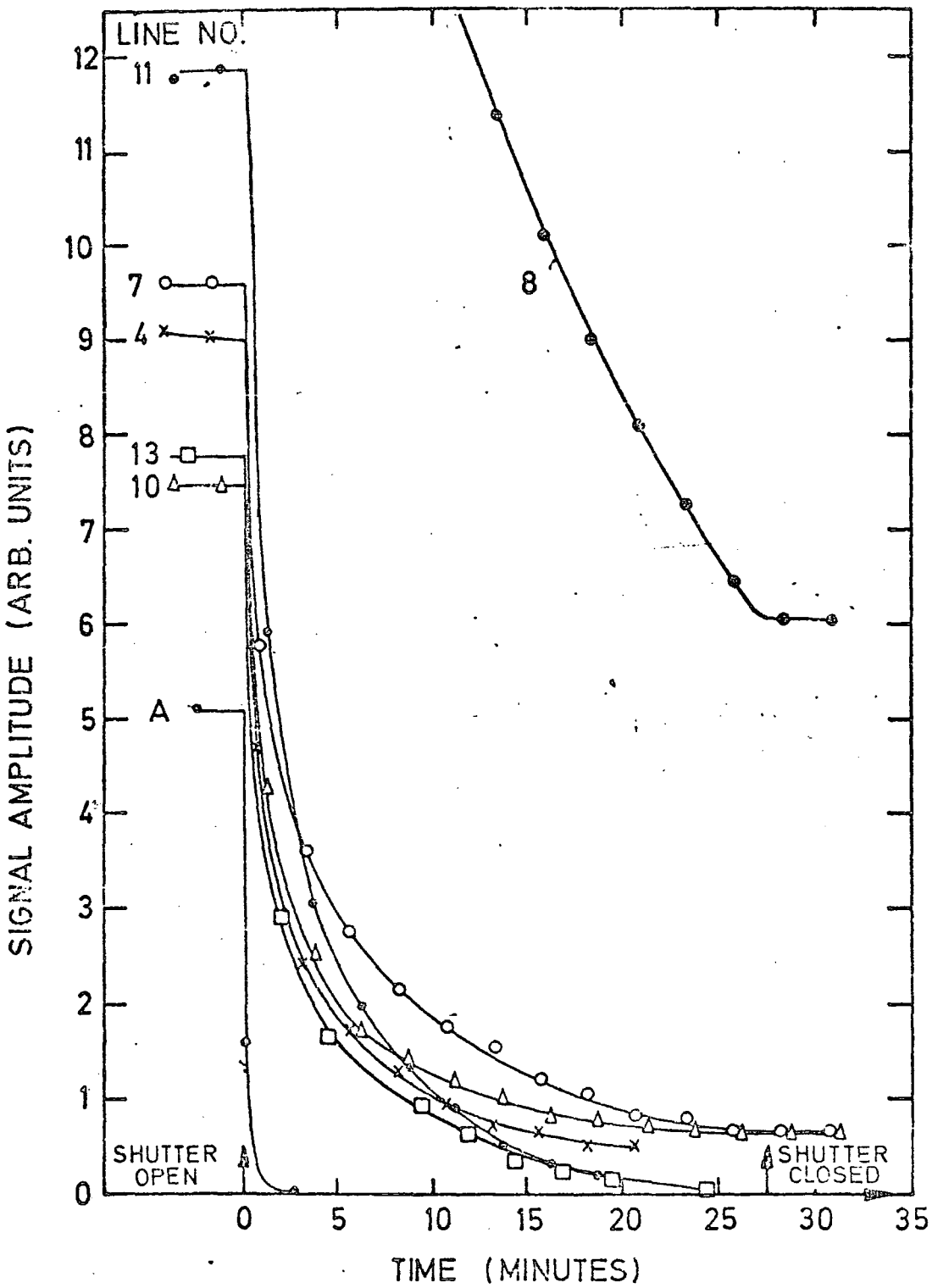

FIG 632 DECAY OF SIGNAL AMPLITUDE OF SPECTRA (FORMED BY U.V. AT 40K) UNDER INFRA-RED IRRADIATION OF ENERGY $< 9 \times 10^3$ CM^{-1}.

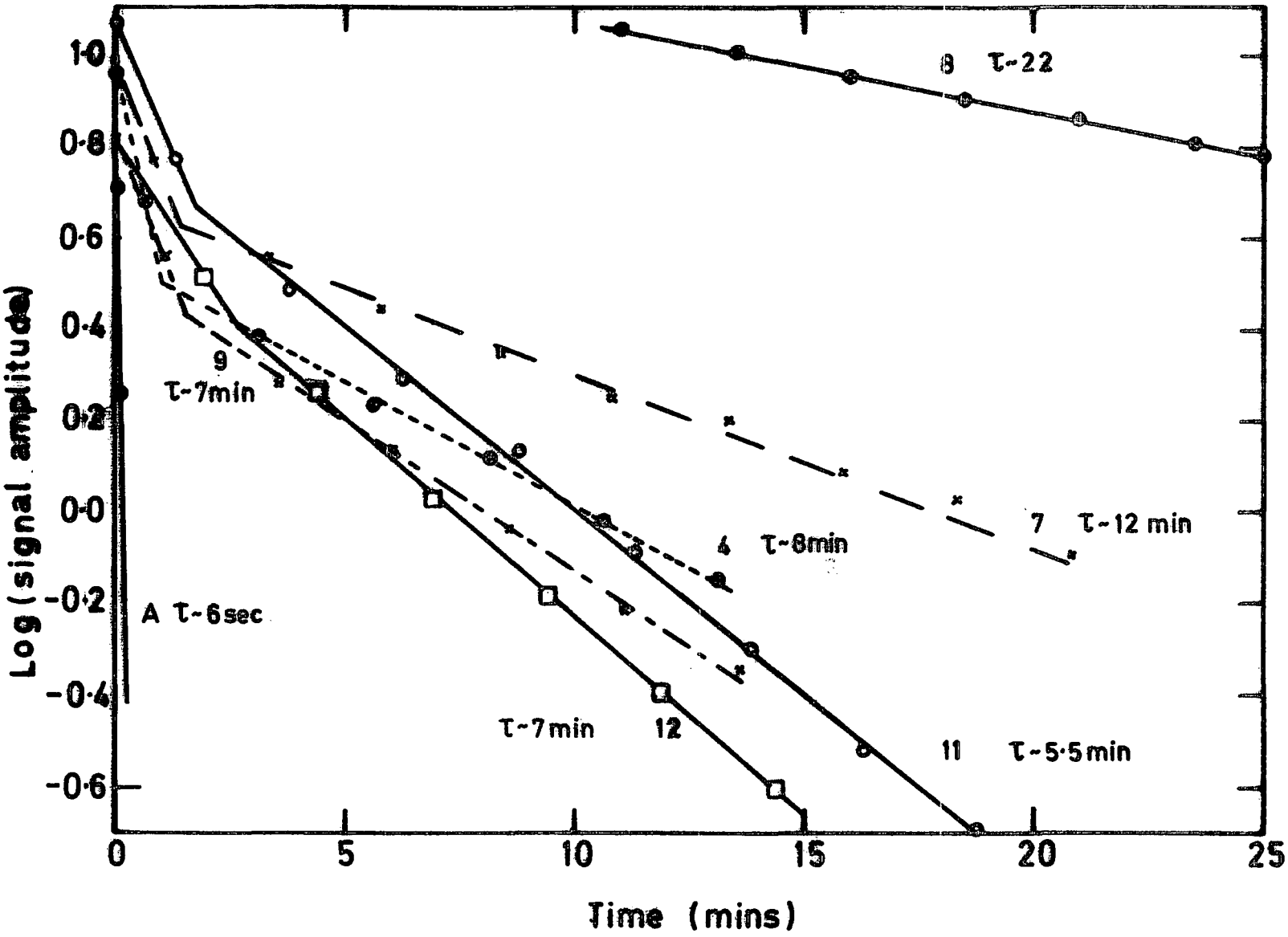

FIG. 6.33 Decay of amplitude of u.v. - induced spectra during infra-red irradiation of energy $< 9 \times 10^3$ cm^{-1}, Ni/TiO$_2$(NL)

shallow electron traps, centres C-H, are fairly similar, ranging from 5 to 12 minutes, but that of the deeper electron trap, centre B (line 8) is significantly longer and centre A has a time constant $\sim$ 2 orders of magnitude lower. The relative magnitudes of these decay time constants may be related to the relative magnitudes of the photon capture cross-sections of the traps. Thus centre 'A' has the highest capture cross-section and centre 'B' has the lowest, in agreement with the initial measurements with the I.R. filter.

In addition to the above effects, 25 minutes of infra-red irradiation completely restored the Fe^{3+} concentration to the pre-u.v. irradiation level, but Ni^{3+}, Ni^{2+}, Mn^{4+} and Mn^{3+} concentrations were intermediate between pre- and post-u.v. values. This suggests that Fe^{4+} and 'A' centres are shallow enough hole traps to be optically ionized by radiation of energy less than 1.1 eV, but that the Ni and Mn recombination centres are situated nearer the centre of the band gap.

6.9 AS-RECEIVED N.L. TiO_2

The results reported in sections 6.3 to 6.8 were all carried out with the Ni-doped National Lead crystal, sample 4 . This section presents further results from an undoped sample cut from the same boule. E.s.r. spectra representing Fe^{3+}, Cr^{3+} and Ni^{3+}, together with the much weaker spectrum I, were recorded in the'as-received' National Lead crystal, which was also nominally doped with 1000 p.p.m. of Aluminium.

In order to carry out comparable measurements to those performed with the Ni and Mn-doped crystal, described in Sections 6.3 to 6.7, the sample was cooled to 40 K and subjected to u.v. irradiation from a Hg lamp. In this case, however, irradiation had the effect of completely damping the microwave cavity, presumably by causing excessive photoconductivity in the rutile crystal, so that no quantitative measurements of u.v. induced changes in spectral intensity were possible at this temperature. Moreover, the cavity damping persisted even after irradiation had ceased and the original cavity Q could only be restored

by heating the sample to about 70 K. Raising the temperature of irradiation above 40 K had the effect of causing a decrease in the degree of damping and a corresponding decrease in the time needed for the cavity to recover its initial Q after irradiation, until at 120 K there was negligible damping induced by irradiation.

Due to this damping problem, the lowest temperature at which isochronal annealing measurements could be made was 80 K, so that some of shallow traps found in the Ni-TiO_2 (N.L.) crystal, if present in this sample, could not be detected by this technique. After cooling to 80 K in the dark and recording the Fe^{3+} and Ni^{3+} spectra, the sample was subjected to 10 minutes u.v. irradiation. Time was then allowed for the initial cavity Q to be restored and the spectra were re-recorded. It was found that Fe^{3+} concentration was reduced to $\sim$ 15% of the pre-u.v. level, Ni^{3+} concentration increased by $\sim$ 35% and two new spectra appeared. One was easily identified as corresponding to the 'A' centre, previously found in the Ni-doped N.L. crystal. The other spectrum, labelled 'X', had substitutional symmetry and was described by the following parameters : $g_{001} = 1.9355$, $g_{110} = 1.9137$ and $g_{1\bar{1}0} = 1.9653$. An isofrequency plot of this spectrum in the (110) plane is given in Fig. 6.34. No other new spectra of significant intensity were observed.

Isochronal annealing measurements between 80 and 265 K were performed with lines from the Fe^{3+}, Ni^{3+}, A and X spectra and the results are summarized in Fig. 6.35. The Fe^{3+} and 'A' centre profiles are broadly in agreement with those in the Ni-TiO_2 (N.L.) crystal, though the features are less sharp in this case. The Fe^{3+} concentration is gradually restored by successive anneals until its pre-u.v. level is reached after heating to $\sim$ 220 K. The 'A' centre concentration falls sharply between 100 and 120 K and then gradually decreases with increasing temperature, reaching zero at $\sim$ 180 K.

The amplitude-temperature profiles of Ni^{3+} and 'X' are both similar to that of 'A' at temperatures up to $\sim$ 180 K , except that both Ni^{3+} and 'X'

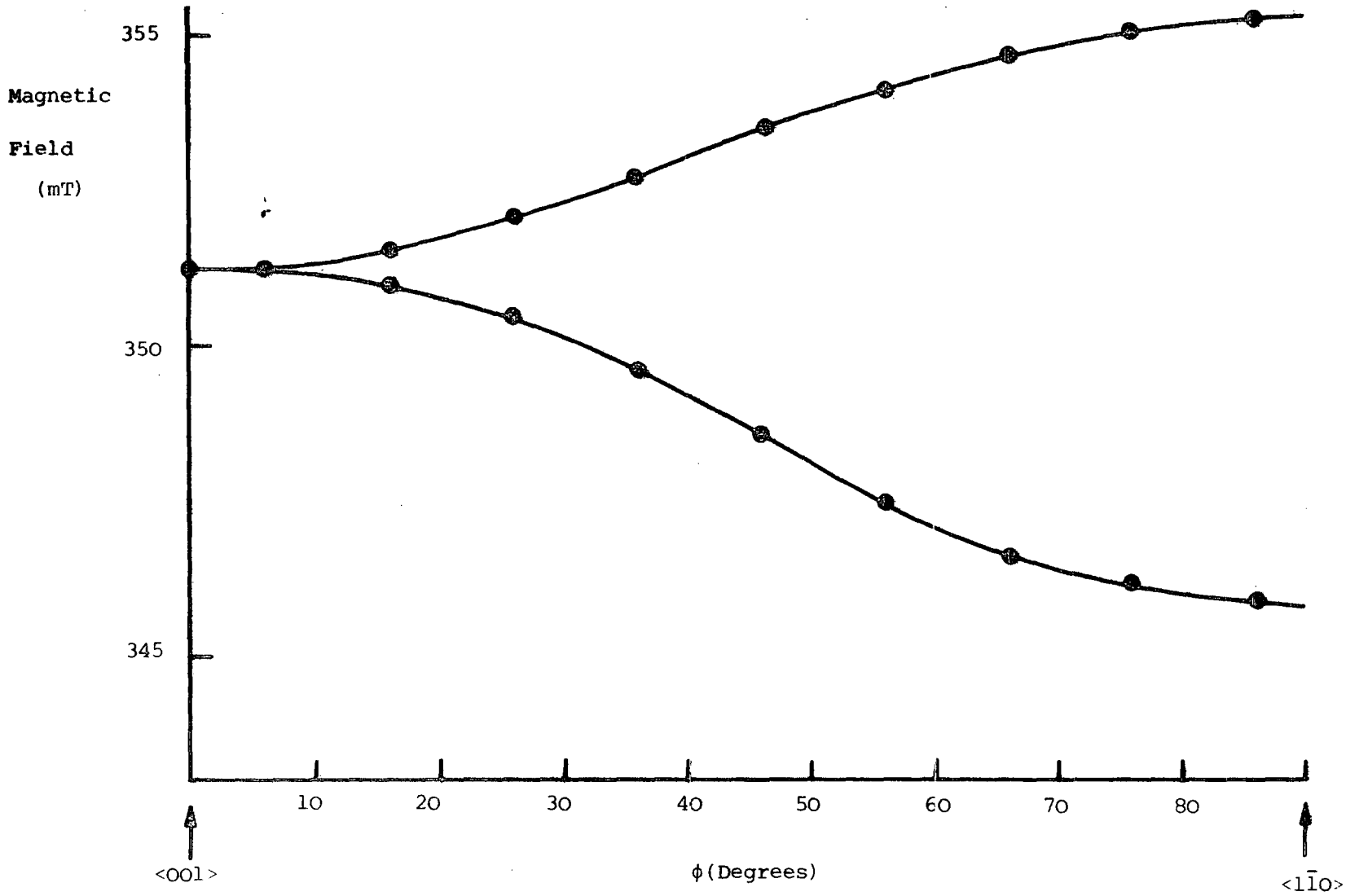

Figure 6.34 : Isofrequency diagram of spectrum 'X' in the (110) plane, ν = 9.5135 GHz ; TiO_2 (N.L.)

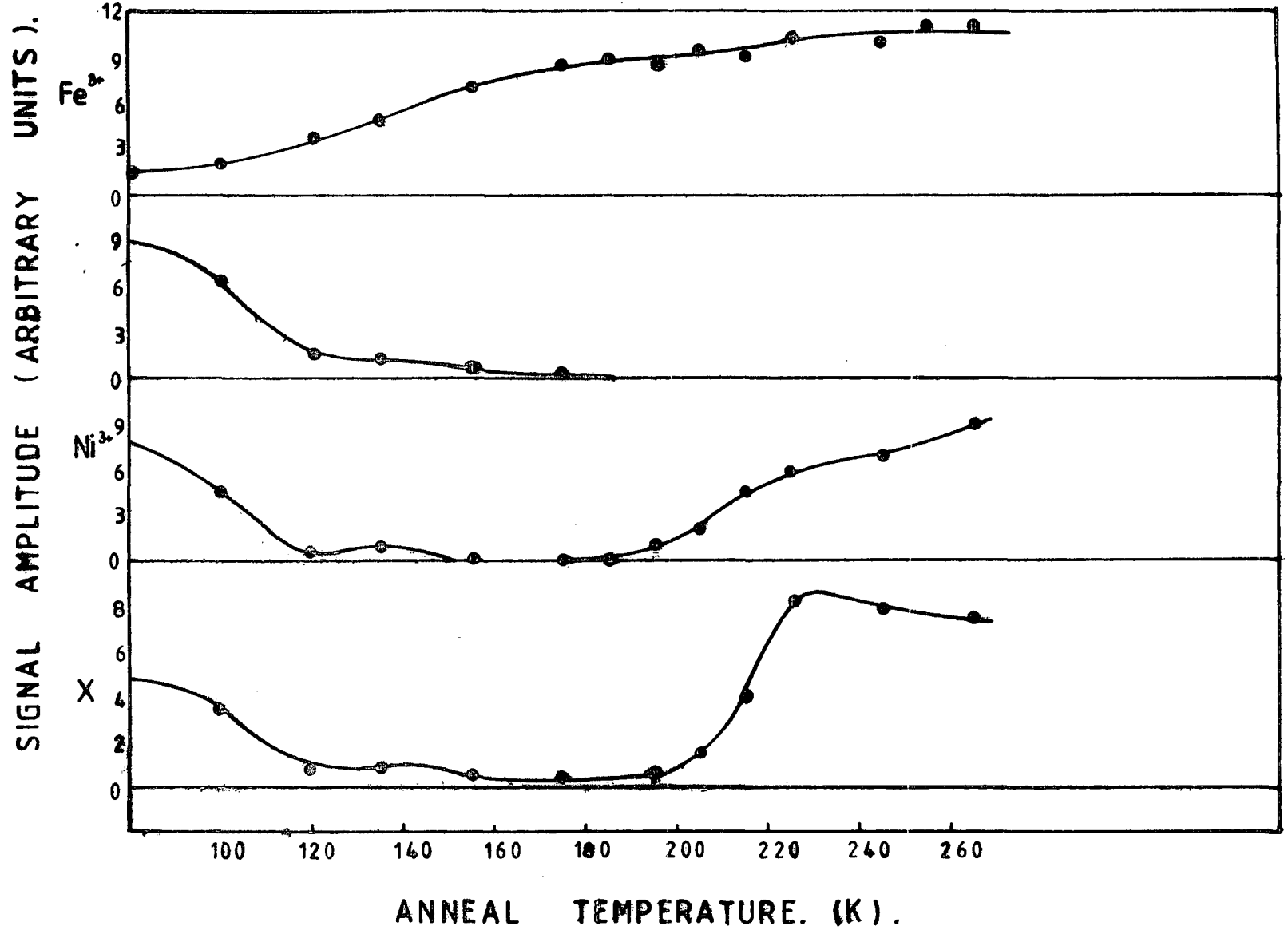

FIG.6·35 ISOCHRONAL ANNEALING OF Fe^{3+}, Ni^{3+}, A, X, SPECTRA, FOLLOWING u.v. IRRADIATION AT 80K; AS RECEIVED TiO_2 (N.L.).

profiles have a small shoulder at ∿ 140 K. This suggests that, like centre 'A', both Ni^{3+} and 'X' are acting as hole traps, so that the decrease in concentration by heating from 100 to 120 K is caused by the recombination of electrons thermally freed from shallow traps such as those found in Ni-TiO_2 (N.L.), whose presence however could not be detected at 80 K in the 'as-received' N.L. crystal since their resonance lines would be broadened. The shoulders at ∿ 140 K again suggest the presence of a shallow hole trap which is thermally ionized at this temperature. Unlike centre A, the concentrations of both Ni^{3+} and 'X' increase with annealing at temperatures above 180 K. There is a fairly sharp increase up to 220 K, above which the Ni^{3+} concentration increases at a slower rate while the concentration of centre 'X', gradually decreases. The fact that the Ni^{3+} and 'X' spectra have such similar amplitude-temperature profiles in the 180 to 220 K temperature range suggests that both are responding to the same event, the most likely explanation being the thermal reconnection of a hole trap (e.g. Fe^{4+}) with the valence band and the subsequent stabilization of freed holes at these defects to give 'X' and Ni^{3+} centres. The behaviour at higher temperatures may then be due to Ni^{2+} levels coming into thermal equilibrium with the conduction band, causing an excess of free electrons which then recombine via 'X' centres, or conversely the 'X' centre may become thermally connected with the valence band with the freed holes being subsequently retrapped at Ni^{2+} sites, causing an increase in Ni^{3+} concentration.

Isothermal recovery measurements could only be performed with the Ni^{3+} spectrum, since lines from 'X' and 'A' spectra rapidly broadened at temperatures above ∿ 100 K and the features of the Fe^{3+} isochronal annealing profile were too soft to yield useful quantitative measurements. The amplitude of a Ni^{3+} line was monitored before and after u.v. irradiation over a range of temperatures between 216 and 240 K. Fig. 6.36 illustrates the variation in the Ni^{3+} concentration thermal recovery rate with temperature of irradiation. Fig. 6.37, a

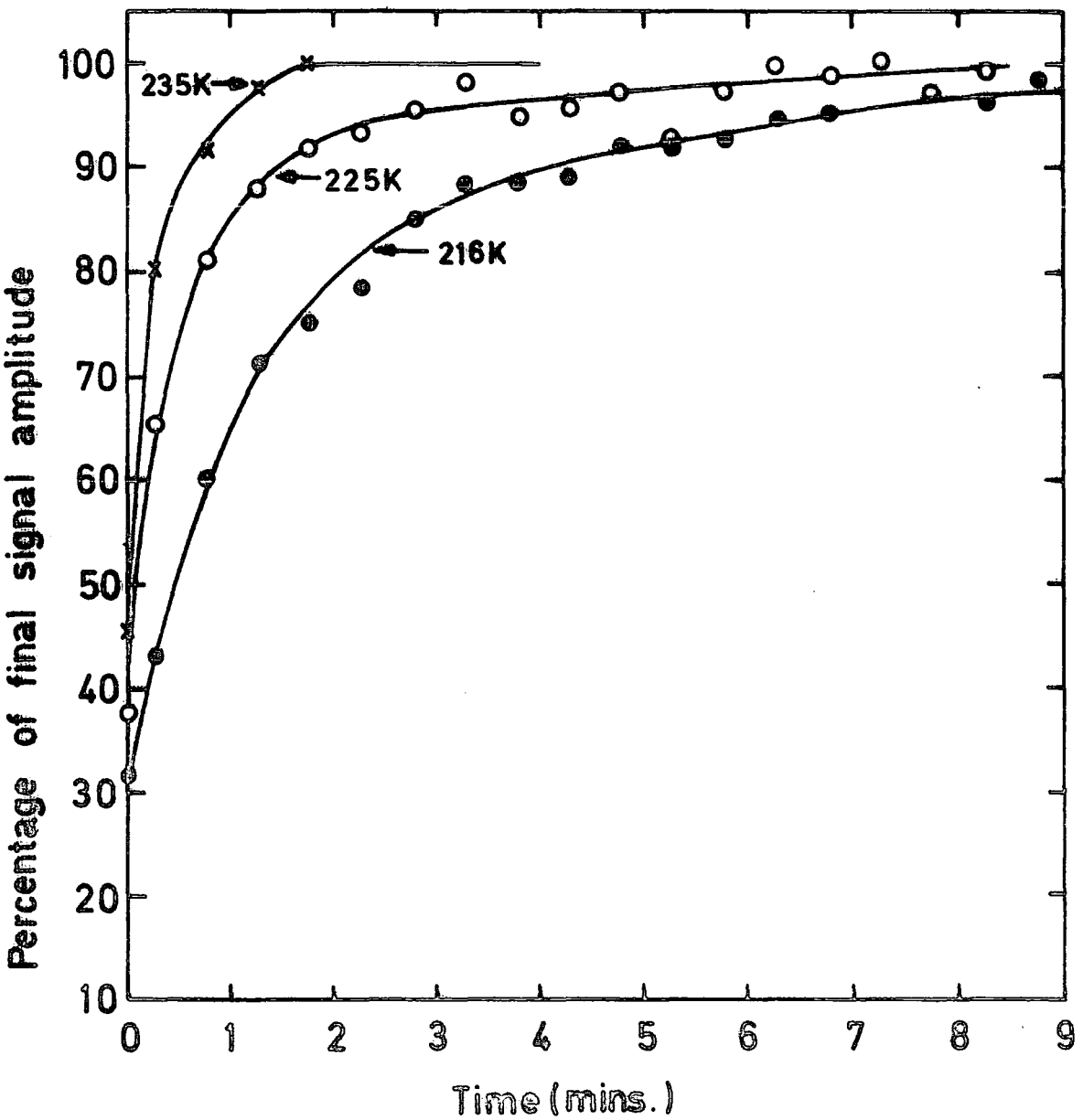

FIG.6-36 Isothermal recovery of Ni^{3+} signal following u.v. irradiation at temperatures between 216 and 235K; TiO_2(NL)

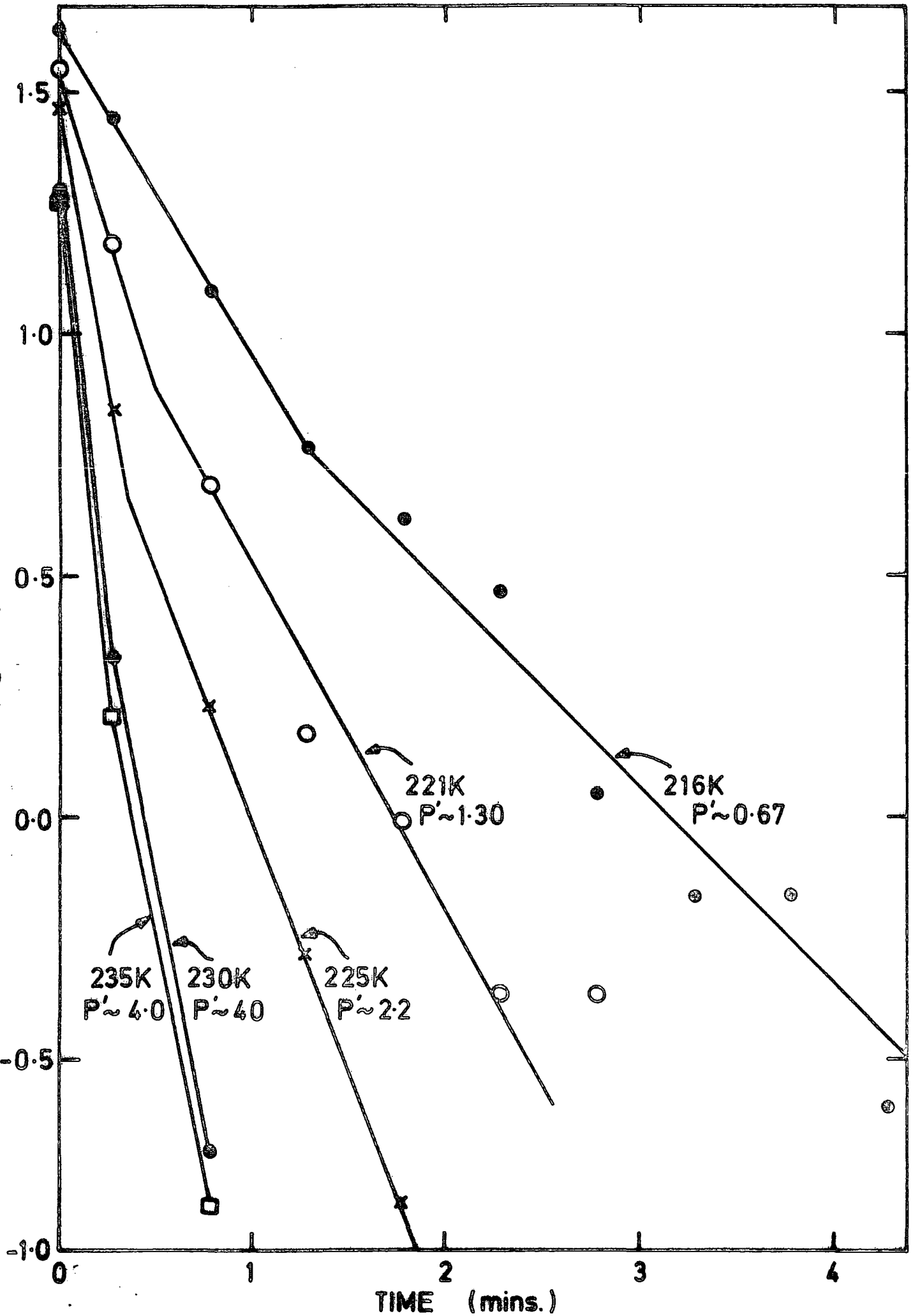

FIG.6-37 Variation of isothermal recovery rates of Ni^{3+} signal at different temperatures of irradiation, TiO_2 (NL)

plot of $\ell n\ (I_\infty - I_t)$ vs. time, where I_∞ is the final Ni^{3+} signal amplitude again suggests initial monomolecular and subsequent bimolecular kinetics, with the transition occurring when the Ni^{3+} concentration had reached ∿70% of its final value. Hence it is thought that fairly reliable values of P, the escape probability of the relevant trap can be evaluated from the initial decay slopes at 216, 221 and 225 K, but the values determined at 230 and 235 K may be less reliable if 2nd order kinetics had taken over before the 2nd point on the decay curve was recorded. The resulting plot of ℓn P vs. $^{1}/_{T}$, Fig.6.38, using only data derived from measurements at 216, 221, 225 and 230 K, gives a thermal activation energy for the trap of ∿ 0.55 eV.

6.10 PLASMA-GROWN CRYSTALS

Two crystals from plasma-grown boules were examined by e.s.r. techniques. One, B.S.16, had been grown in an oxidized state and doped with 1000 ppm Aluminium, and the other, B.S.10, was grown from nominally pure feed, but in a reducing atmosphere, hence requiring a subsequent oxidizing heat treatment.

A weak Fe^{3+} spectrum was detected in a relatively large sample from B.S.16 at room temperature, but no spectra at all of significant intensity could be found in the smaller sample needed for cryogenic work, even at liquid helium temperatures. As was found with the 'as-received' N.L. crystal, u.v. irradiation at 40 K had the effect of completely damping the cavity, again presumably due to causing excessive photoconductivity. This effect was reversed by heating to 100 K for several minutes. On recooling to 40 K, spectra corresponding to the 'A' and 'B' centres first found in Ni-TiO_2 (N.L.) had appeared. Both spectra were removed by annealing at 140 K for 10 minutes. The lack of any other spectra in this sample and the fact that both A and B defects anneal out at approximately the same temperature (electrons freed from 'B' centres re-combining via 'A' centres) suggest that A and B are the dominant defects in the stoichiometric plasma-grown boules, which were generally of higher purity than any of the other rutile crystals.

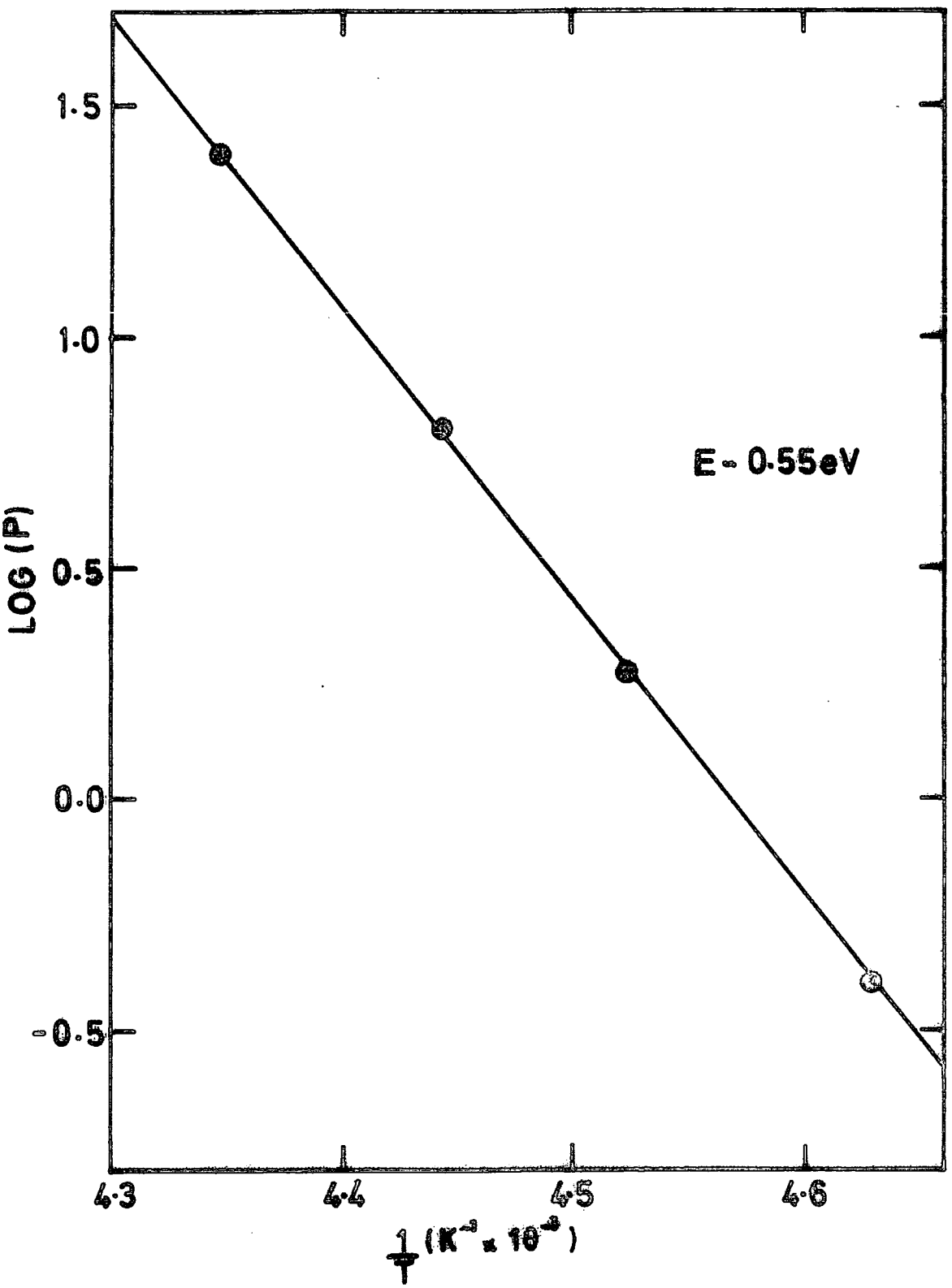

FIG.6·38 VARIATION OF LOG (P) WITH $\frac{1}{T}$ GIVING THE Ni^{3+} RECOVERY ACTIVATION ENERGY; TiO_2.

E.S.R. examination of B.S.10 showed the presence of Fe^{3+} and substitutional Cu^{2+}. U.V. irradiation at 40 K had no apparent effect on the cavity Q, but caused decreases of ∿ 35% in both Fe^{3+} and Cu^{2+} signal intensities. No new spectra were detected. Isochronal annealing of Fe^{3+} and Cu^{2+} spectra was then performed at 40 K intervals between 40 and 240 K. The Fe^{3+} concentration was restored to its pre-u.v. level after annealing at 200 K, in good agreement with similar measurements on N.L. crystals. There was, however, no evidence of the intermediate concentration change at ∿ 100-120 K found in Ni-TiO_2 (N.L.) and ascribed to the recombination of charge released from electron traps. Thatinterpretation is therefore supported in this case, since no spectra due to the electron traps were recorded. The intensity of the Cu^{2+} spectrum remained unchanged even after annealing at 240 K, which suggests that the energy level of this centre lies near the centre of the forbidden energy gap.

The crystal from B.S.10 was subsequently heated to 1000°C in O_2 and then quenched back to room temperature in about 10 seconds. E.S.R. measurements at 40 K showed that this heat treatment had caused substantial increases in both the Fe^{3+} and Cu^{2+} concentration and the appearance of both Mn^{3+} and Mn^{4+}. It is likely that the manganese and additional iron and copper were already present in the lattice, but in a form not detectable by e.s.r., e.g. quenching may freeze the impurities on well-separated sites but annealing may allow the metal ions to diffuse together to form metal aggregates. U.V. irradiation at 40 K caused the conversion of some Mn^{3+} ions to Mn^{4+}, a drop in Cu^{2+} concentration of ∿ 35%, but only a 15% drop in Fe^{3+} concentration. Furthermore, several new lines appeared, but isofrequent analysis of these spectra was hindered by interference from Mn^{4+} lines at most crystal orientations, so that the light-induced lines could only be easily isolated when the magnetic field was approximately parallel to the <001> axis. Most of these light-induced, 'quenched-in' defects did not appear to correspond to those

found in the National Lead crystal, and the spectra due to 'A' and 'B' centres were certainly not present.

6.11 MISCELLANEOUS SINGLE CRYSTAL RESULTS

Sections 6.3 to 6.10 have described the e.s.r. results obtained with specific crystals using techniques involving the liquid helium continuous flow cryostat. This section summarizes relevant earlier results obtained with a Nitrogen gas continuous flow cryostat. There was relatively poor temperature control and reproducibility with this cryostat so that most of the conclusions reached are fairly qualitative. In some cases, however, they complement the Helium cryostat results in that the design of the Nitrogen cryostat permitted measurements to be made above room temperature.

Isochronal annealing measurements of the Ni^{3+} spectrum in an 'as-received' National Lead crystal using the Nitrogen cryostat, in which the sample was heated to 150°C in the dark before being cooled to $\sim$ 160 K for u.v. irradiation, (Fig. 6.39) are in good agreement with measurements made with the Helium cryostat (see Fig. 6.35) in the region where the two temperature ranges overlap, i.e. 160 to 260 K. Fig. 6.39, however, shows an additional high temperature feature in the Ni^{3+} profile at $\sim$ 370 K, which probably corresponds to the thermal ionization of the Ni^{2+} centre. This suggests then that in the charge transfer at $\sim$ 220 K, Ni^{2+} centres are capturing holes which have been thermally released from other traps.

A National Lead crystal which had been doped with iron by evaporation and diffusion gave rise to a new e.s.r. spectrum after u.v. irradiation at $\sim$ 120 K, which was identified as the 'light-sensitive' substitutional Ni^{3+} spectrum reported by Gerritsen (1962). This centre was removed by annealing at temperatures in the 310-330 K range, i.e. similar to the highest T.L. peak at 328 K.

A Japanese rutile crystal was deliberately doped with Aluminium by evaporation and diffusion. This treatment caused the introduction of both

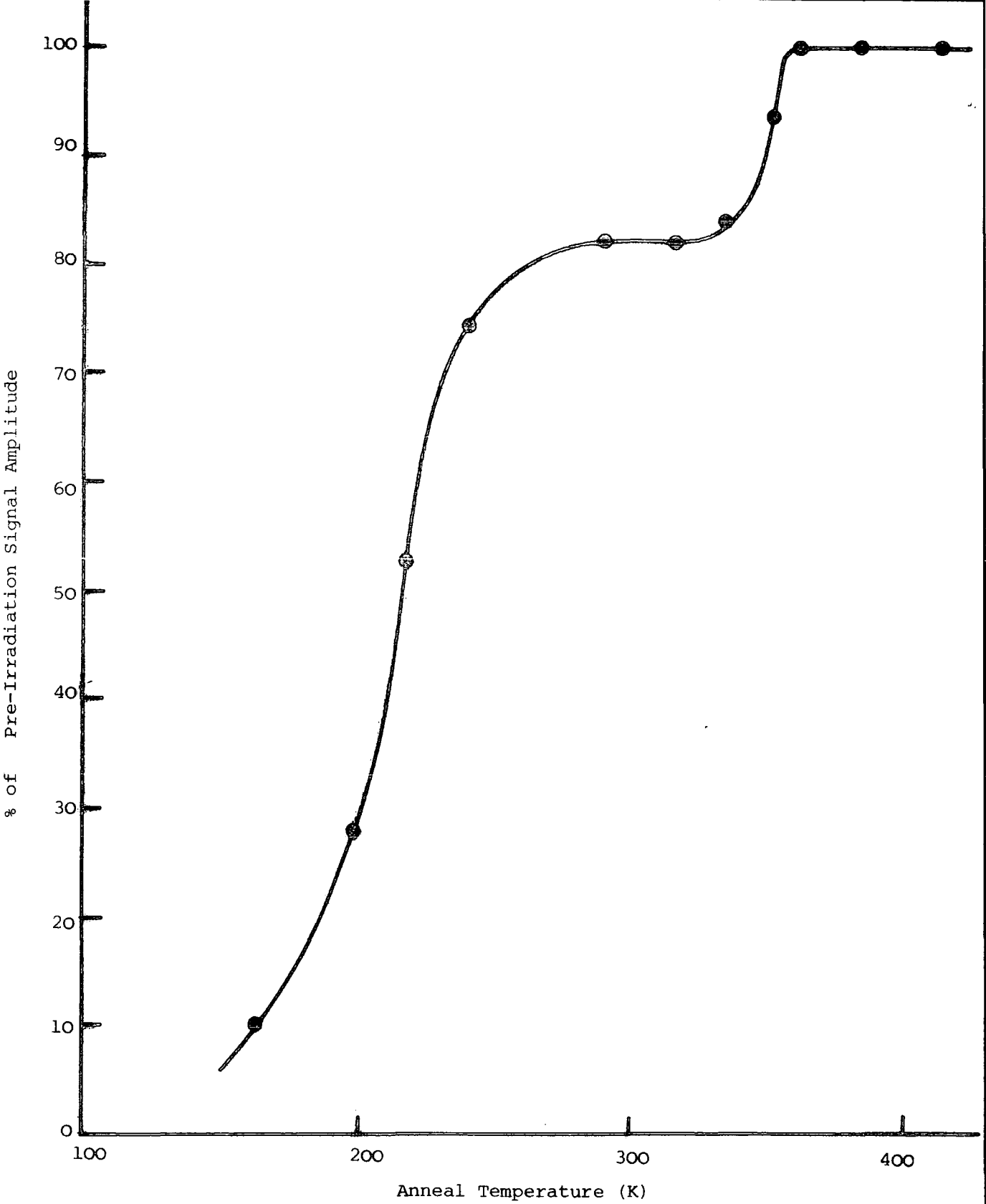

Figure 6.39 : Isochronal annealing of Ni^{3+} spectrum between 160 and 420 K using N_2 gas cryostat ; TiO_2 (N.L.)

interstitial and (light-sensitive) substitutional Ni^{3+} and also the appearance of two more light-induced spectra, Y and Z, following irradiation at $\sim$ 110 ($\pm$ 20) K. Isochronal annealing (Fig. 6.40) then showed that centre Z was removed by annealing at 140 ($\pm$ 20) K and that this charge transfer was accompanied by an increase in Fe^{3+} and decrease in Ni^{3+} concentrations, which suggest that the centre is an electron trap. The other light-induced centre (Y) was annealed out at temperatures between 260 and 300 K. Isofrequency analysis of these light-generated spectra was unsuccessful in identifying the centres, mainly due to the presence of several low-angle grain boundaries in the sample which meant that at certain orientations several resonance lines were recorded for every transition. As found in other samples there were increases in the concentrations of both Ni^{3+} and Fe^{3+} following annealing at 200-220^{o}C, suggesting a charge transfer of the type :-

$$Fe^{4+} + Ni^{2+} \longrightarrow Fe^{3+} + Ni^{3+} \qquad (6.6)$$

A further charge transfer between substitutional and interstitial Nickel appears to occur at $\sim$ 310 K, which suggests that substitutional Ni^{3+} is hole trap.

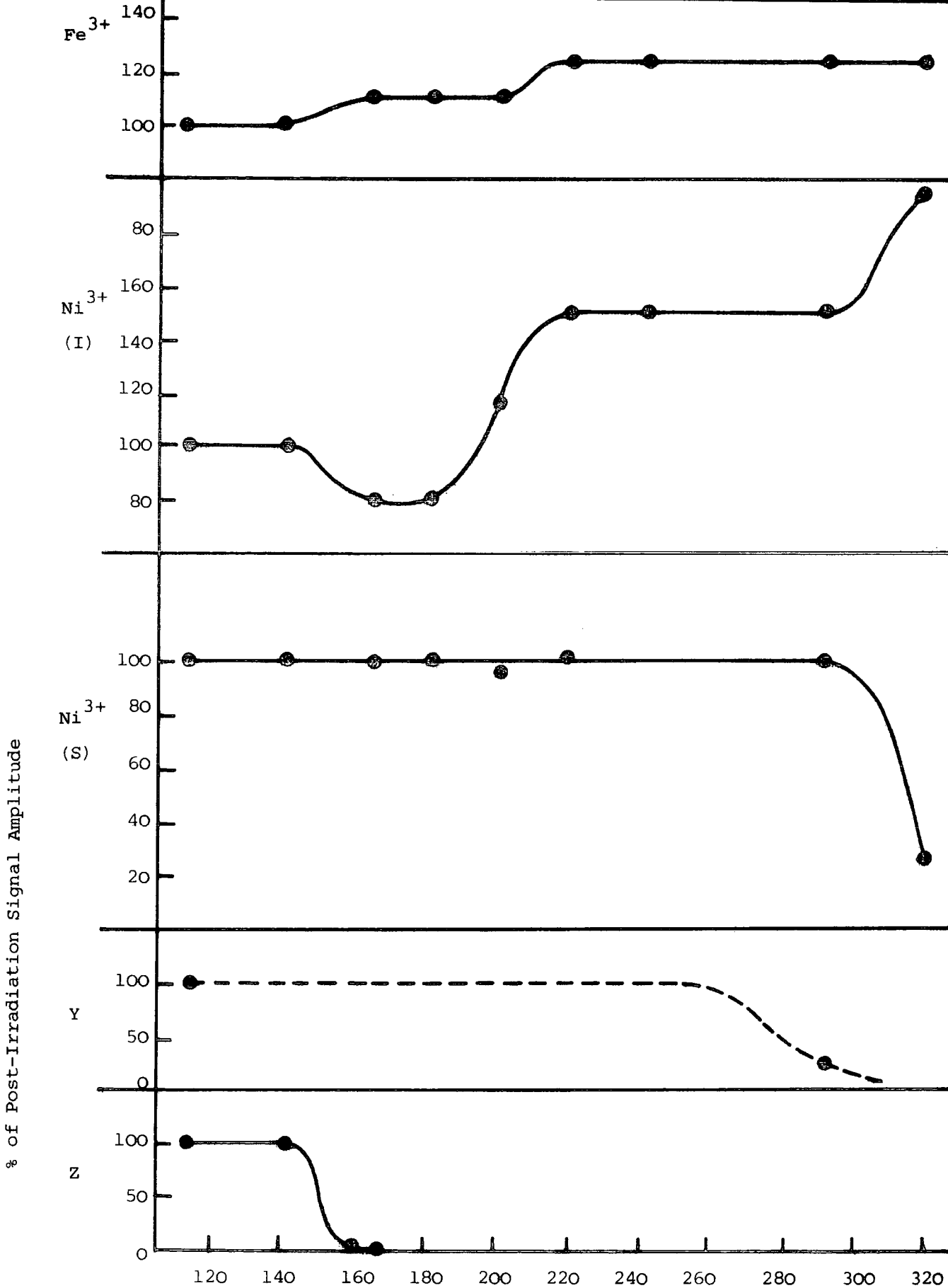

Figure 6.40 : Isochronal annealing (with N_2 Cryostat) of Fe^{3+}, interstitial and substitutional Ni^{3+}, 'Y' and 'Z', following u.v. irradiation at ∿ 110 K ; Al/TiO_2 (NaK)

CHAPTER 7

POWDER RESULTS

7.1 INTRODUCTION

Having established the use of e.s.r. techniques to investigate trapping centres in single crystals of rutile, the next step was to test their applicability to powders. A more specific aim was to determine whether any of the trapping centres or similar defects could be identified in samples of rutile pigment which were supplied for e.s.r. analysis by Tioxide International Limited.

Unlike the abundant data from single crystal studies, as reviewed in Chapter 4, there has been relatively little published literature concerning e.s.r. analysis of rutile powders, other than investigations of the surface chemistry of adsorbed gases (Primet, 1970), though Iyengar(1966) noted that reduction of rutile powder in hydrogen gave rise to an asymmetric signal centred on g $\sim$ 1.96, which was assigned to Ti^{3+} on normal cation sites.

E.S.R. signals from powder samples are in general more difficult to interpret than their single crystal counterparts. Much of the valuable information which can be extracted by studying the angular variation of the spectrum is lost, since the component crystallites of a powder have random orientation with respect to the magnetic field. Thus, with anisoptropic spectra the individual resonance lines from each crystallite are superimposed to give a much broader, usually asymmetric, powder absorption line. Very anisotropic single crystal spectra, such as those representing several of the impurity ions in rutile, may lead to powder signals which are so broad that they cannot be easily detected.

7.2 COMPUTER SIMULATION

It is sometimes possible, however, to extract some of the information needed to aid interpretation of powder spectra, by employing simulation techniques. This involves taking single crystal spin Hamiltonian parameters and using a computer programme to generate a theoretical powder spectrum. The parameters may then be adjusted in order to alter the shape of the powder pattern, with the aim of reproducing the features of the experimental powder spectrum.

A computer programme, which was originally written by Mr.W.Hutton of this Department for a study of e.s.r. in glass ceramics, was used in this work to simulate spectra from rutile pigment samples. The programme applies to $S = \frac{1}{2}$, $I = 0$ systems, with cubic, axial or orthorhombic symmetry, and can incorporate either Gaussian or Lorentzian line broadening functions. The basic steps of the programme are as follows :-

(a) Random orientation is represented by calculating g-values at each of 20,000 different orientations, equally incremented over the whole solid angle, from

$$g = \left[g_1^2 \sin^2\theta\sin^2\phi + g_2^2 \sin^2\theta\cos^2\phi + g_3^2 \cos^2\theta \right]^{\frac{1}{2}} \qquad (7.1)$$

where g_1,g_2 and g_3 are g-values along the principal crystal axes, and θ and ϕ define the orientation with respect to the magnetic field.

(b) The corresponding resonance field value for each element is found from

$$H = \frac{h\nu}{g\beta} \qquad (7.2)$$

(c) A histogram is created of the number of elements with resonance fields occurring in each cell of a magnetic field array, $H_1 \rightarrow H_n$, incremented in 0.5 Gauss intervals. This leads to the full lines in the upper traces of Fig. 7.1.

(d) The effect of crystallite line broadening is introduced by multiplying the value in each cell of the magnetic field array by an appropriate normalised single crystal lineshape function, giving the dashed lines in the upper traces of Fig. 7.1. The lineshape function can be either Gaussian, to simulate spin-lattice broadening,

$$G(H_o - H) = \frac{1}{\sqrt{2\pi}} \quad \frac{1}{\sigma_G} \quad \exp. \quad \left[\frac{-(H_o - H)^2}{2(\sigma_G)^2} \right] \qquad 3.$$

where $2\sigma_G$ is the width at half-height, or a Lorentzian function may be used, representing spin-spin broadening.

$$F(H_o - H) = \frac{1}{\pi} \quad \frac{2/\sigma_L}{(2/\sigma_L)^2 (H_o - H) + 1} \qquad 4.$$

where σ_L is the width at half-height.

(e) The final step is to compute the 1st derivative of the absorption lineshape in order to give a direct comparison with as-recorded experimental spectra.

While this computation can be a very useful tool under ideal conditions, it should be realised that it includes some assumptions which will often preclude an exact simulation of a real spectrum. In practice it is unlikely that the true broadening function will be either completely Gaussian or completely Lorentzian, but rather a combination of the two. Similarly, it is also unlikely that the recorded spectrum will be a true first derivative of the absorption line. Furthermore, it is possible that the recorded spectrum may not be a representative of the true lineshape,

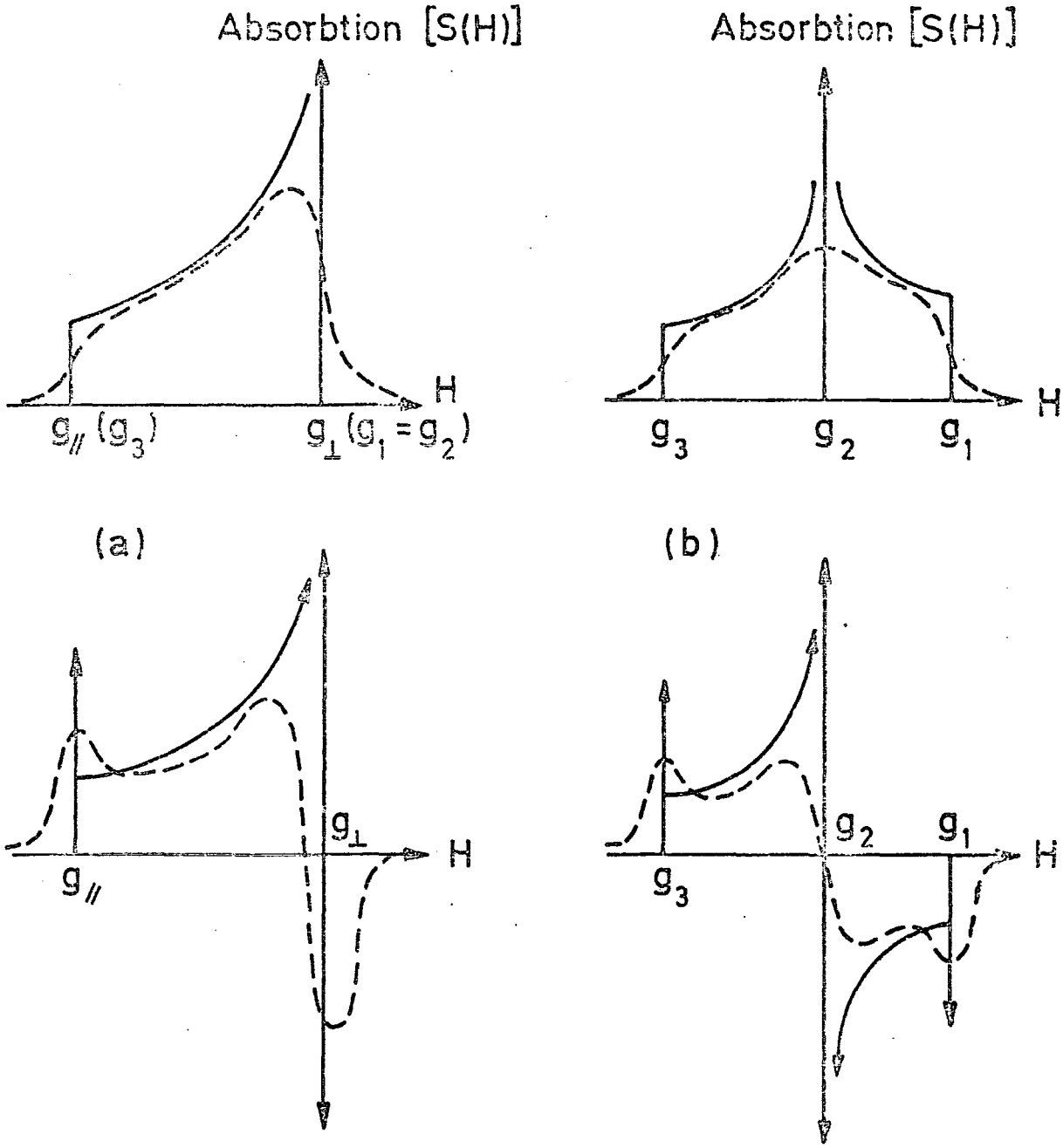

FIG. 7·1 Powder spectra from sites with (a) Axial Symmetry (b) Orthorhombic Symmetry.

Upper Traces:- Absorbtion Spectrum.
Lower Traces:- First Derivative of Spectrum.
Full Lines:- Idealized Spectra with δ Function Absorbtion by Individual Crystallites.
Dotted Lines:- 'Real' Spectra, i.e. the Effect of Crystallite Line Broadening.

due to such effects as overlapping with other signals or baseline drift. For these reasons the best-fit simulated pattern usually consists of a compromise between reproduction of different features of the true spectrum.

7.3 POWDER SAMPLES

The 7 rutile pigment samples which were supplied by Tioxide are listed in Table 7.1. This shows that samples A-F comprised a 6-way factorial trial, with aluminium concentration and the effect of an oxidizing heat treatment as the variable parameters. Trials at Tioxide have shown that both parameters have a significant effect on the durability of paints made from these pigments. The samples were submitted for e.s.r. analysis with the hope that a centre could be identified whose concentration varied in a similar way to the paint durability. One of the pigment samples (G) had been reduced by heating to 600^{o}C in H_2 for 30 minutes, in order to provide a reference signal from intrinsic defects. A mass spectrographic analysis of the pigments is presented in Table 7.2.

In addition to the pigments, a sample of the powder used to grow crystals was also examined, to determine whether any evidence of the spectra found in samples BS10 and BS16 could be detected in their source material.

7.4 RESULTS

7.4.1 Initial Characterisation

Initial e.s.r. measurements of powders with the Varian spectrometer at room temperature revealed no spectra of significant intensity in any of the samples, apart from a single, slightly anisotropic line from pigment G. The pigment samples were then sent for e.s.r. analysis with a Jeol spectrometer, by Dr. G.Brown at the Military College of Science, Shrivenham. The increased sensitivity of this spectrometer gave the following additional results, at room temperature :- Sample A gave a broad asymmetric line at $g \sim 2.10$. This signal was not detected in sample B. Both pigments C and D gave asymmetric lines at $g \sim 2.07$, of similar intensity in each

Sample	Al_2O_3 %	Heat treatment
A	0.61	None
B	0.61	30 min. at 600°C in O_2
C	3.28	None
D	3.28	30 min. at 600°C in O_2
E	1.56	None
F	1.56	30 min. at 600°C in O_2
G	1.56	30 min. at 600°C in H_2

TABLE 7.1 : Aluminium concentration and heat treatments of Tioxide International rutile pigment samples

Sample / Impurity	A, B	C, D	E, F, G
Al_2O_3	6100	31000	15000
SiO_2	6000	6000	6000
MgO	6	20	12
P_2O_5	8	25	8
K_2O_5	4	5	2
CaO	10	15	8
V_2O_5	0.5	2	1
Cr_2O_5	1	2	2
MnO	<0.2	0.3	<0.2
Fe	25	35	25
NiO	≤3	-	-
CoO	<2	<2	<2
Cu	<1	3	<1
ZnO	1	10	5
As_2O_3	35	4	1
SrO	<0.1	<0.1	<0.1
ZrO_2	15	20	2
Nb_2O_5	4	2	4
MoO_3	<3	<3	<3
Sn	13	4	4
Sb_2O_3	12	2	<1
BaO	0.5	0.5	<0.5
Ta_2O_5	1	3	5

TABLE 7.2 : Mass spectragraphic analysis (in p.p.m) of Tioxide International pigment samples.

sample. In addition, sample C also had a small, near-symmetric line at $g \sim 2.00$, which was not present in sample D. No signals were detected in either sample E or sample F. Reference to Table 2.1 suggests that the signals at $g \sim 2.10$ and $g \sim 2.00$ in samples A and C respectively may be associated with intrinsic defects which are removed by annealing in an oxidizing ambient at 600^{o} C. The signal at g = 2.07, which was unaffected by oxidation, was only found in samples containing 3.28% Al_2O_3. Since this is greater than the maximum solubility of Al in rutile (Slepetyo, 1969) it is possible that this signal may represent the presence of a new phase, such as Al_2TiO_5.

Measurements at 4.2 K with the Varian spectrometer showed the presence of two weak asymmetric lines in all the pigment samples, at magnetic fields corresponding to $g \sim 4.1$ and $g \sim 2.0$. In addition sample E also gave rise to a weak isotropic line at $g \sim 1.89$. The only pigment to produce a signal of sufficient intensity to allow accurate recording of the lineshape for computer simulation was sample G, which had been reduced in H_2. This signal, spectrum P, is shown in Fig. 7.2. The line is broad ($\sim$ 80 Gauss from positive to negative peaks) and slightly anisotropic, with a zero-crossing magnetic field corresponding to $g \sim 1.955$, i.e. similar to the value reported by Igengar (1966), also in H_2 - reduced rutile powder.

Initial attempts to simulate spectrum P assumed axial symmetry (from the relative lack of features, see Fig. 7.1), with $g_{\prime\prime}$ defined by the magnetic field value of the positive peak in the spectrum ($g_{\prime\prime}$ = 1.9714) and $g_{\perp}$ = 1.9280). Fig. 7.3 compares spectra simulated with these g-values, for three different magnitudes of Lorentzian broadening, function with the experimental spectrum. This shows that a σ_L value of $\sim$ 80 gauss is required to produce the same lack of features, while retaining the appropriate ratio of positive and negative peak heights. Gaussian broadening functions gave

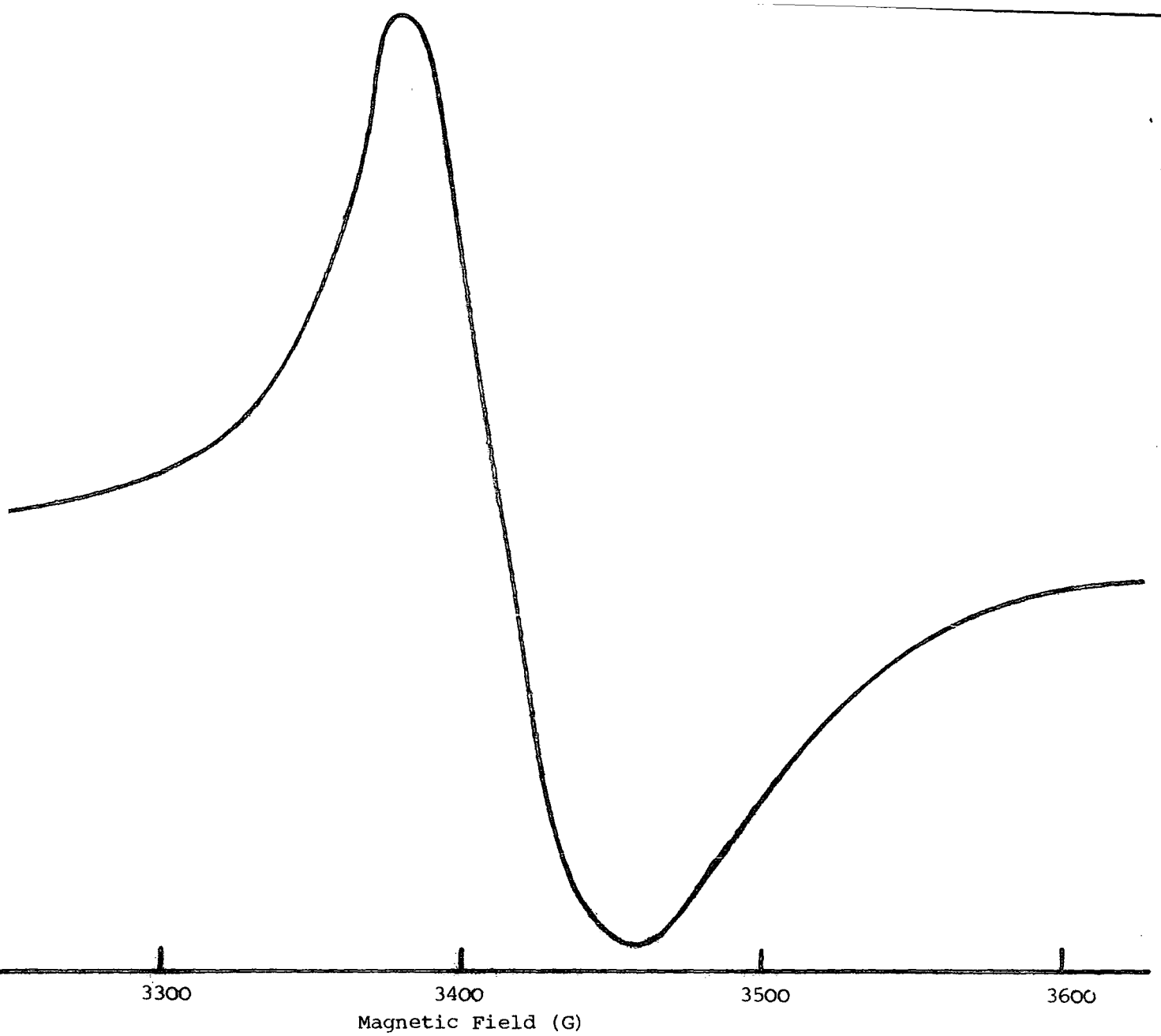

Figure 7.2 : Signal P, recorded at 4.2 K, ν = 9.331 GHz (Pigment G)

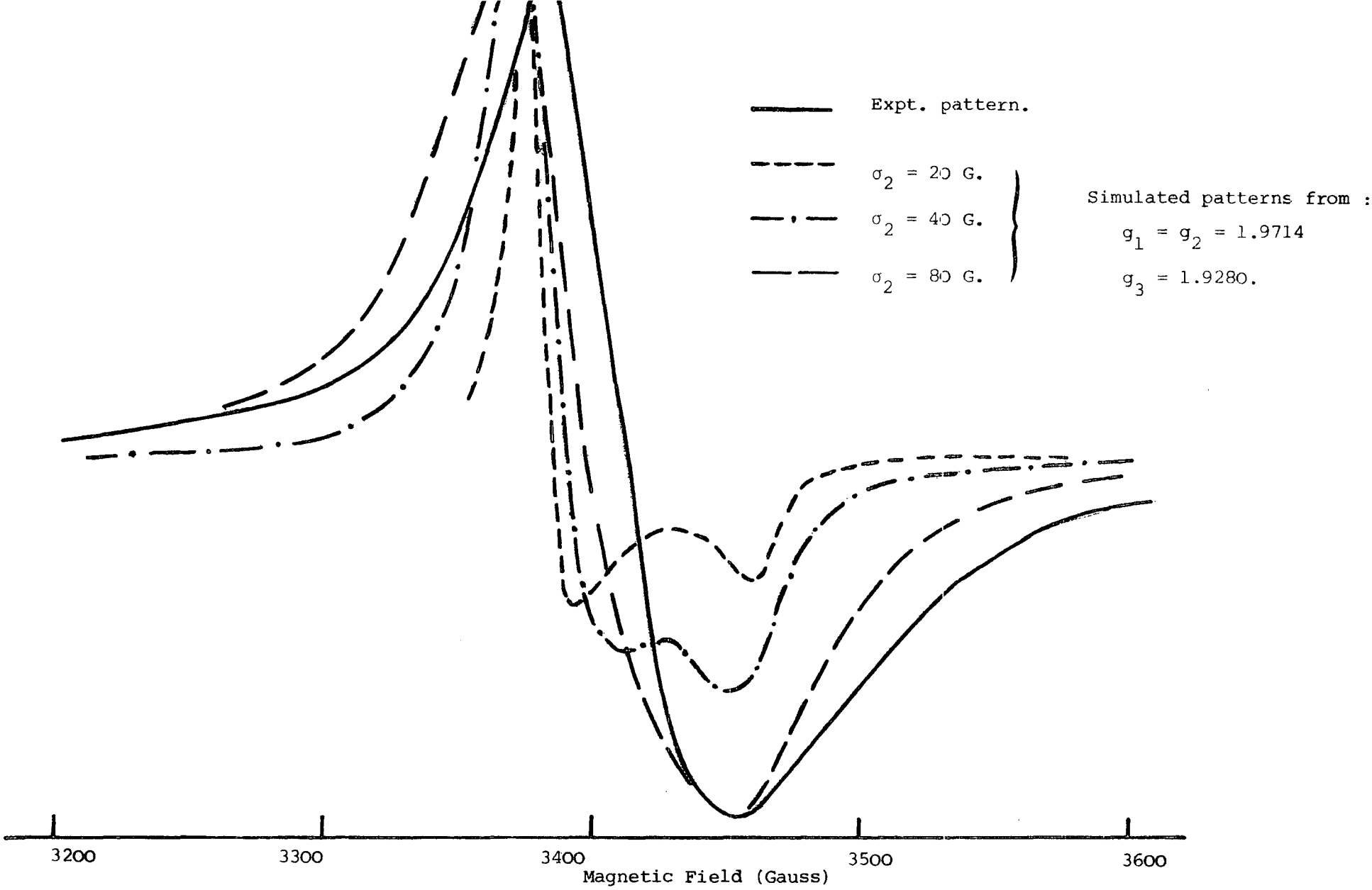

Figure 7.3 : Comparison of Experimental Powder Spectrum P with simulated spectra representing $g_1 = g_2 = 1.9714$, $g_3 = 1.9280$ and varying broadening functions ; $\nu = 9.331$ GHz.

lines that were too symmetrical. Slight adjustments to g-parameters to give $g_{\parallel}$ = 1.962 and $g_{\perp}$ 1.923 yielded the simulated pattern shown in Fig. 7. 4. The peaks and zero-crossing fields of the two patterns coincide within experimental limits, as does the rate of rise of the positive peak, though the rate of fall of the negative peak is less well matched. Introduction of a small degree of orthorhombic distortion produced no improvement in alignment and therefore Fig.7. 4 represents the best fit simulated spectrum, within the limitations of the programme. Thus, it appears that spectrum P may be described by $g_1 = g_2 = 1.962$ and $g_3 = 1.923$ together with a Lorentzian line broadening function, and σ_L = 80 gauss. Reference to Table 4.3, which lists e.s.r. parameters from non-stoichiometric rutile single crystals, shows that the parameter of spectrum P are similar to several others which have been interpreted as being due to intrinsic defects, either F centres or interstitial Ti^{3+}.

7.4.2 U.V. Sensitive Spectra

Ultra-violet irradiation of pigment samples at 4.2K had no observable effect on the intensities of the signals reported in section 7.4.1., but caused the appearance of a new signal, spectrum Q, at g $\sim$2.01. The same signal, a trace of which is shown in Fig 7.5, was detected in all seven pigment samples, but its intensity varied considerably. Although no accurate spin calibration measurements were performed, qualitative comparisons suggested that the intensity was greater in samples which had received the oxidizing heat treatment.

The first simulations of spectrum Q compared Lorentzian and Gaussian broadening functions with varying linewidths using axial symmetry. As with spectrum P, it was found that a Gaussian function was inappropriate, being unable to reproduce the peak height ratios while retaining the correct half-height widths. Better progress was made with the Lorentzian function and Fig.7.6 depicts lineshapes for four different values of σ_L, with g_1=g_2=2.0074

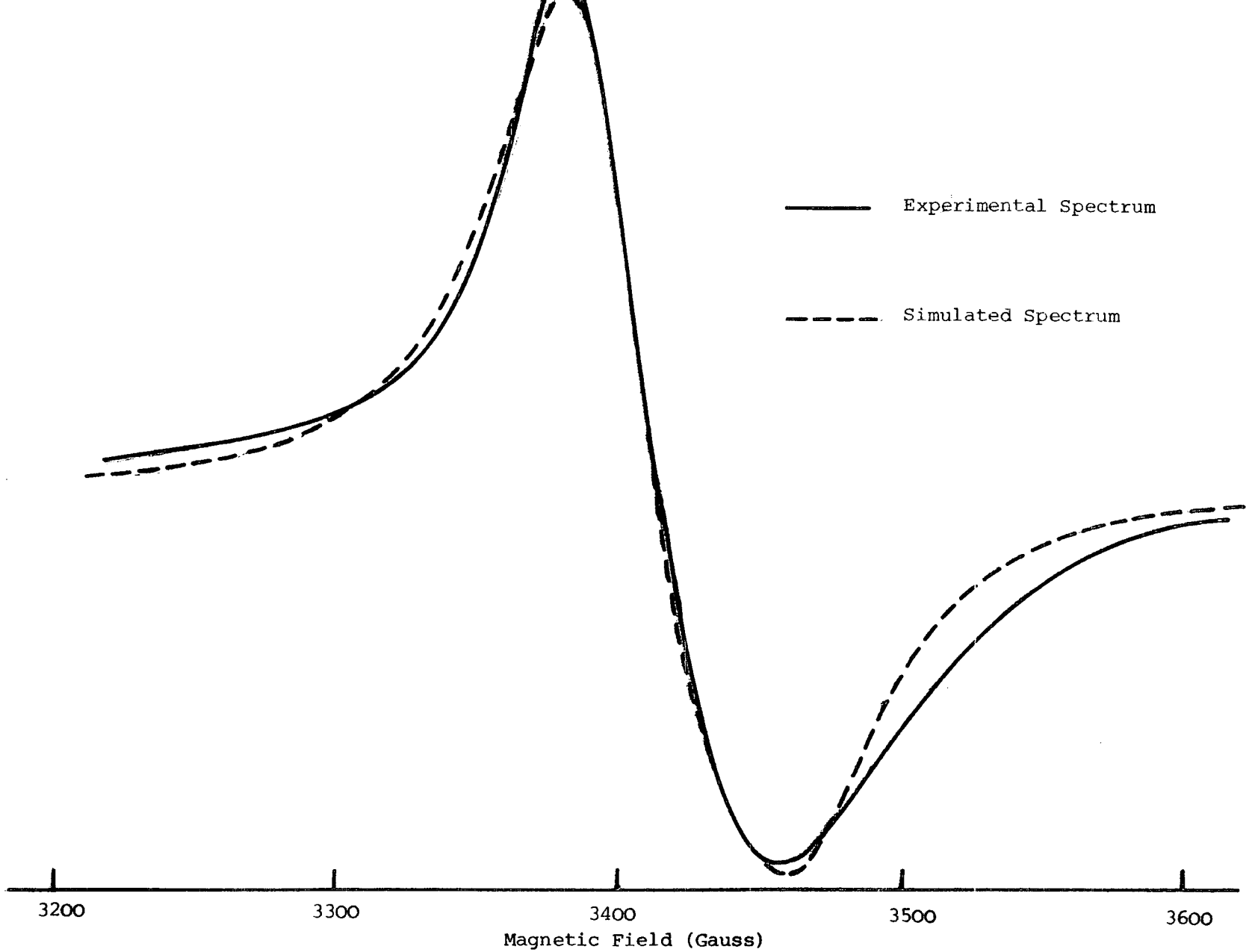

Figure 7.4 : Comparison of experimental powder spectrum P with best-fit simulated spectrum

$g_1 = g_2 = 1.962$, $g_3 = 1.923$, $\sigma_2 = 80$ G ; $\nu = 9.331$ GHz.

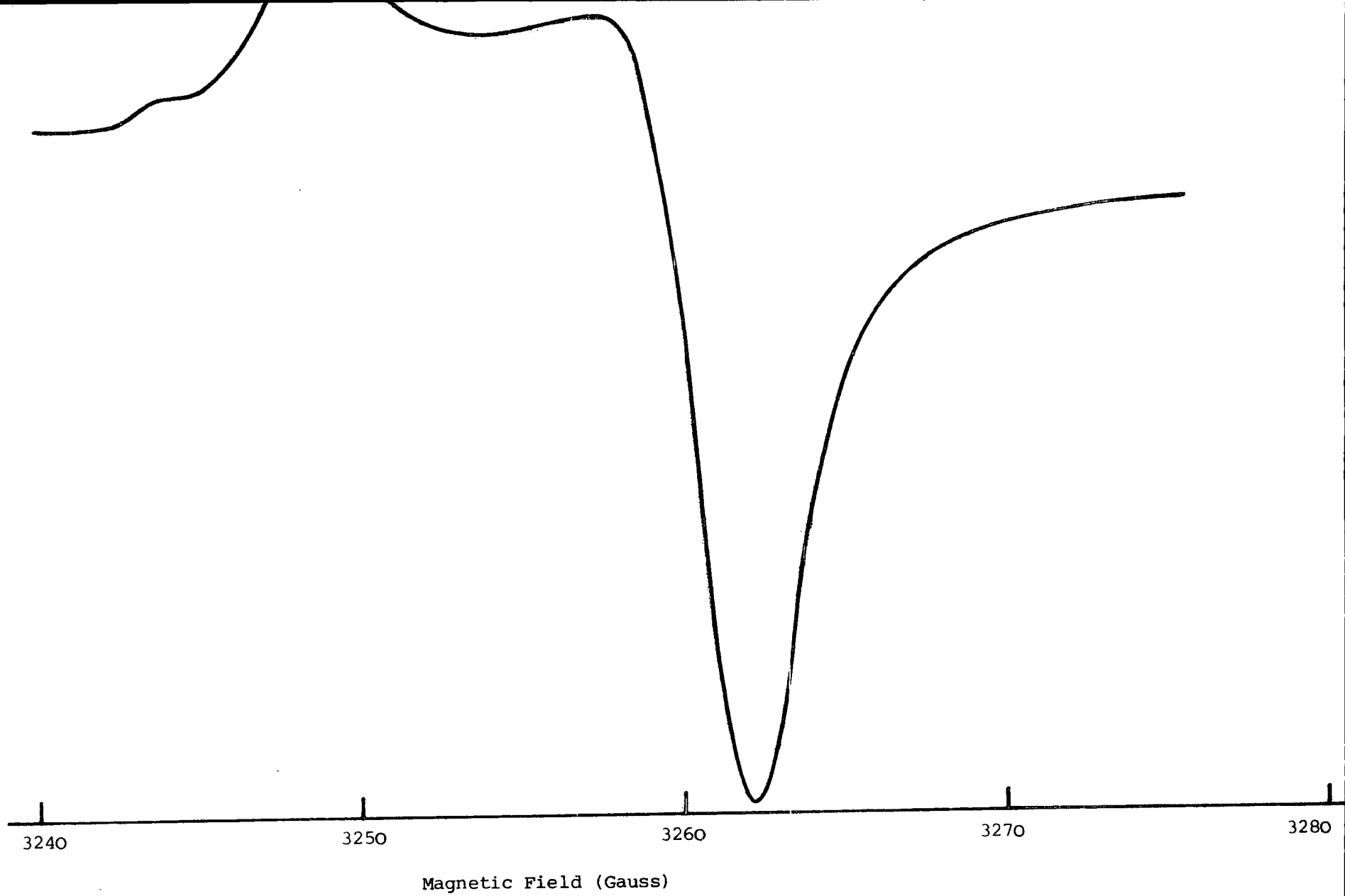

Figure 7.5 : Powder spectrum Q, created by u.v. irradiation at 4.2 K, ν = 9.166 GHz.

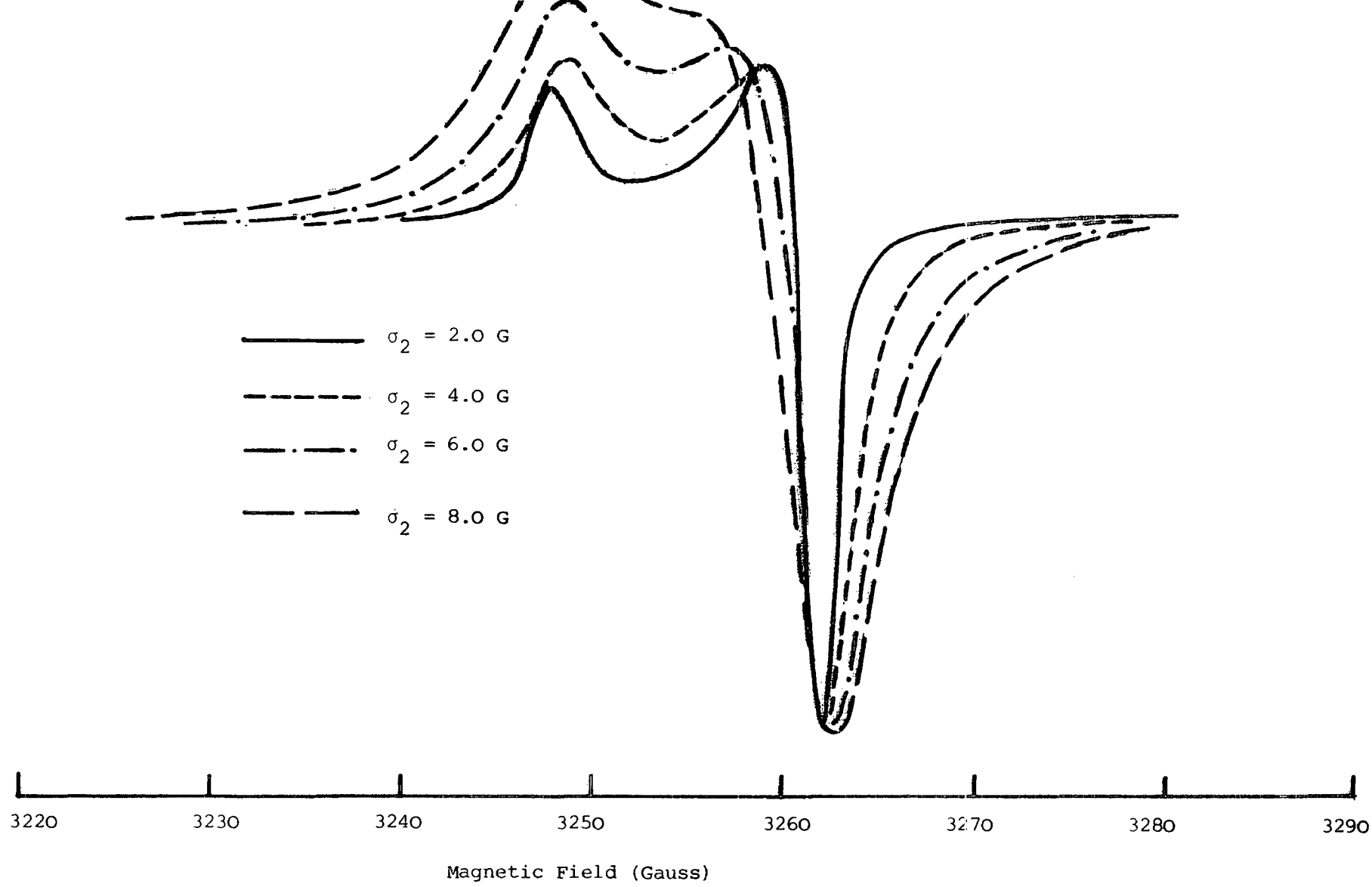

Figure 7.6 : Simulated powder spectra for $g_1 = g_2 = 2.0074$, $g_3 = 2.0155$, showing the effect on lineshape of varying the broadening function ; $\nu = 9.166$ GHz.

and g_3 = 2.0155. A value of σ_L = 6.0 gauss gives the best reproduction of the shape of the shoulder at ∿3258 gauss. Further small adjustments in the parameters gave the best fit simulated pattern, as shown in Fig. 7.7, with $g_1 = g_2$ = 2.0077, g_3 = 2.0153 and σ_L = 5.5 gauss. Thus the spectrum appear to be unlike any other reported from e.s.r. measurements on rutile powders. Moreover, the parameters cannot be matched with any of the data for centres in u.v.-irradiated single crystals. It is thought that since the g-values are greater than the free electron value, spectrum Q may represent a trapped hole.

Further evidence for this interpretation was gained from isochronal annealing and isothermal decay measurements. Fig. 7.8 depicts the variation of signal amplitude during and after u.v.irradiation at 4.2K and shows an exponential growth during irradiation, followed by a rapid fall to ∿ 40% of maximum intensity when irradiation ceases. It is suggested that this behaviour corresponds to filling of both hole-trapping and electron-trapping centres during irradiation and then thermal release of electron from shallow traps followed by their recombination at hole traps, causing the decrease in the number of 'Q' centres. Fig 7.9 suggests that this recombination process is initially monomolecular and then, as retrapping becomes significant, the kinetics become bimolecular.

Isochronal annealing of signal 'Q' between 4 and 100K (see Fig 7.10) revealed two temperature regions in which charge transfers occurred, both causing further decreases in the intensity of 'Q'. The first, at ∿ 10K, is assumed to correspond to thermal release of electrons from another shallow trapping level and subsequent recombination at 'Q' centres. The second at ∿ 80K may either represent a similar process with a deeper electron trap or the direct thermal release of trapped holes. Fig 7.11 shows that the decrease in intensity between 60 and 100K is evenly spread over the whole temperature range and may possibly indicate the presence of several different electron traps with similar thermal ionisation temperatures, as was found in

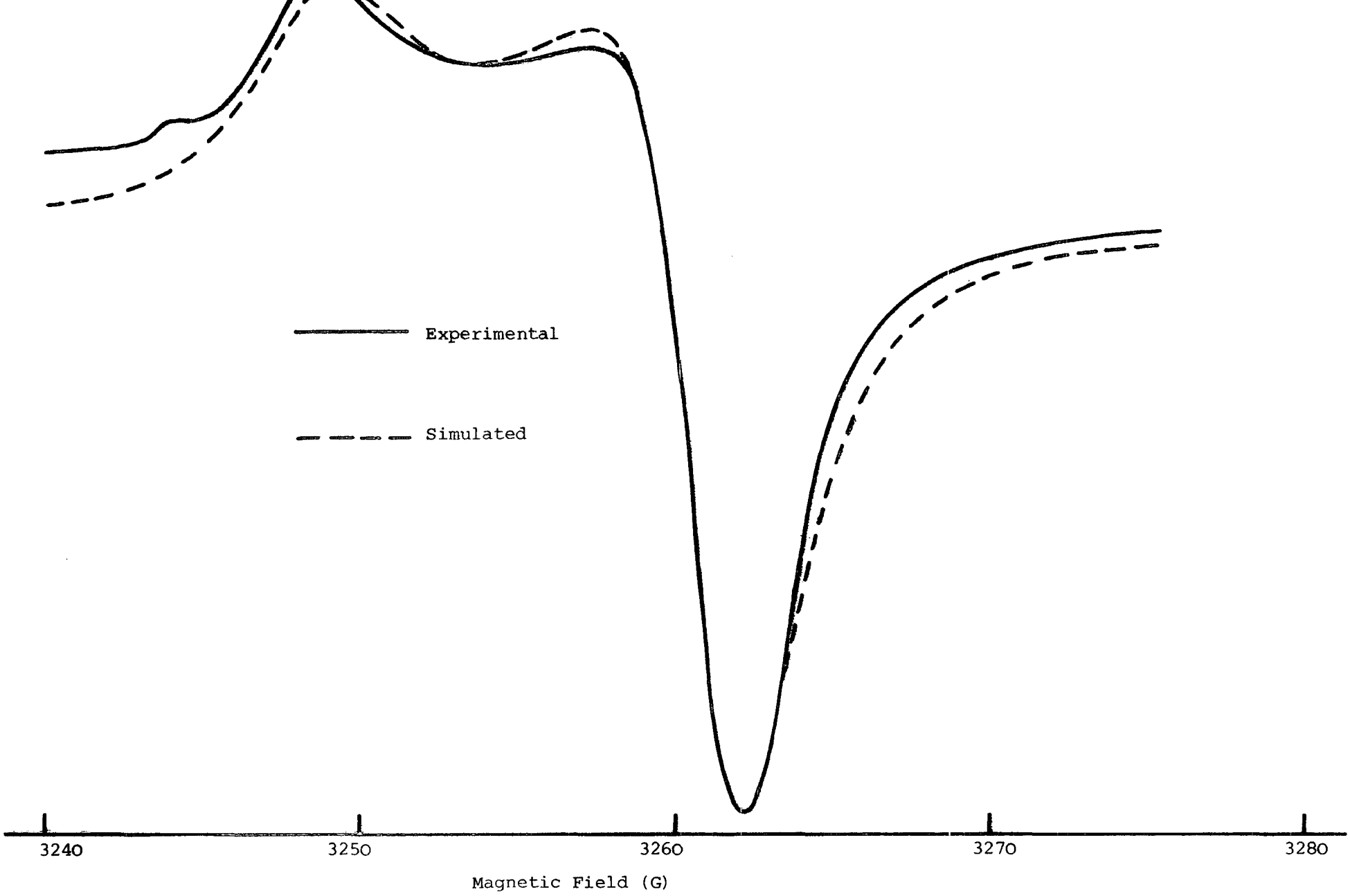

Figure 7.7 : Comparison of experimental powder spectrum Q, with best-fit simulated spectrum

$g_1 = g_2 = 2.0077$, $g_3 = 2.0153$, $\sigma_2 = 5.5$ G; $\nu = 9.166$ GHz.

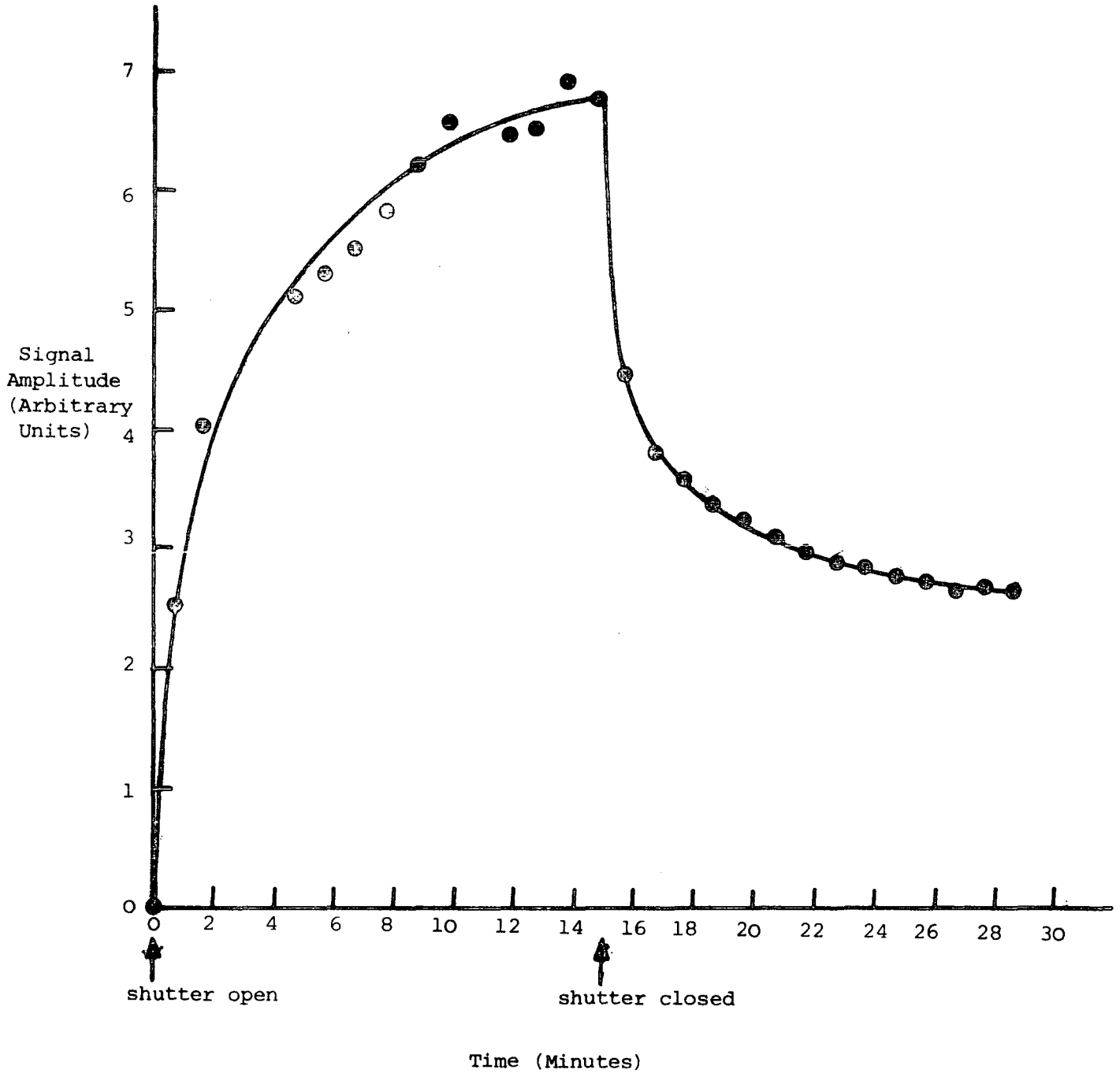

Figure 7.8 : Variation of amplitude of signal Q with time, during and after u.v. irradiation at 4.2 K (Pigment D).

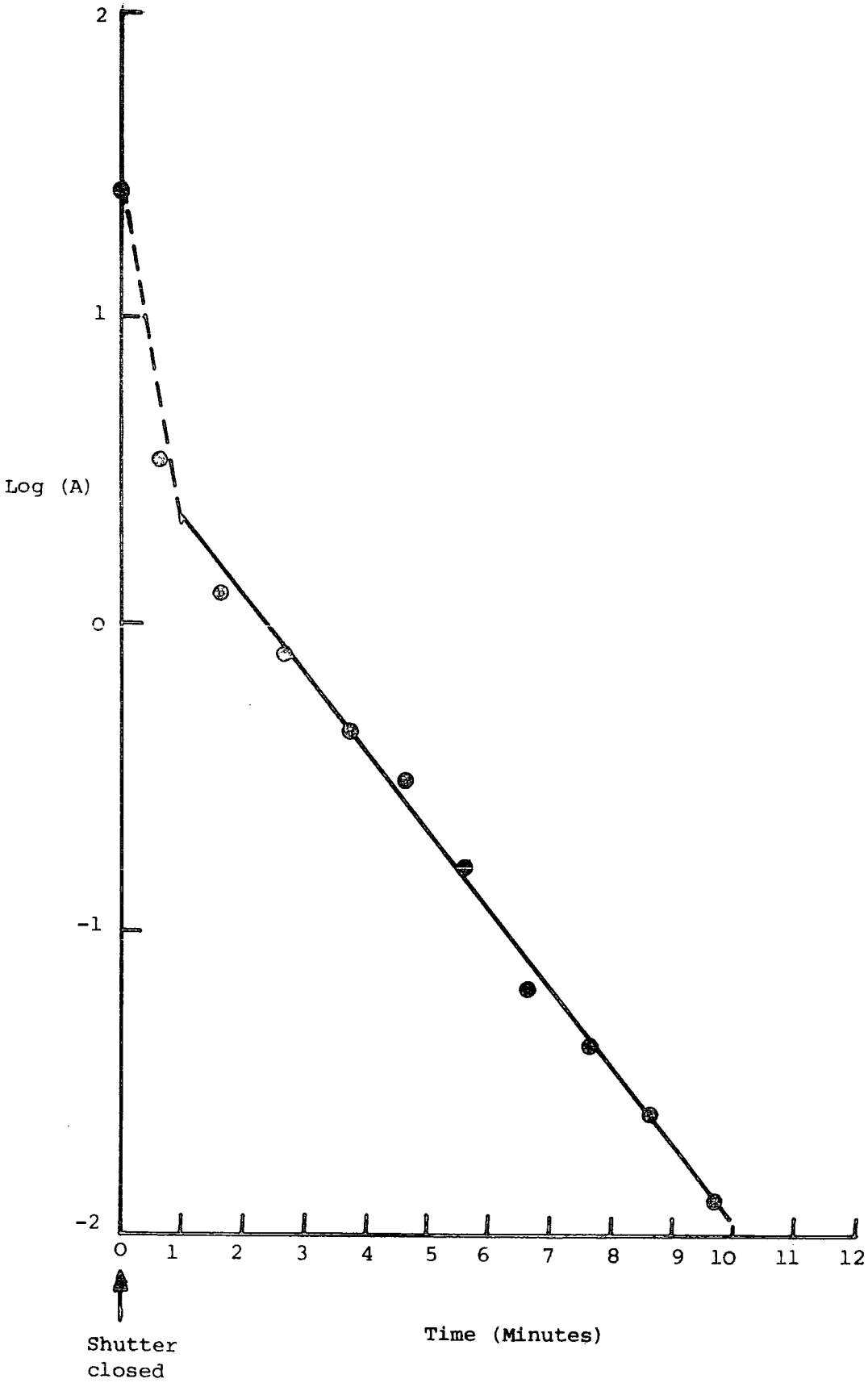

Figure 7.9 : Log (A) of signal Q vs. time, after u.v. irradiation at 4.2 K (Pigment D).

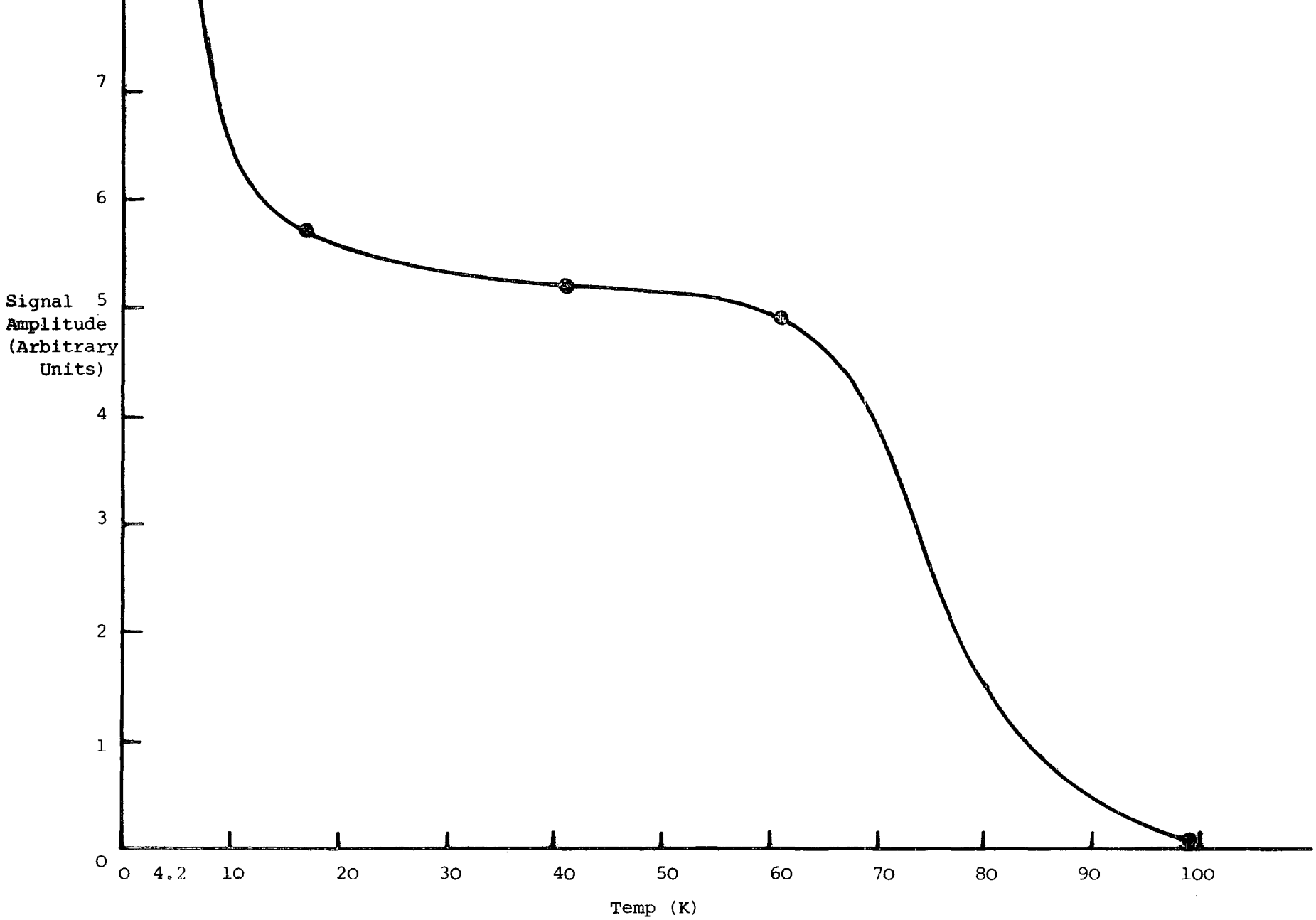

Figure 7.10 : Effect of isochronal annealing on the amplitude of signal Q, following u.v. irradiation at 4.2 K (Pigment E).

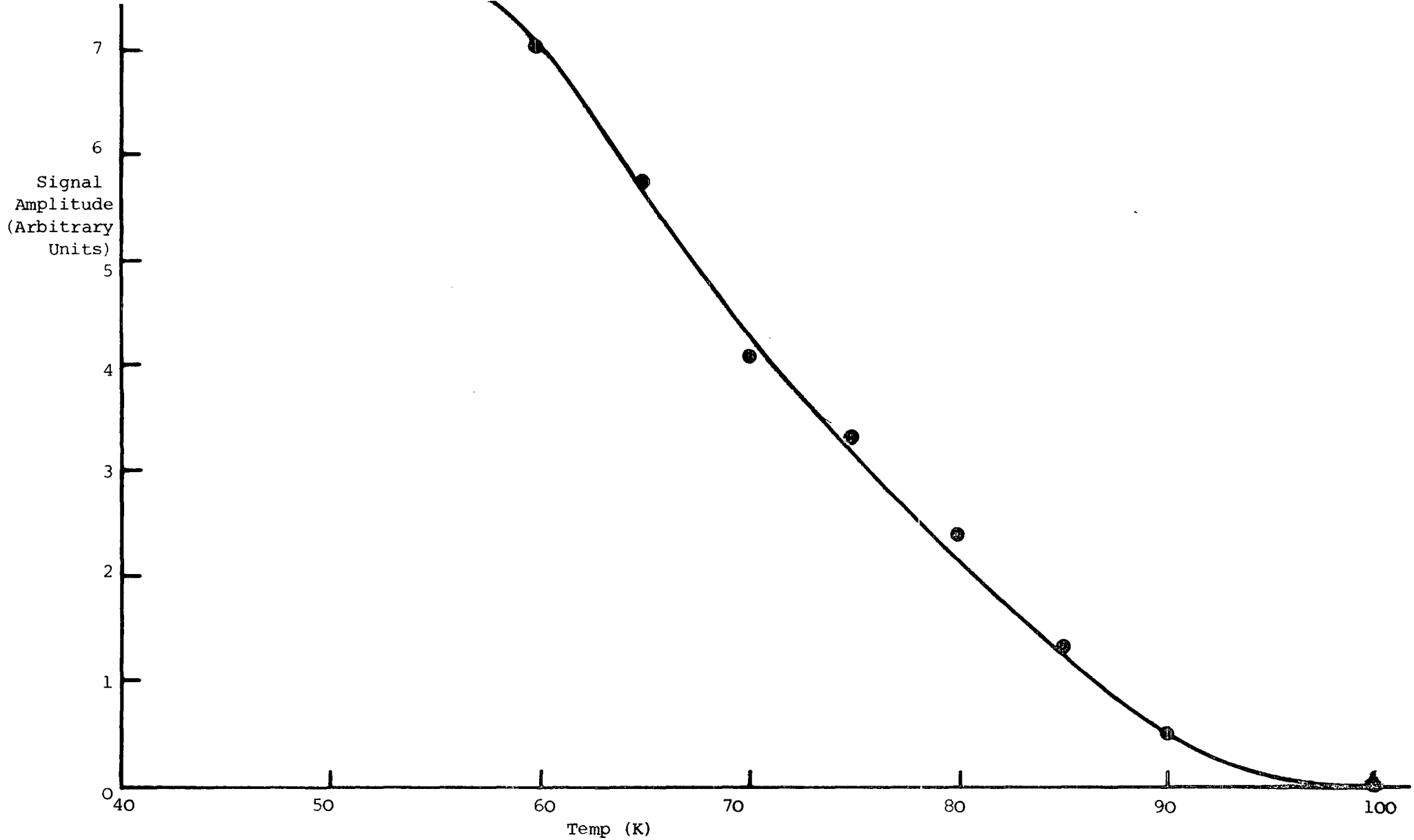

Figure 7.11 : Effect of isochronal annealing on the amplitude of signal Q, following u.v. irradiation at 40 K (pigment A).

the single crystal work.

Unfortunately, lack of time precluded a comprehensive study of isochronal annealing of spectrum Q in all the pigment samples, but sufficient encouraging results were obtained to suggest that such a study may be used to investigate variations in the distribution of trapping centres between the different samples.

7.4.3 Sandy Rutile

A sample of the sandy rutile powder (batch DN5) used to grow crystals in the plasma torch was submitted for e.s.r. analysis. No signals at all could be observed at 4.2K initially, but following u.v. irradiation two new lines appeared, at magnetic fields corresponding to $g \sim 2.01$ and $g \sim 1.97$. Both signals were too weak to allow either line shape analysis or quantitative intensity measurements.

CHAPTER 8

DISCUSSION AND CONCLUSIONS

8.1 TECHNIQUES

8.1.1 Crystal Growth and Preparation

An O_2-Ar plasma torch at Tioxide International Research Labs. was adapted and modified to provide a reliable crystal growth apparatus which produced rutile boules at a rate of $\sim$ 3 cm/hour by a semi-automatic process. Analysis of the boules, which were typically 1 cm in diameter and 3 cm in length, showed them to be monocrystalline and generally of higher purity than crystals grown by the conventional Verneuil technique. The impurity doping level was controlled by variation in the composition of the starting material. Adjustment of the position and ambient of the plasma growth zone gave control of the resistivity of the rutile boules and allowed the growth, for the first time, of fully stoichiometric rutile single crystals.

Rutile crystals from several sources were aligned by X-ray diffraction methods, cut and polished to produce suitable samples for e.s.r. analysis. A quartz tube furnace was used both for oxidation/reduction experiments and for diffusion doping of impurity ions at temperatures up to 1200^{o}C.

8.1.2 E.S.R. Analysis

A Varian e.s.r. spectrometer was used to characterise rutile samples (both single crystals and powders) with respect to the identity and distribution of paramagnetic defects. The main part of this project concerned the measurement of changes to e.s.r. spectra with optical and thermal stimulation of the sample and for this purpose it was necessary to incorporate facilities into the spectrometer system to enable (a) the

direct optical irradiation of samples in the microwave cavity and (b) control over the sample temperature between 4 and 300K with a continuous flow liquid Helium cryostat.

8.2 SINGLE CRYSTAL RESULTS

The intensities of most of the e.s.r. spectra from rutile crystals were affected by ultra-violet irradiation at low temperatures ($\sim$ 40K). This treatment also caused the appearance of several new spectra, for which Spin Hamiltonian parameters were determined from isofrequency angular analysis. It is thought that the cause of these changes in spectral intensity is a redistribution of charge, from an initial equilibrium state in which there are relatively few charge carriers trapped at impurity centres to a final state where the incidence of optical energy has filled most centres with carriers which are then trapped in the metastable state by lack of thermal energy.

The relative position of the trapping levels in the forbidden band gap was determined from isochronal annealing studies, which gave the temperature required to revert the spectral intensities to pre-irradiated, equilibrium values. Isochronal annealing also revealed interactions, or charge transers, between different impurity centres which lead to assignment of their photo-electronic roles, i.e. as electron or hole traps, or recombination centres. Studies of the intensity vs temperature profiles of the deeper centres allowed deductions to be made of the existence of further trapping centres, whose presence could not be detected directly by e.s.r.

Measurements of rates of thermally stimulated charge transfers and their variation with temperature were used to calculate the trap depths of some of the impurity centres, though, due to the complexity of trapping kinetics in rutile, these values are only regarded as 1st order estimates.

Table 8.1 presents a summary of the temperatures at which thermally stimulated charge transfers were detected by isochronal annealing of e.s.r.

E. S. R.			T. L.	
Ionization Temp. (K)	Activation Energy (eV)	Interpretation	Peak Temp. (K)	Trap Depth (eV)
30-40	0.075	hole trap		
40-50	0.12	electron trap - centre H		
70-80	0.12	electron trap - centre G		
70-80		electron trap - centre D	100	0.13
90-100		electron trap - centre C		
100-120	0.22	electron trap - centre B	118	0.24
140-150		hole trap		
160-200		hole trap - centre A	169	0.37
180-220	0.52	hole trap - Fe^{4+}	239	0.51
200-240	0.55	hole trap (recombined at Ni)	296	0.60
300-340		Substitutional Ni	328	0.68
360-380		Interstitial Ni		

TABLE 8.1 : Summary of temperatures of thermally stimulated charge transfers and associated activation energies of defects in rutile single crystals, from e.s.r. measurements, and comparison with thermoluminescence data.

spectra, together with activation energies, where available and interpretation of the centre responsible for the reaction. These values are compared with glow curve peak temperatures and trap depths, derived from thermoluminescence measurements. It is important to note that both sets of temperature data in Table 8.1 can be affected by experimental conditions, i.e. the apparent charge transfer temperature increases as (a) the isochronal anneal time decreases and (b) the thermoluminescence heating rate increases. In view of the relatively long anneal time (5-10 mins) and fast heating rate (0.5 K sec^{-1}) used in the e.s.r. and T.L. measurements respectively, it is expected that the former would indicate a lower ionization temperature if the same event was recorded by both techniques.

The shallowest centre detected in this work is a hole trap, with a thermal activation temperature of $\sim$ 35 K and an energy level $\sim$ 0.075 eV above the valence band. Although this centre did not give rise to any observable e.s.r. spectrum, its presence and charge state were deduced from interactions with other defect centres, i.e. after thermal release the holes are re-trapped at deeper levels to form Fe^{4+} and 'A' centres.

There are at least five different electron trapping centres (B-H) with ionization temperatures between 40 and 120 K. The shallowest of these is centre H, which has a trap depth of $\sim$ 0.12 eV and thermal activation temperature of $\sim$ 50 K. Two of the electron traps had thermal activation temperatures of $\sim$ 75 K and isothermal analysis of one of them, centre G, also gave an estimated trap depth of 0.12 eV, which is close to the value derived from the 1st T.L. peak at 100 K. A further electron trap, centre C, is thermally ionized at $\sim$ 95 K. The deepest of this set of electron traps, centre B, has a thermal ionization temperature ($\sim$ 110 K) and trap depth ($\sim$ 0.22 eV) which correlate well with the 2nd T.L. peak at 118 K.

Another defect, centre A, was interpreted as a hole trap with a thermal ionization temperature of $\sim$ 170 K. At lower temperatures A centres

behaved as recombination sites for electron freed from B centres. Centre X had a similar isochronal anneal profile to centre A, but appeared to be at a much deeper energy level.

All of these defect centres, A-H and X, gave e.s.r. spectra which only appeared after u.v. irradiation. The Spin Hamiltonian parameters for each light-generated spectrum were determined by isofrequency analysis and are summarized in Table 8.2. All of these centres were detected in National Lead rutile crystals which were heavily doped with Aluminium. The two deepest traps, centres A and B, were also detected in one of the plasma-grown boules, BS16, which was also deliberately doped with Al. There was no evidence of the u.v.-generated spectra in another of the plasma-grown boules, BS10, which contained relatively little Aluminium. Diffusion doping of Aluminium into a Nakazumi rutile crystal caused the introduction of two more light-sensitive spectra, from centres labelled Y and Z, with thermal ionization temperatures of $\sim$ 280 K and 150 K respectively, though it was not possible to determine spin Hamiltonian parameters for these spectra,due to the presence of several low angle grain boundaries in the sample. Thus, although there is no positive identification of the u.v.-generated centres A-H and X-Z, it is suggested that most if not all of them are connected with the presence of Aluminium and may consist of complexes of charge trapped at normal lattice sites, e.g. Ti^{3+}, O^{-} or V_O^{-} , with neighbouring Al^{3+} ions. Two of the centres, G and H, had g-parameters which agreed closely with those reported (Kerssen, 1973) in Al-doped, vacuum-reduced rutile and interpreted as a Ti^{3+}-Al^{3+}-Al^{3+} complex.

Iron appears to behave as a hole trap in the rutile lattice, with u.v. irradiation at low temperatures causing the conversion of some Fe^{3+} ions to Fe^{4+}. The trapped holes may then be removed either by recombining electrons or by thermal ionization at $\sim$200K. This behaviour was observed in five different samples from various sources. Isothermal recovery measurements lead

Centre	g_{110}	$g_{1\bar{1}0}$	g_{001}	D (GHz)	E (GHz)	Site Symmetry	Interpretation
A	4.59	1.94	3.36			Subst.	Hole trap
B	1.922	1.896	1.793			Subst.	Electron trap
C	1.953	1.846	1.788	0.701	0.072	Subst.	Electron trap
D	1.956	1.839	1.785	0.712	0.078	Subst.	Electron trap
E	1.915	1.872	1.778			Subst.	Electron trap
G	g_{100} = 1.956	g_{010} = 1.919	1.811			Perturbed subst.or interst.	Electron trap
H	g_{100} = 1.955	g_{010} = 1.920	1.822			"	Electron trap
X	1.965	1.914	1.935			Subst.	Recombination centre

TABLE 8.2 : Spin Hamiltonian Parameters of u.v. generated E.S.R.spectra

to an activation energy which places the Fe level $\sim$ 0.52 eV above the valence band, which is similar to the trap depth derived from the 4th T.L. peak. This value of activation energy is also the same as that determined for the thermal bleaching of photochromic absorption in rutile (Clark, 1970), which had been attributed to the presence of Iron, though there was uncertainty concerning the mechanism involved. The isochronal annealing results of this project suggest that the appearance of the absorption band during u.v. irradiation is due to the creation of Fe^{4+} ions.

Chromium appears to behave in a similar manner to Iron at low temperatures, i.e. u.v. irradiation converts some Cr^{3+} ions to Cr^{4+}, which then act as recombination sites for electrons freed from shallow-traps, but the thermal ionization temperature of Cr^{4+} centres was not determined.

Nickel and Manganese behave as recombination centres in rutile, with high thermal ionization temperatures and energy levels near the centre of the band gap. Charge transfers involving these ions can be especially informative, since Ni^{2+}, Ni^{3+}, Mn^{3+} and Mn^{4+} all give rise to observable e.s.r. spectra. It is therefore possible to detect simultaneously signals from both full and empty traps and hence deduce the polarity of the charge carriers in question. Thus, for example, some of the electrons freed from centres B-H by heating to 60-120K recombined at Ni^{3+} and Mn^{4+} sites to form Ni^{2+} and Mn^{3+} respectively. Nickel in particular is very sensitive to interactions with both hole and electron traps and charge transfers involving changes to Ni^{3+} concentrations were observed at at least six different temperatures between 40 and 400K. Isothermal decay measurements at temperatures between 210 and 230K gave an activation energy of 0.55 eV, corresponding to the thermal ionization of a hole trap, possibly Fe^{4+}, and subsequent recapture at Ni^{2+} sites. At higher temperatures a further interaction between Ni^{3+} (interstitial) and another centre interpreted as 'light-sensitive' substitutional Ni^{3+} (Gerritsen, 1963) was observed at $\sim$ 320K, in good agreement with the

highest T.L. peak at 328K. A final charge transfer involving Ni^{3+} occurs at ∿ 370K, and it is thought that this represents thermal ionization of Ni^{2+}.

Copper is another centre with an energy level near the centre of the band gap and thermal ionization temperature greater than 300K.

In general, most of the paramagnetic defects which give rise to e.s.r. spectra, also appear to play active roles in the photoelectronic reactions of rutile. The nature of the roles were deduced in most cases and many of the thermally stimulated changes to e.s.r. spectra occurred at similar temperatures to published T.S.C. and T.L. data. (The two shallowest centres are below the range of existing T.S.C. and T.L. measurements, which have been recorded with a base temperature of ∿ 80K). Furthermore, estimates of activation energies, from isothermal annealing of e.s.r. spectra, yielded values which were within 10% of those derived by the other techniques.

The main advantage of using e.s.r. to study trapping centres is that the recorded signal is a direct measure of defect concentration and is relatively unaffected by other influences, unlike e.g. T.S.C. in which thermally generated dark current can swamp weak signals, especially at high temperatures. With e.s.r. each trapping centre produces a characteristic signal which may be detected independently of or simultaneously with signals from other centres. It is thus possible to isolate several different centres with similar trap depths and this may explain why several more traps were detected by e.s.r. than by T.S.C. Finally, successful analysis of an e.s.r. spectrum can lead to an identification of a trapping centre and its surrounding environment.

8.3 POWDER RESULTS

Initial studies of rutile pigments supplied by Tioxide International gave encouraging results. The same ultra-violet-activated e.s.r. spectrum was observed in 7 different pigment samples, but with varying intensity. The Spin Hamiltonian parameters of this and another powder spectrum were determined by computer simulations of the powder patterns from single crystal parameters.

Isochronal and isothermal annealing of the u.v.-activated spectrum suggested that it represents a hole trap or recombination centre, with a thermal ionization temperature of $\geq$ 100K. The existence of several shallow electron traps was deduced by their interaction with the recombination centre during isochronal annealing.

8.4 SUGGESTED FUTURE WORK

Further single crystal studies include the doping of other impurity ions, e.g. Cobalt, Vanadium and Niobium into rutile, their characterisation by e.s.r. and deduction of the trapping behaviour by annealing techniques.

The addition of an infra-red monochromator to the present optical system would allow the study of optical ionization energies of u.v. generated centres.

Potentially useful work with powders includes the measurement of absolute concentrations of u.v. generated defect centres and their variation between different pigment samples with known physical properties. Isochronal annealing and infra-red bleaching could be used to estimate relative distributions of other shallow trapping centres and their activation energies.

REFERENCES

Abragam A, and Bleaney B; 'Electron Paramagnetic Resonance of Transition Ions', Clarendon Press, (1970).

Addiss, R.R. et al; App.Phys. Lett. 12 397 (1968).

Anderson, P.O, et al ; Phys. Rev. B 8 4956 (1973).

Andresen, H.G ; Phys. Rev. 120 1606 (1960).

Assenheim, H.M ; 'Introduction to Electron Spin Resonance' Hilger (1966).

Ayscough, P.B ; 'Electron Spin Resonance in Chemistry', Methuen (1967).

Barbanel, V.I, et al ; Sov.Phys. Solid State 11 431 (1969).

Baur,W.H ; Acta Cryst. 9 515 (1956).

Berks,J.S, et al ; J.Appl.Phys. 36 3276 (1965).

Bogomolov V.N. et al ; Sov.Phys. Solid State 9 2647 (1968).

Breckenridge, R.J. et al ; Phys. Rev. 91 793 (1953).

Bube, R.H ; 'Photoconductivity of Solids', Wiley (1960).

Carnahan, R.D. et al ; J.App.Phys. 34 3095 (1963).

Carrington A. et al ; Quart. Rev.14 427 (1960).

Carter, D.L. et al ; Phys. Rev. 118 1485 (1960).

Chandrashekhar G.V, et al ; J. Electrochem. Soc. 123 392 (1976).

Chang T ; Phys.Rev. 136A 1413 (1964).

Chase J.D. et al ; J. Cryst. Growth 5 294 (1969).

Chen R ; J. App.Phys. 40 570 (1969).

Chester P.F ; Js App.Phys. 32 866 (1961) (a).

Chester P.F ; Ji App.Phys. 32 2233 (1961) (b).

Chester P.F ; C.E.R.L. Report RD/L/R 1267 (1964).

Clark W. et al ; JiPhys. C 3 1047 (1970).

Cronenger D.C ; Phys. Rev. 87 876 (1952).

De Vare J.R ; J. Opt. Soc. Am. 41 416 (1951).

Dominik L.A.K. et al ; Phys. Rev. 156 910 (1967).

Dominik L.A.K. et al ; Phys. Rev. 163 756 (1967).

Ensign T.C. et al ; Phys. Rev. 188 703 (1969).

Farrell E.F. et al ; Am.Ceram.Soc.Bull. 54 1017 (1975).

Faughnan B.W. et al ; Phys. Rev. Lett. 21 1331 (1968).

Frederikse H.P.R: J.App.Phys. 32 2211 (1961).

Gerritsen H.J. et al ; Phys. Rev. Lett. 2 153 (1959).

Gerritsen H.J. et al ; Phys. Rev. 119 1010 (1960).

Gerritsen H.J. et al ; Phys. Rev. 125 1853 (1962).

Gerritsen H.J. et al ; Phys. Rev. 132 1507 (1963) (a).

Gerritsen H.J ; Paramagnetic Resonance 1, Academic Press, (1963) (b).

Ghosh A.K. et al ; Phys. Rev. 184 979 (1969).

Grabner L. et al ; Phys. Rev. B2 590 (1970).

Grant F.A ; Rev. Mod. Phys. 31 646 (1959).

Hillhouse R.W.A. et al ; Phys. Stat. Sol (a) 46 163 (1978).

Holt J ; Brit.J.App.Phys. 16 639 (1965).

Huntington H.B. et al ; Phys. Rev. Lett. 14 177 (1965).

Iguchi E. et al ; J.Phys. Soc.Jap. 32 1415 (1970).

Ikebe M. et al ; J.Phys. Soc. Jap. 26 43 (1969).

Iyengar R.D. et al ; J.Amer.Chem. Soc. 88 5055 (1965).

Iyengar R.D. et al ; J. Colloid Interface Sci. 35 424 (1971).

Johnson O.W ; App.Phys. Lett. 13 338 (1968) (a).

Johnson O.W., et al ; Phys. Rev. 175 1102 (1968), (b).

Kerssen J. et al ; Physica 69 535 (1973).

Kingsbury P.I. et al ; Phys. Rev. 175 1091 (1968).

Kofstad P ; Less Common Metals 13 635 (1967).

Kubec F. et al ; J. Chem.Phys. 57 1660 (1972).

Low W. et al ; Solid State Physics 17 135 (1965).

Mirlin D.N. et al ; Sov.Phys. Sol. State. 11 1995 (1970).

Miyoko Y ; Phys.Lett. 24A 635 (1967).

Mizushima K. et al ; J.Phys. Soc. Jap. 32 1519 (1972).

Moore C.H ; Trans.A.I.M.M.E. 184 194 (1949).

Nassau K. et al ; J.Amer.Ceram.Soc. 45 474 (1962).

Ohlsen W.D ; Phys. Rev. B7 4058 (1973).

Primet M. et al ; J. Chim.Phys. 67 1627 (1970).

Purcell T. et al ; J. Chem.Phys. 54 2800 (1971).

van Raulte J.A ; J.App.Phys. 36 3365 (1965).

Reed T.R. et al ; J.App. Phys. 32 821 (1961).

Sandin T.R. et al ; Phys. Rev. 177 1370 (1969).

Schollmeier G. et al ; Z. Angew.Phys. 22 471 (1967).

Shannon R.D. et al ; J.Amer.Ceram.Soc. 48 391 (1965).

Shen L.N. et al ; Phys. Rev. B 10 1823 (1974).

Slepetys R.A. et al ; J.Phys. Chem. 73 2157 (1969).

Sochava L.S. et al ; Sov.Phys. Sol.State 12 946 (1970).

Sochava L.S. et al ; Sov.Phys. Sol.State 13 1802 (1972).

Verneuil ; Compt. Rend. 135 791 (1902).

Wachtman J.B. et al ; Phys. Rev. 148 811 (1966).

Weeks R.A ; Bull.Am.Phys. Soc. 6 178 (1961).

Wilmhurst T.H. Electron Spin Resonance Spectrometers, Hilger, (1967).

Wittke J.P ; JsElectrochem Soc. 113 193 (1966).

Yagi E. et al ; J.Phys. Soc.Jap. 42 939 (1977).

Yamaka E. et al ; Phys. Rev. 125 1568 (1962).

Yamaka E ; J.Phys. Soc. Jap. 18 1095 (1963).

Yamaka E. et al ; Phys. Rev. 135A 144 (1964).

Young C.G. et al ; Bull.Am.Phys.Soc. 6 248 (1961).

Zimmerman P.H; Phys.Rev. B8 3917 (1973).

Zwingel D ; Solid State Comm. 20 397 (1976).